

Copyright
by
Shang-Te Yang
2014

**The Dissertation Committee for Shang-Te Yang Certifies that this is the approved
version of the following dissertation:**

**Design and Application of Microstrip Leaky Wave Antennas for Radar
Sensing**

Committee:

Hao Ling, Supervisor

Andrea Alù

Dean Neikirk

Ching-Kuang Clive Tzuang

Ali Yilmaz

**Design and Application of Microstrip Leaky Wave Antennas for Radar
Sensing**

by

Shang-Te Yang, B.S.; M.S.E.

Dissertation

Presented to the Faculty of the Graduate School of

The University of Texas at Austin

in Partial Fulfillment

of the Requirements

for the Degree of

Doctor of Philosophy

The University of Texas at Austin

August 2014

Dedicated to my wife and family.

Acknowledgements

I would like to thank everyone who helped me in the journey of my graduate study. First of all, I would like to express my deepest gratitude to my supervisor, Dr. Hao Ling. He is an open-minded scholar who is always enthusiastic about research. His insightful guidance helped me develop my primitive ideas into executable research. Next, I would like to thank Dr. Ching-Kuang Clive Tzuang. He introduced me into the wonderful world of electromagnetics when I was an undergraduate student. He also kindly served as my committee member across the Pacific Ocean. I am also grateful for Dr. Andrea Alù, Dr. Dean Neikirk, and Dr. Ali Yilmaz for serving on my dissertation committee. They provided invaluable comments.

My appreciation also goes to my fellow lab members: Dr. Yang Li, Dr. Nicholas J. Whiteloni, Dr. Ickjae Yoon, Dr. Aale Naqvi, and Mr. Chenchen Jimmy Li. Their research topics led me to have a better picture of the field. We also had numerous inspiring discussions. Especially, I would like to thank Dr. Shobha S. Ram for offering discussions over phone.

Finally, I would like to thank my family and friends. I owe them so much for their unconditional support and love. Thanks to my wife, Yen-Pi Cheng. I am fortunate to meet her in Austin, Texas.

SHANG-TE YANG

The University of Texas at Austin

August 2014

Designs and Applications of Microstrip Leaky Wave Antenna for Radar Sensing

Shang-Te Yang, Ph.D.

The University of Texas at Austin, 2014

Supervisor: Hao Ling

This dissertation investigates the application of the frequency-scanned beam of a microstrip leaky wave antenna (LWA) to track humans in the two-dimensional (2-D) range-azimuth plane. The history, operating principles and frequency-scanned properties of a microstrip LWA are first reviewed. The basic concept of using a microstrip LWA to track humans is verified by designing, building and testing a broadband microstrip LWA, developing the necessary processing algorithm, and collecting data using a vector network analyzer. A number of topics are then investigated to further advance the concept. First, the idea of combining the frequency-scanned antenna with a short-pulse ultra-wideband (UWB) radar is developed to realize a portable, real-time system for human tracking. The radar concept and the components of the system are discussed in detail. Line-of-sight and through-wall measurements of a human subject are carried out to demonstrate the performance. Second, a new LWA structure is proposed to achieve a narrower azimuth beam, which requires both a small leaky-wave attenuation constant and a long aperture. The transverse resonance method (TRM) is applied to analyze the proposed structure and the results are verified with measurements of a built prototype. Third, a new signal processing technique, compressive sensing, is applied to further improve the resolution in both the azimuth and down range dimensions. The technique is

tested with simulation and measurement data and is shown to produce sharper target responses in both the down range and azimuth dimensions. Lastly, the radar cross-section (RCS) of a microstrip LWA is studied. The antenna mode scattering and structural mode scattering are modeled separately. A ray picture is provided to explain the observed time-domain features using the group delay of the leaky wave.

Table of Contents

| | |
|---|----|
| List of Tables | x |
| List of Figures | xi |
| Chapter 1: Introduction | 1 |
| 1.1 Background | 1 |
| 1.2 Motivation..... | 3 |
| 1.3 Scientific Objective and Approach | 5 |
| 1.4 Organization..... | 6 |
| Chapter 2: Microstrip Leaky Wave Antenna | 8 |
| 2.1 Previous Works on Microstrip LWA..... | 8 |
| 2.2 TRM Analysis of A Half-width Microstrip LWA | 11 |
| 2.2 Radiation patterns of a Half-width Microstrip LWA..... | 17 |
| 2.3 Conclusion | 24 |
| Chapter 3: Tracking Multiple Humans Using Microstrip Leaky Wave Antennas | 26 |
| 3.1 Broadband Microstrip Leaky Wave Antenna | 26 |
| 3.2 Radar Concept and Processing Algorithm..... | 32 |
| 3.3 Radar Measurements..... | 37 |
| 3.4 Conclusion | 42 |
| Chapter 4: Combining a Frequency-scanned Antenna with a Short-Pulse Radar for 2-D Imaging..... | 44 |
| 4.1 Introduction..... | 44 |
| 4.2 The P410 Short-Pulse UWB Radar..... | 45 |
| 4.3 A Long Microstrip leaky Wave Antenna for the P410 | 50 |
| 4.4 System Integration and Characterizing the P410..... | 54 |
| 4.5 Line-of-Sight and Through-Wall Tracking of Human..... | 62 |
| 4.6 Conclusion | 66 |
| Chapter 5: Two-section Microstrip Leaky Wave Antenna | 67 |
| 5.1 Introduction..... | 67 |

| | |
|---|------------|
| 5.2 Antenna Geometry and TRM Analysis..... | 68 |
| 5.3 Prototype and Measurement | 75 |
| 5.4 Narrow Beam Antenna Design | 80 |
| 5.5 Discussion | 84 |
| 5.6 Conclusion | 87 |
| Chapter 6: 2-D Imaging Using a Microstrip LWA with Compressive Sensing | 88 |
| 6.1 Compressive Sensing..... | 88 |
| 6.2 Problem Formulation and Validation..... | 90 |
| 6.3 Snapshots of 2-D Tracking using Compressive Sensing | 94 |
| 6.4 Resolving Capability of Compressive Sensing..... | 96 |
| 6.5 Compressive Sensing and a Long Microstrip LWA | 99 |
| 6.6 Conclusion | 104 |
| Chapter 7: Radar Cross-Section of a Microstrip LWA..... | 106 |
| 7.1 Introduction..... | 106 |
| 7.2 Radiation Properties of a Microstrip LWA..... | 107 |
| 7.3 Modeling of Individual Scattering Mechanisms..... | 111 |
| 7.4 Time Domain Interpretation of Antenna Mode Scattering | 114 |
| 7.5 Conclusion | 116 |
| Chapter 8: Conclusions and Future Work..... | 118 |
| 8.1 Conclusions..... | 118 |
| 8.2 Future Work..... | 121 |
| REFERENCES | 125 |

List of Tables

| | | |
|----------|--|----|
| Table 1: | Simulated Performances of Conventional Half-width microstrip LWAs..... | 83 |
| Table 2 | Simulated Performances of Two-section microstrip LWAs..... | 84 |

List of Figures

| | | |
|-----------|--|----|
| Fig. 2.1 | Structure of the half-width microstrip..... | 12 |
| Fig. 2.2 | The illustration of the relationship between the wave numbers. | 14 |
| Fig. 2.3 | Normalized propagating and attenuation constants of a half-width microstrip LWA structure versus frequency computed using TRM. | 16 |
| Fig. 2.4 | Normalized propagating and attenuation constants of an air-filled half-width microstrip LWA structure versus frequency computed using TRM. | 18 |
| Fig. 2.5 | The built prototype..... | 19 |
| Fig. 2.6 | FEKO simulation setup..... | 20 |
| Fig. 2.7 | The far field patterns using difference mesh sizes. | 20 |
| Fig. 2.8 | The relative errors between the far field patterns at different directions using difference mesh sizes. $\lambda_0/25$ is used as the reference for each of the curve shown. | 21 |
| Fig. 2.9 | The steps to derive the equivalent magnetic current model..... | 22 |
| Fig. 2.10 | Comparison of radiation patterns between TRM theory, simulation and measurement at three different frequencies. The patterns are plotted versus θ , which was defined with respect to the z-axis in Fig. 2.1..... | 23 |
| Fig. 3.1 | The propagation and attenuation constants of the higher order leaky modes on a half-width microstrip LWA with $\epsilon_r = 4.4$. The propagation constants are the solid curves and the attenuation constants are the dashed curves..... | 28 |

| | | |
|----------|---|----|
| Fig. 3.2 | The propagation and attenuation constants of the higher order leaky modes on a half-width microstrip LWA with $\epsilon_r = 1$. The propagation constants are the solid curves and the attenuation constants are the dashed curves. | 28 |
| Fig. 3.3 | The built half-width microstrip LWA prototype. The far end is an SMA connector with the center tip directly soldered to the top microstrip. | 30 |
| Fig. 3.4 | Propagation and attenuation constants of the built prototype calculated using TRM. The structure parameters are $W/2 = 15\text{mm}$, $h = 2\text{mm}$, and $\epsilon_r = 1$ | 30 |
| Fig. 3.5 | Measured antenna gain pattern plotted as a function of frequency and azimuth angle. The gain value is color coded from 0 to 15dBi. | 31 |
| Fig. 3.6 | Illustration of the radar concept. The frequency-scanned pattern of the microstrip LWA is used to track humans. | 32 |
| Fig. 3.7 | Simulation results based on the point scatterer model. (a) Frequency response of two targets located at different azimuth angles and distances to the antenna. (b) Range profile obtained after the inverse Fourier transform. (c) Range-gated frequency responses for windows (A) and (B) in (b). The individual frequency responses can be used to estimate target bearings. (d) Final range-azimuth image of the simulated scene. | 35 |
| Fig. 3.8 | The antenna and measurement setup. | 38 |
| Fig. 3.9 | The trihedral target, which is 16cm per side. | 39 |

| | | |
|-----------|--|----|
| Fig. 3.10 | Range-azimuth image generated from measured data of two stationary trihedrals. The two trihedrals are placed at positions similar to the simulated scene in Fig. 3.7..... | 39 |
| Fig. 3.11 | Snapshot of the two-human tracking measurement. | 40 |
| Fig. 3.12 | Range-azimuth snapshots from a continuous human tracking measurement. Subject (A) walks in the clockwise direction while subject (B) walks in the counterclockwise direction. | 41 |
| Fig. 3.12 | Range-azimuth snapshots from a continuous human tracking measurement. Subject (A) walks in the clockwise direction while subject (B) walks in the counterclockwise direction. | 42 |
| Fig. 4.1 | The rake-receiver architecture | 47 |
| Fig. 4.2 | The raw range scan of a trihedral in the scene..... | 48 |
| Fig. 4.3 | The mechanisms of the early-time jamming..... | 49 |
| Fig. 4.4 | The built antenna prototype. The pen is the dimension reference and a close-up view of the excitation is shown in the inset..... | 51 |
| Fig. 4.5 | Simulated gain pattern of the MLWA vs. frequency and angle. | 51 |
| Fig. 4.6 | (a) S11 of the built prototype with the far end left open. (b) The time response of the antenna with the far end left open. (c) S11 of the built antenna with a matched far end. (d) The time response of the antenna with a matched far end. | 53 |
| Fig. 4.7 | Illustration of the system concept. | 55 |
| Fig. 4.8 | The measured S-parameters of the CS-16-50 circulator..... | 56 |

| | | |
|-----------|--|----|
| Fig. 4.9 | The pulse shapes of the Fourier transformed insertion loss and isolation. They are labelled as through and rejection, respectively. | 56 |
| Fig. 4.10 | The scattering calibration. (a) VNA measured equivalent time response. (b) VNA measured, time-gated equivalent frequency response. (c) P410 measured target response. (d) P410 measured, time-gated equivalent frequency response. | 58 |
| Fig. 4.11 | The complex equivalent frequency response of the P410 transceiver. | 59 |
| Fig. 4.12 | (a) - (c) Measured frequency response of targets at about 80°, 60°, and 40°. (d) - (f) Combined response of full-wave simulations and the equivalent frequency response of the P410. | 61 |
| Fig. 4.13 | Snapshots of the line-of-sight measurement of a walking human subject. | 63 |
| Fig. 4.14 | The setup of the through-wall measurement. The antenna is put right against the wall. | 64 |
| Fig. 4.15 | Snapshots of the through-wall measurement of a walking human subject. | 65 |
| Fig. 5.1 | (a) The geometry of a conventional half-width microstrip LWA. It consists of a top microstrip, a ground plane, and a side shorting plane. (b) The proposed two-section microstrip LWA. It consists of two microstrip LWA sections with different thicknesses of dielectric material. The top microstrip is kept at the same height. | 70 |

| | | |
|----------|--|----|
| Fig. 5.2 | The transverse equivalent circuit model of the proposed two-section microstrip LWA. The left most edge represents the shorting plane and the right most impedance represents the radiation impedance from a parallel plate waveguide connecting to an extended dielectric slab. The capacitor in the middle models the step discontinuity..... | 70 |
| Fig. 5.3 | Complex normalized propagation constants for different heights in the second section. Solid lines are propagation constants and dashed lines are attenuation constants..... | 73 |
| Fig. 5.4 | Complex normalized propagation constants for different widths in the second section. Solid lines are the propagation constants and dashed lines are attenuation constants..... | 73 |
| Fig. 5.5 | (a) Attenuation constants at different beam directions of the geometries discussed in Fig. 5.3. (b) Attenuation constants at different beam directions of the geometries discussed in Fig. 5.4..... | 74 |
| Fig. 5.6 | The prototype of the proposed two-section microstrip LWA consists of two aluminum blocks. The air-filled region is removed from the bottom ground plane using a milling machine and the top aluminum block works as the top microstrip..... | 76 |
| Fig. 5.7 | Measured radiation pattern of the proposed two-section microstrip LWA prototype..... | 77 |
| Fig. 5.8 | Measured radiation pattern of the conventional half-width microstrip LWA prototype..... | 77 |

| | | |
|-----------|---|----|
| Fig. 5.9 | Retrieved propagation and attenuation constants from the radiation pattern of the proposed two-section microstrip LWA. Dashed curves are the attenuation and propagation constants computed using TRM. | 79 |
| Fig. 5.10 | Retrieved propagation and attenuation constants from the radiation pattern of the conventional half-width microstrip LWA. Dashed curves are the attenuation and propagation constants computed using TRM..... | 80 |
| Fig. 5.11 | The radiation patterns of the proposed two-section microstrip LWA at 2.9GHz, 3.4GHz and 3.9GHz. FEKO simulation results are shown as blue curves and the TRM predicted results are shown as black curves..... | 82 |
| Fig. 5.12 | The radiation patterns of the conventional half-width microstrip LWA at 5.1GHz, 6GHz and 7GHz. FEKO simulation results are shown as blue curves and the TRM predicted results are shown as black curves. | 83 |
| Fig. 5.13 | Simulated efficiencies of the 200cm long conventional half-width microstrip LWA and the 200cm long two-section microstrip LWA. Both structures are simulated with copper and steel. | 86 |
| Fig. 5.14 | Simulated S11 of the proposed 200cm two-section microstrip LWA using the MoM solver in FEKO. | 87 |
| Fig. 6.1 | Range-azimuth images generated using the L1-norm minimization with point scatterer simulation. | 93 |

| | | |
|----------|--|-----|
| Fig. 6.2 | Range-azimuth images generated using the L1-norm minimization of the two-trihedral measurement..... | 93 |
| Fig. 6.3 | Range-azimuth images of the human tracking measurement generated using L1-norm minimization. (a) - (h) are the same snapshot as Fig. 3.12(a) – (h)..... | 95 |
| Fig. 6.3 | Range-azimuth images of the human tracking measurement generated using L1-norm minimization. (a) - (h) are the same snapshot as Fig. 3.12(a) – (h)..... | 96 |
| Fig. 6.4 | The two-way 3dB beamwidth and bandwidth of the 28.5cm long half-width microstrip LWA. | 98 |
| Fig. 6.5 | (a) The ground truth of three sets of targets placed 3dB in azimuth and down range locations. The color code is reversed compared to the others to better show the targets. (b) The 2-D image generated by compressive sensing. | 99 |
| Fig. 6.6 | The 2-D image generated using the STFT. (a) 113cm Hamming window. (b) 30cm Hamming window. | 99 |
| Fig. 6.7 | Testing of the near field effect at 90m, 30m, 10m, and 3m. The ground truths are on the left and the images obtained using compressive sensing are shown on the right..... | 101 |
| Fig. 6.7 | Testing of the near field effect at 90m, 30m, 10m, and 3m. The ground truths are on the left and the images obtained using compressive sensing are shown on the right..... | 102 |
| Fig. 6.8 | The reconstructed near-field image using a matching near-field A matrix. | 102 |

| | | |
|-----------|---|-----|
| Fig. 6.9 | The compressive sensing image of Fig. 6.5(a) using the 90cm-long microstrip LWA. The targets are clearly resolved in both the azimuth and down range dimensions. | 103 |
| Fig. 6.10 | The 3dB beamwidth and bandwidth of the 90cm-long microstrip LWA. | 104 |
| Fig. 7.1 | The propagation and attenuation constants of a half-width microstrip LWA shown in the inset. These quantities are computed using TRM and normalized with respect to the free space wave number. The blue curves are for the lowest order leaky mode and the black curves are for the next higher order leaky mode. | 108 |
| Fig. 7.2 | Simulated RCS of a 29cm-long half-width microstrip LWA as a function of frequency and aspect angle. | 110 |
| Fig. 7.3 | Simulated RCS of a 29cm-long half-width microstrip LWA as a function of range and aspect angle. | 110 |
| Fig. 7.4 | Measured RCS of a 29cm-long half-width microstrip LWA as a function of range and aspect angle. | 111 |
| Fig. 7.5 | Three scattering features modeled individually and displayed in the range-aspect plane. (a) Primary antenna mode scattering. (b) First higher-order bounce antenna mode scattering. (c) Structural mode scattering. | 113 |

Fig. 7.6 (a) The coupling ray (in red) and the re-radiation ray (in black) along the sideview of the antenna. (b) The earliest and the latest ray pairs are labeled as (i) and (ii). Their corresponding time delays are plotted as the dashed and solid lines in Fig. 7.7.....117

Fig. 7.7 Total RCS in the range-aspect plane by adding the three individually modeled scattering mechanisms. The dashed and dotted lines correspond respectively to the lower and upper bound in the range delay of the the primary antenna mode scattering.....117

Chapter 1: Introduction

1.1 BACKGROUND

Monitoring human activities using radar is a topic of current research interest, with applications ranging from urban military operations and law enforcement to disaster search-and-rescue and border security. Radio waves in the low GHz range can penetrate through walls and provide a non-intrusive means to monitor suspicious personnel or to search for vital signs of survivors buried under debris after disasters. Moreover, radar can operate at night as well as in all weather conditions. Thus, it is very useful for surveillance applications. Over the years, different radars have been developed to address different aspects of human monitoring.

Doppler radar has been exploited for human monitoring due to its capability to capture a unique feature of a moving human called the microDoppler, which was first reported by Geisheimer et al. in 2002 [1]. This feature corresponds to the non-rigid nature of a human body. As a human subject moves, the different body parts move in different directions with different speeds. Consequently, the movements of body parts can be identified by observing the various Doppler frequency components over time. Different human models were proposed to simulate the movements of a human subject and the results led to a better understanding of microDoppler features [1, 2, 3, 4, 5]. MicroDoppler features were also used to differentiate a human subject from other moving targets, such as a fan [6] or other animals [7, 8]. Other works further exploited human microDoppler features to achieve automatic target and activity identification [9, 10, 11, 12, 13, 14].

Doppler radar has also been combined with interferometry to achieve a low-complexity system to track direction-of-arrivals (DOAs) or two-dimensional (2-D) range-

azimuth positions of humans [15, 16]. The basic assumption used in these systems was that each target bears a distinct Doppler frequency and the targets can be separated in the Doppler domain. As a result, these systems are not very robust since different moving humans may move at a similar speed. Another approach was proposed to improve the performance by replacing interferometry with a four-element antenna array [17]. A joint Doppler-array processing was developed correspondingly.

Doppler radar has been further combined with a 2-D aperture to achieve a 2-D azimuth-elevation frontal view of a human. This is of interest because the frontal view corresponds more closely with our visual experience. Lin and Ling attempted this problem earlier using a Doppler radar and a three-element interferometry system [18]. However, only a blurry image of a human was formed under the most idealized condition. The joint Doppler-array processing in [17] was extended to simulate a radar frontal image of a human in [19]. However, a robust image was only achievable when a large antenna array with 20 x 20 elements was used. Hence, the array was never implemented.

Ultra-wide-band (UWB) radar is another class of radar that has also been utilized to monitor humans. Such type of radar can achieve a superior range resolution, which enables the radar to not only detect the range of targets but even sense the fine movements of human respiration [20, 21, 22, 23]. UWB radars have been combined with various 1-D arrays to achieve 2-D range-azimuth tracking of targets [24, 25, 26, 27, 28]. While UWB radar has a very fine range resolution, the azimuth resolution is still governed by the electrical size of the array employed. Some advanced signal processing techniques, such as MUSIC [29] and CLEAN [30], have been applied to improve the azimuth resolution of UWB radar systems without using large antenna arrays [31, 32].

UWB radar has also been combined with a 2-D aperture to achieve 3-D range-azimuth-elevation imaging of targets using different algorithms [33, 34, 35, 36, 37, 38]. Among these works, some were investigations using only simulation data, while others were tested with a synthetic aperture by moving a small set of antennas mechanically in a 2-D plane. Only one physical 2-D array with 12 elements was implemented in [36]. Note that a synthetic aperture is not a practical means for tracking moving humans due to the time-varying nature of human movements. Consequently, a large, complex, and costly antenna array system is required to form a 3-D image of a moving human. To date, no such large array has ever been built for human monitoring applications.

More recently, there is effort to combine Doppler radar and UWB radar to form a multi-functional system [39, 40, 41, 42, 43]. The pulse-to-pulse Doppler features measured with a UWB radar were exploited to achieve activity identification [39]. Moreover, a joint range-Doppler feature extraction was explored in [42] to achieve a better identification performance. The combination of a Doppler radar and a UWB radar leads to a higher-dimensional feature space, which is not only useful for target identification but may also help achieve a better performance in tracking and imaging of humans.

1.2 MOTIVATION

In both human tracking and imaging applications, the radar system must have a narrow beam and the beam must be able to scan rapidly to different directions. Moreover, a physical aperture instead of a synthetic one is required due to the time-varying nature of human movements. This necessitates the use of a large antenna array with many controllable elements, which leads to high complexity and high cost. Some physical apertures have been built and tested in earlier works. Interferometry systems were

combined with Doppler processing for the tracking and imaging problems [15, 16, 18]. However, such low-cost system usually leads to a large degradation in radar performance. Other larger antenna arrays have also been explored, such as the 2-D “flower” array in [36] and the eight-element Vivaldi antenna array in [44]. However, data were collected sequentially from the array elements via switches in both works before software beamforming was applied. This approach reduces the number of phase shifters and transceivers at the cost of acquisition time. Therefore, these systems are still limited when applied to monitor a fast moving human subject. A different approach than an antenna array is needed. It has to be a physical aperture that can rapidly scan to different directions without the complexity and cost of an antenna array.

A frequency-scanned antenna is a class of antennas whose beam can be steered by changing the carrier frequency. The frequency-scanned beam of slotted waveguides was used for air defense radar in the 1960s, but was subsequently replaced by phased arrays. This is because frequency is a precious resource for military radar to counteract against propagation effects and hostile jamming [45]. Very recently, there is a renewed interest in applying the frequency-scanned beam of a leaky wave antenna (LWA) to automotive collision avoidance applications [46, 47, 48, 49]. Wollitzer et al. applied a dielectric slab LWA as the front-end of a radar using two frequency tones [46]. Matsuzawa et al. proposed another LWA for automotive applications, in which a movable dielectric slab was employed to steer the beam instead of changing the carrier frequency [47]. Ettore et al. proposed a pillbox LWA integrated with a parabolic reflector system [48]. The frequency-scanned beam of the LWA steers the beam in the elevation plane while an offset feed position was used to steer the beam in the azimuth plane.

To date, frequency-scanned antennas have not been applied for human detection, tracking or monitoring. A microstrip LWA [50] is a particularly attractive candidate

among the many different LWA designs, since the structure is based on the standard microstrip transmission line. Such simple structure leads to easier manufacturing. Moreover, the cross-sectional dimensions of a microstrip LWA are much more compact than those of a rectangular waveguide, which is commonly used to realize a frequency-scanned slotted array. In this dissertation, a microstrip LWA will be explored for human tracking applications. Only a single broadband transceiver is required to steer the frequency-scanned beam and the beam direction can be changed rapidly. A simple and portable system can be implemented to monitor human activities in real-time.

1.3 SCIENTIFIC OBJECTIVE AND APPROACH

The objective of my dissertation is to apply the frequency-scanned beam of a microstrip LWA to tracking human subjects in the 2-D range-azimuth plane. To accomplish this objective, the following approaches are taken. First, the basic concept of using a microstrip LWA to track humans is demonstrated by designing, building and testing a broadband microstrip LWA, developing the necessary processing algorithm, and collecting data using a vector network analyzer (VNA) to achieve 2-D human tracking. To further advance the concept, three topics are researched. First, the idea of combining the frequency-scanned antenna with a short-pulse UWB radar is explored to achieve a portable, real-time system for human tracking. Second, a new LWA structure is investigated to achieve a narrower azimuth beam. Third, a new signal processing technique, compressive sensing, is applied to further improve the resolutions in both the azimuth and down range dimensions. Lastly, the radar cross-section (RCS) of a microstrip LWA is studied.

1.4 ORGANIZATION

The rest of this dissertation is organized as follows. A detailed literature review on microstrip LWA is presented in Chapter 2. The transverse resonance method (TRM) analysis of a half-width microstrip LWA is reviewed [51]. The relationship between the leaky mode and the radiation properties is discussed, and a single half-width microstrip LWA is simulated, built, and measured to show the frequency-scanned beam.

In Chapter 3, a broadband half-width microstrip LWA is designed for the human tracking application. The antenna is built and the broadband radiation pattern is measured. The concept of “target bandwidth,” which defines the antenna bandwidth from the perspective of a target instead of the input port of an antenna, is discussed. The tracking algorithm is developed correspondingly. Data of static and moving targets are measured with a VNA to show the 2-D range-azimuth tracking capability.

In Chapter 4, the idea of combining a microstrip LWA and a short-pulse radar is explored. First, the architecture of a short-pulse UWB radar is discussed. Afterward, the equivalent frequency response of the radar is characterized and measurements of static targets are presented to show the direction finding capability. Line-of-sight and through-wall measurements of a human subject are then carried out to demonstrate the tracking performance of this portable system.

In the next two chapters, two different approaches are studied to further improve the resolving capability of the system. A two-section microstrip LWA with a narrower beam is proposed and discussed in Chapter 5. The antenna is designed to reduce the attenuation constant of the leaky mode while retaining the original frequency-scanned property. The performance is compared to a half-width microstrip LWA and the impacts of a narrow-beam antenna on the whole radar system are discussed.

In Chapter 6, compressive sensing is applied to further improve the system resolution through signal processing. First, compressive sensing is reviewed from the mathematical perspective and previous applications to radar problems are discussed. The tracking problem using a frequency-scanned antenna is formulated into the framework of compressive sensing. The algorithm is first tested with a point scatterer simulation. Next, compressive sensing is applied to measurements of static target as well as moving humans to show the performance. Lastly, the resolving capability of compressive sensing is tested with closely spaced targets using point scatterer simulations.

In Chapter 7, the RCS of a microstrip LWA is discussed. The RCS is first simulated using a full-wave solver and presented in both the frequency and time domains. The simulated RCS is then compared to measured results. Next, different observed features are explained using analytical models of the antenna mode scattering and structural mode scattering. Lastly, a time-of-arrival ray picture is proposed to explain the observed features in the time domain and a connection to the dispersion of the leaky mode is made.

A detailed conclusion and some potential future research topics are presented in Chapter 8.

Chapter 2: Microstrip Leaky Wave Antenna

In this chapter, an introduction to the microstrip leaky wave antenna (LWA) is presented. We begin with a literature review of earlier works on microstrip LWAs. Next, the transverse resonance method analysis of a half-width microstrip LWA is reviewed. The relationship between the leaky mode and the radiation properties is discussed. We then design, simulate and measure an air-fill half-width microstrip LWA to show the discussed properties. This chapter provides the basic design and operating principles of a half-width microstrip LWA so that a broadband design can be implemented and applied to human tracking in the next chapter.

2.1 PREVIOUS WORKS ON MICROSTRIP LWA

A microstrip LWA is a simple and elegant structure for achieving a frequency-scanned beam. Microstrip line is a widely used guiding structure operating in the quasi-TEM mode. Studies of higher order modes on a microstrip line showed that these modes can radiate power. Thus, this type of mode is termed a leaky mode or a leaky wave, and its radiation properties are closely related to the mode characteristics. In the late 1970s, Ermert first reported on the propagation constants of higher order modes on a microstrip line [52]. For a higher order leaky mode on a microstrip, the propagation constant (β) is related to the beam direction:

$$\theta \approx \cos^{-1}\left(\frac{\beta}{k_0}\right) \quad (2.1)$$

where k_0 is the free space wave number and θ is the beam direction defined with respect to the longitudinal direction of the microstrip. Subsequently, Menzel measured the frequency-scanned beam of a microstrip line acting as a leaky wave antenna by

exciting it with an unbalanced feed [53]. The first accurate analysis of both the propagation and attenuation constants was done by Oliner and Lee [50]. Their analysis was based on the transverse resonance method (TRM). In the analysis, the cross-section of the microstrip structure is considered as a section of parallel plate transmission line with two complex impedances at the two ends. The impedance accounts for the discontinuity between a parallel plate waveguide and a grounded dielectric slab. This complex impedance was derived rigorously using the Wiener-Hopf technique by Chang and Kuester [54]. The result is in the form of a Sommerfeld integral, which needs to be evaluated numerically with contour deformation around the two poles. The Sommerfeld integral was later simplified using the thin-substrate approximation by Kuester et al. in [55]. The result is a simple algebraic equation related to the thickness of the substrate, material parameters, and wave numbers. After Oliner and Lee applied the simplified equation to their TRM analysis in [50], it became clear that the two poles in the Sommerfeld integral are actually related to different types of leakage. The first pole corresponds to a space-type leakage and it is related to the radiation properties of a microstrip LWA. The second pole corresponds to a surface-type leakage and it is related to the power lost from the microstrip into the TM_0 mode of the grounded dielectric substrate. Oliner and Lee also used the propagation and attenuation constants to explain Menzel's measurement results [56]. It was concluded that both the propagation and attenuation constants are important parameters to properly design a microstrip LWA. The former is related to the beam direction, and the latter is related to the gain and beamwidth. Lastly, a different design procedure for a microstrip LWA was proposed based on a cavity model by Luxey and Latheurte [57].

In order to design a feed structure to excite the leaky mode, the field distribution and mode impedance of the leaky mode are required. However, TRM analysis does not

answer these questions. Spectral domain analysis can be used to compute the complex propagation constant and the field distribution at the same time. It was first applied to study the higher order leaky modes on a microstrip by Grimm and Nyquist [58]. Afterward, Lin et al. studied several feeding structures using a spectral domain integral equation approach to simultaneously excite the leaky mode and suppress the fundamental mode [59]. Chen and Tzuang measured the mode impedance and the complex propagation constant using a time-gated measurement [60]. The results were compared to those computed using the spectral domain approach with a good agreement. The mode impedance of the lowest order leaky mode on a microstrip was also studied using other methods. In [61], Hong et al. derived the mode impedance using a lossy waveguide model. In [62], Jiang et al. studied a simplified structure to approximate the mode impedance. A microstrip is simplified by placing perfect magnetic conductors (PMCs) at the two sides. The field equations were formulated and related to the mode impedance. It is noted that the corresponding transcendental equation of the simplified structure is not correct since radiation is not considered. However, an approximate mode impedance can be obtained by using the proper complex propagation constant in the mode impedance expression for the simplified structure. The proper complex propagation constant can be computed using TRM or the finite-element method (FEM). Lastly, Zelinski et al. modified the conventional microstrip structure into a half-width design by inserting a vertical perfect electric conductor (PEC) symmetry plane at the center of the structure [51]. This design suppresses the fundamental mode and simplifies the feed.

Other variations of the basic microstrip LWA structure have also been proposed and studied. Mode properties of microstrip LWAs in an array environment were studied using the couple mode theory and spectral domain method [63, 64]. This is of interest since the mode of a microstrip LWA in an array environment may be different from that

of a stand-alone one due to the presence of neighboring elements. A laterally-shielded microstrip LWA based on the second higher-order mode was proposed by Gomez-Tornero et al. to control the propagation and attenuation constants separately [65]. This approach could lead to independent optimization of the beam direction and aperture distribution, which are closely related to each other for most microstrip LWAs and are usually difficult to engineer separately. In [66], Archbold et al. explored loading the radiating edge of a half-width microstrip LWA with capacitors to change the beam direction at a fixed frequency. TRM analysis was derived by including a distributed capacitance. A prototype with periodically loaded capacitors on the radiating edge was built and measured. Li et al. switched the shorted edge of a half-width microstrip LWA in a periodic pattern to achieve a wider scanning range. The concept is similar to the composite left-/right-handed microstrip LWA reported in [67]. Ouedraogo et al. further explored the idea of electronically scanning the beam direction using switches and discrete capacitors instead of varactors [68]. Different switch configurations for achieving a beam at different directions were found using a genetic algorithm. A tunable negative capacitive loading was also simulated by Long et al. to control the beam direction [69]. Recently, the complex propagation constants of a conventional microstrip LWA were revisited by Liu et al. to include the mutual coupling between the two edges [70]. Tomofuji et al. proposed a circular half-width microstrip LWA to achieve a broader frequency bandwidth. The structure was analyzed using an extended spectral domain method [71].

2.2 TRM ANALYSIS OF A HALF-WIDTH MICROSTRIP LWA

The detailed TRM analysis of a half-width microstrip [51] will now be presented, as this structure will be utilized throughout the remainder of this dissertation. The

structure can be considered by carrying out an odd-mode analysis of a conventional microstrip structure by inserting a vertical PEC symmetry plane at the center of the structure. This suppresses the fundamental guiding mode, which possesses even symmetry, and eases the design of the excitation structure. Zelingski further simplified the structure by removing the PEC symmetry plane outside the microstrip, since it does not change the field inside the microstrip structure. The resulting structure is shown in Fig. 2.1. It consists of a top microstrip, a side shorting plane, a ground plane, and a dielectric substrate with a dielectric constant ϵ_r . The width of the microstrip is $\frac{W}{2}$ and the thickness of the dielectric substrate is h .

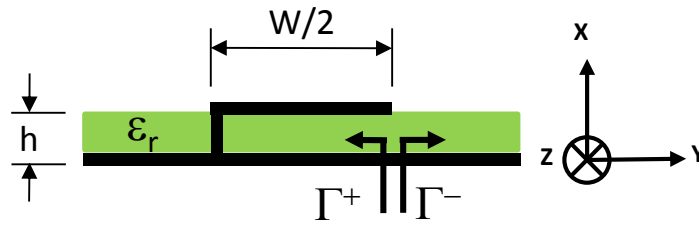


Fig. 2.1 Structure of the half-width microstrip.

To perform a TRM analysis, the transverse structure is modeled as a transmission line. One end is shorted and the other end is connected to a radiation impedance, which is at the interface between a parallel plate waveguide and a grounded dielectric slab [54]. The longitudinal direction of the antenna is chosen to be the z -axis. The reflection coefficient looking into the microstrip structure (Γ^+ in Fig. 2.1) is a shorted parallel plate waveguide and can be expressed as:

$$\Gamma^+ = -e^{-jk_t W/2} \quad (2.2)$$

where k_t is the transverse wave number. The reflection coefficient looking into the substrate is $\Gamma^- = e^{j\chi}$, and the simplified expression for χ assuming a thin substrate was derived in [55]. The result is repeated here:

$$\chi = 2 \tan^{-1} u - f_e \quad (2.3)$$

and

$$u = \frac{k_z}{k_t} \tanh\left(\frac{k_z h}{\pi} \left[\frac{1 - \epsilon_r}{\epsilon_r} g + 2Q \right]\right) \quad (2.4)$$

$$f_e = -\frac{2k_t h}{\pi} \left[\frac{g}{\epsilon_r} + 2Q - \ln(2\pi) \right] \quad (2.5)$$

where

$$Q = \sum_{m=1}^{\infty} \left(\frac{\epsilon_r - 1}{\epsilon_r + 1} \right)^m \ln(m) \quad (2.6)$$

$$g = \ln\left(jh \sqrt{k_0^2 - k_z^2}\right) + \gamma - 1 \quad (2.7)$$

γ is the Euler constant. By substituting the expressions into the transverse resonance condition $\Gamma^+ \Gamma^- = 1$, a transcendental equation can be derived as shown below:

$$\chi - k_t W + n\pi = 0 \quad (2.8)$$

where n is an integer dictating the order of the mode. The associated longitudinal propagation constant can be found by:

$$k_z = \sqrt{\epsilon_r k_0^2 - k_t^2} \quad (2.9)$$

It is noted that the physical solution for a radiating leaky mode requires the imaginary part of k_z to be negative and the imaginary part of k_t to be positive. The reasoning behind these choices is illustrated in Fig. 2.2. The structure is assumed to be excited from the left and the amplitude of the excited leaky wave is assumed to be A . The wave propagates toward the right in the $+z$ direction. The field strength at a position z on the microstrip can be expressed as $Ae^{-\alpha z}$, with a positive α to ensure that energy conservation is satisfied. Thus, the imaginary part of k_z must be a negative number. Moreover, the cosine relationship in (2.1) can be interpreted as the fact that the radiating beam in free space must elevate to match the phase on the microstrip, when the propagation constant (β) is smaller than k_0 . As for the real part of k_t , we can consider a 2-D transverse cut as the dash line in Fig. 2.2. Consider a microstrip with a finite length L , fields along the dash line can be traced back to different parts of the microstrip, through rays parallel to the elevated beam direction. Since the field on the microstrip is

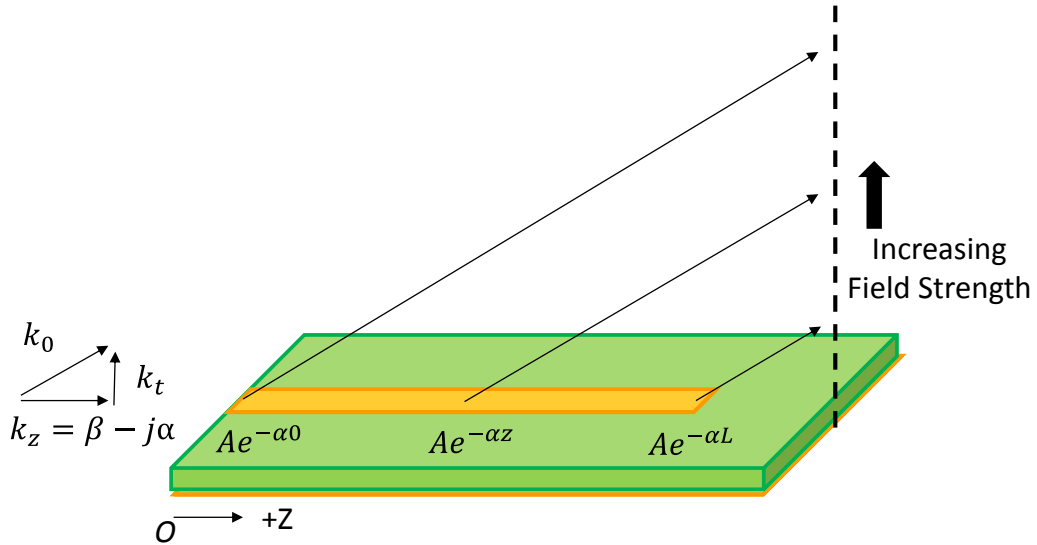


Fig. 2.2 The illustration of the relationship between the wave numbers.

stronger when it is located closer to the excitation, the corresponding field on the transverse cut is also stronger. As a result, the transverse field grows from the bottom to the top, until the height corresponds to the excitation end. The field strength decreases as the height is further increased beyond this position. However, TRM is a 2-D analysis and the source position is equivalently located at negative infinity along the z -direction. Hence, the transverse field in the 2-D cut grows as the height is increased. The imaginary part of k_t must be a positive number to ensure this condition.

The propagation and attenuation constants of a half-width microstrip LWA are computed using the above equations and shown in Fig. 2.3 as the solid and dash curves, respectively. They are normalized with respect to the free space wavenumber. The parameters of the structure are $W/2 = 15mm, h = 0.5mm, \epsilon_r = 4.4$. It can be observed in Fig. 2.3 that the normalized propagation constant starts from nearly zero and grows toward the square root of the dielectric constant as frequency is increased. Since the beam direction is related to the propagation constant through the cosine formula in (2.1), the beam steers from the broadside toward the endfire direction as the carrier frequency is increased. It is further noted that once the normalized propagation constant is greater than one (the black horizontal dash curve in Fig. 2.4), the corresponding beam direction becomes a complex number. This is similar to a plane wave problem when the incident angle is greater than the critical angle. The angle of refraction becomes a complex number without any physical meaning, and the field on the air side of the interface becomes evanescent. Similarly, the proper choice of k_t is with a negative imaginary part when the propagation constant is greater than the free space wave number. This choice ensures the field outside the microstrip is evanescent in the 2-D transverse cut. Physically, the mode transits from a leaky mode into a guided mode. It no longer radiates power as an antenna but only guides power in the $+z$ direction.

For the attenuation constant, it is a very large number when the frequency is low. This indicates that the leaky mode cannot propagate far in the z-direction at lower frequencies. It is noted that the structure is assumed to be PEC in the analysis. Thus, the attenuation constant does not originate from metal loss but is related to the radiation loss. For comparison, the propagation constant of a mode on a PEC rectangular waveguide is either purely propagating or purely evanescent. The mode becomes evanescent once the operating frequency is below the corresponding cutoff frequency. There is no complex wave number unless metal loss or dielectric loss is included. However, there is no such distinct cutoff phenomenon for the leaky modes on a microstrip. The onset frequency of a leaky mode is usually defined as the frequency where the propagation constant and the attenuation constant are equal. Starting from the onset frequency, the attenuation constant continues to decrease as the frequency is increased toward the critical frequency, where

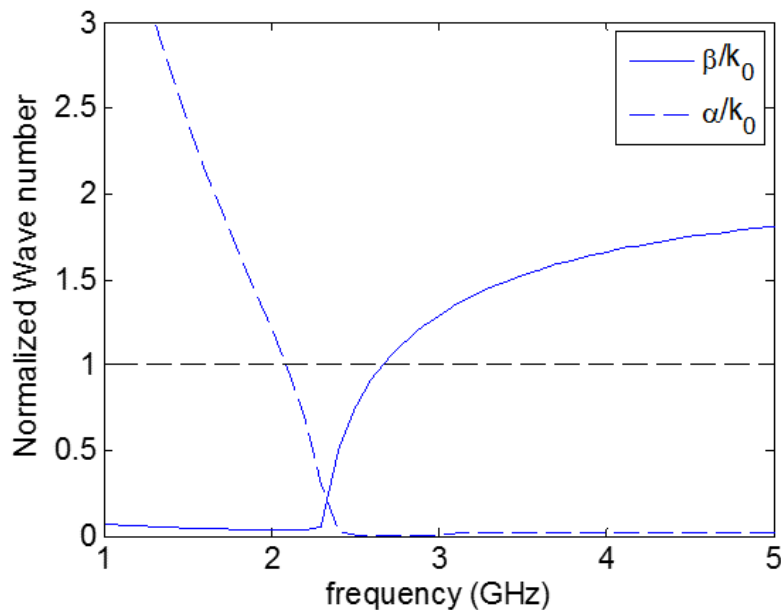


Fig. 2.3 Normalized propagating and attenuation constants of a half-width microstrip LWA structure versus frequency computed using TRM.

the propagation constant equals the free space wave number. The decreasing attenuation constant leads to a more uniformly illuminated aperture, which leads to a narrower beamwidth and a higher gain at higher frequencies. As frequency is further increased beyond the critical frequency, the dominant pole in the Sommerfeld integral changes from the space-type pole to the surface-type pole. Thus, the attenuation constant becomes corresponding to the power lost through the TM_0 mode of the grounded dielectric substrate. It is noted that such surface leakage is different from metal loss or dielectric loss.

2.2 RADIATION PATTERNS OF A HALF-WIDTH MICROSTRIP LWA

In this section, a half-width microstrip LWA is designed, built, and measured to verify the theoretical behaviors described in the previous section. Full-wave simulations are also carried out to simulate the radiation pattern and study the numerical convergence with different discretizations. An equivalent magnetic current model is discussed to compute the theoretical radiation pattern. Lastly, the radiation patterns computed using these methods are compared and discussed.

A half-width microstrip LWA with an air substrate is designed and the structure is shown as the inset in Fig. 2.4. The antenna consists of a 12.5mm wide top microstrip elevated 2mm from the ground plane. An air substrate instead of a dielectric substrate is chosen due to the simpler construction. Fig. 2.4 shows the propagation constant (β) and attenuation constant (α) of the lowest order leaky mode versus frequency computed using TRM. They are normalized with respect to the free space wave number, k_0 , at different frequencies. From 5GHz to 10GHz, the normalized propagation constant changes from 0.259 to 0.867. The corresponding beam directions are 75° and 30° using (2.1). It is observed that the leaky mode never transitions into a guided one due to the air

substrate. This leads to a very broadband design, which is well suited for the radar application to be discussed in the next chapter. A 290mm long prototype is built and shown in Fig. 2.5. The top conductor of the microstrip is made of an aluminum sheet (dark grey in Fig. 2.5). It is elevated from the ground plane by several pieces of foam (white in Fig. 2.5). The shorting plane is formed by using aluminum tape (light grey in Fig. 2.5) from the copper ground plane to the top conductor of the microstrip. The size of the ground plane is 30cm x 28cm. The antenna is edge-fed with a 10mm long 50Ω microstrip line connected to an SMA connector. The other end of the LWA is left open. The width of the microstrip is 9.6mm. The microstrip LWA is mounted on a rotator for the radiation pattern measurement. The cut along the $\phi = 0^\circ$ (defined with respect to the x-axis in the inset of Fig. 2.4) plane is measured using a broadband horn and a VNA from 5GHz to 10GHz. The prototype is further replaced by another identical broadband horn to calibrate the gain.

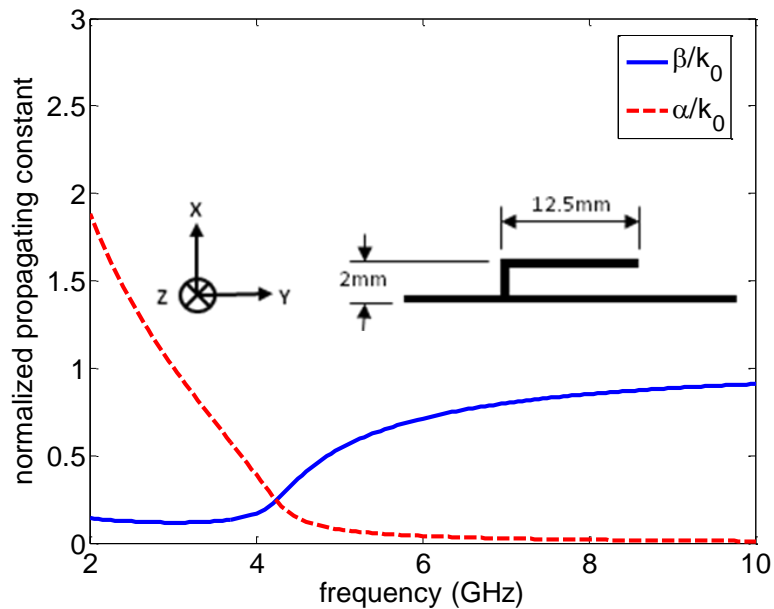


Fig. 2.4 Normalized propagating and attenuation constants of an air-filled half-width microstrip LWA structure versus frequency computed using TRM.



Fig. 2.5 The built prototype.

The same structure is simulated with the method of moments (MoM) full-wave solver in the commercial package FEKO [72]. The metal structures are simulated as PEC on an infinitely large ground plane. The excitation end of the simulation setup is shown as Fig. 2.6, where a TEM edge port is used to excite the microstrip. To verify the numerical convergence, the structure is simulated with four different sizes of triangle mesh at 10GHz, $\lambda_0/10$, $\lambda_0/15$, $\lambda_0/20$, and $\lambda_0/25$. The far field patterns simulated with different mesh sizes are plotted in Fig. 2.7. They show good agreements among the different discretization levels. The relative variations are computed by dividing the results of $\lambda_0/10$, $\lambda_0/15$, and $\lambda_0/20$ discretizations by the one computed with $\lambda_0/25$. They are shown in Fig. 2.8. The maximum deviation occurs near the direction of the back lobe, which is due to the backward traveling wave reflected by the far open end of the antenna. The relative error in the forward beam decreases as the mesh size is refined. However,

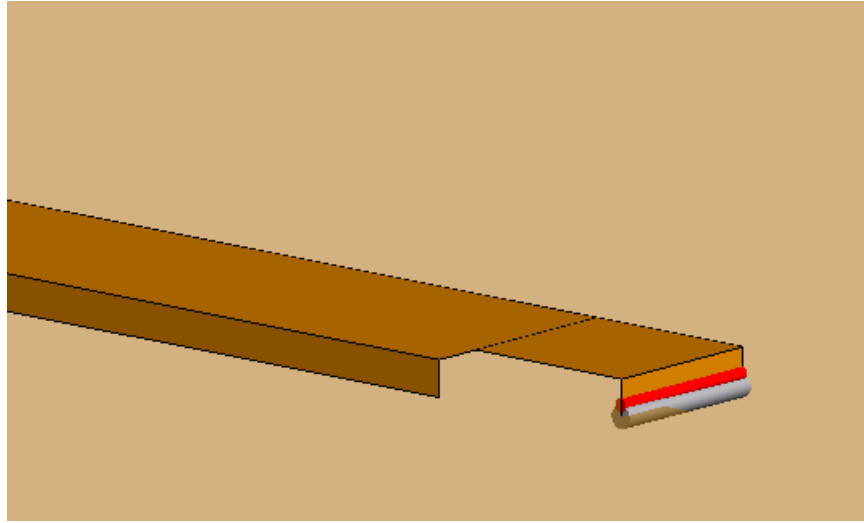


Fig. 2.6 FEKO simulation setup.

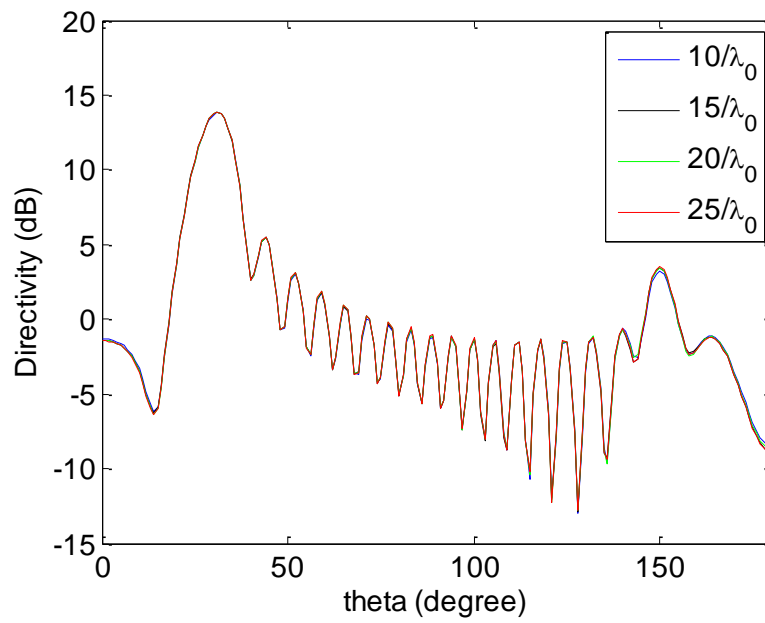


Fig. 2.7 The far field patterns using difference mesh sizes.

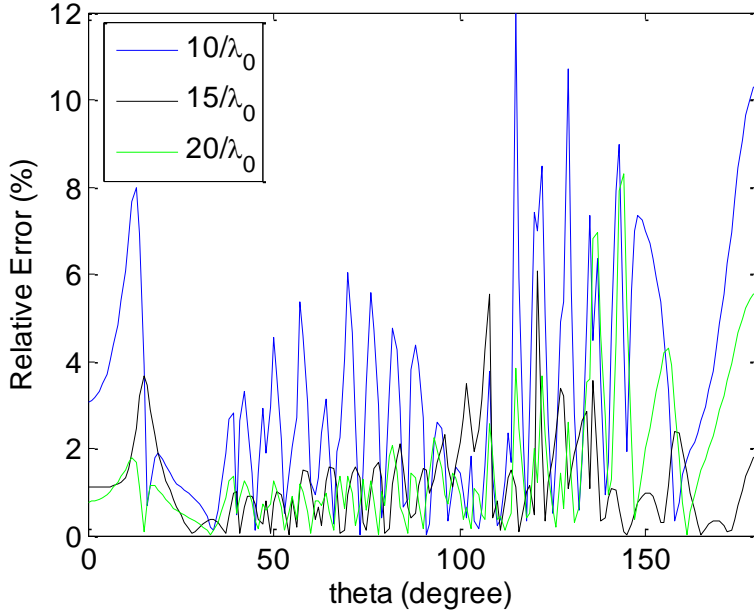


Fig. 2.8 The relative errors between the far field patterns at different directions using difference mesh sizes. $\lambda_0/25$ is used as the reference for each of the curve shown.

the relative errors around the back lobe direction improve slowly as the mesh density is increased. For some directions, such as $\theta = 136^\circ$ and 144° , the relative errors do not change with a definite trend as the mesh density is changed.

In addition to measurement and simulation, a third way to predict the radiation pattern of the antenna is to assume the aperture field based on the TRM results and then compute the radiated far field with an equivalent magnetic current model. The cross-section of a half-width microstrip LWA is shown in Fig. 2.9 (a). It is noted that the electric field of the leaky mode is distributed uniformly across the top and bottom conductors. Thus, it can be related to the excitation voltage directly as $E_x = V/h$. Next, a Huygens equivalent surface is chosen as the dash line in Fig. 2.9 (b). It covers the whole ground plane and the antenna structure. The equivalent magnetic current on this equivalent surface is related to the field in Fig. 2.9 (a) as $\vec{M} = \vec{E} \times \hat{n}$, where \hat{n} is the

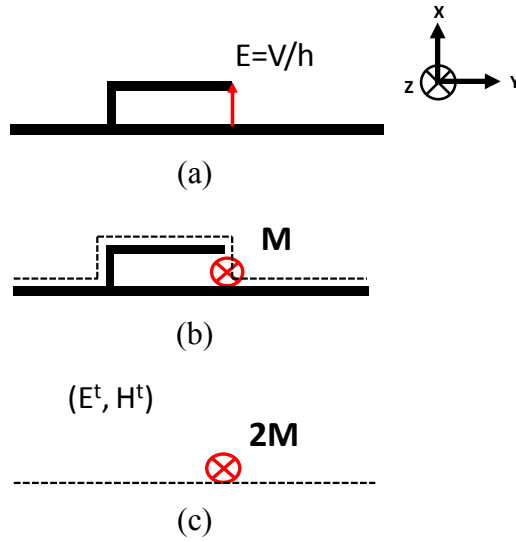


Fig. 2.9 The steps to derive the equivalent magnetic current model.

normal vector pointing outward on the equivalent surface. Since most of the original structure is PEC, the tangential electric field only exists on the radiating aperture, and E_x is turned into M_z . Lastly, the height of the microstrip is assumed to be negligible, thus allowing us to apply the image theory to remove the ground plane. The final field is due to $2M_z$ radiating in free space. It is noted that there are also equivalent electric currents everywhere on the equivalent surface. However, an electric current on a PEC surface does not radiate and they can be removed after we apply the image theory.

To compute the far field due to the equivalent magnetic current, the field strength and phase variation along the z -dimension are required. Since a microstrip LWA is also considered as a waveguide structure, all of the field components carry a $\exp(-j[\beta - j\alpha]z)$ factor, and so does the equivalent magnetic current. At last, the electric far field due to this equivalent magnetic line source can be computed using:

$$E_{\phi}^{ff}(\theta) = 2 \frac{V}{h} \cdot \frac{-jk_0}{4\pi} \cdot \sin(\theta) \int_0^L \exp[(-\alpha - j\beta + jk_0 \cos(\theta))z] dz \quad (2.10)$$

where L is the length of the antenna. The directivity pattern can be obtained by normalizing the far field pattern to the total radiated power, which can be computed by integrating the far field over the half-radiation sphere above the ground plane. Lastly, the field has no ϕ variation in this model since the only source is a magnetic line current, which produces an axial symmetrical field.

The radiation patterns from the measurement, FEKO simulation and TRM theory are compared in Fig. 2.10. The main beam regions at 5.5GHz, 7.5GHz and 10GHz are shown in this figure. It is clearly seen that the beam scans from the broadside to the endfire direction as frequency is increased. The gain also increases accordingly. These observations agree with the modal behavior described in the previous section. The measured main beam directions in θ are found to be 67° , 44° and 31° at the three

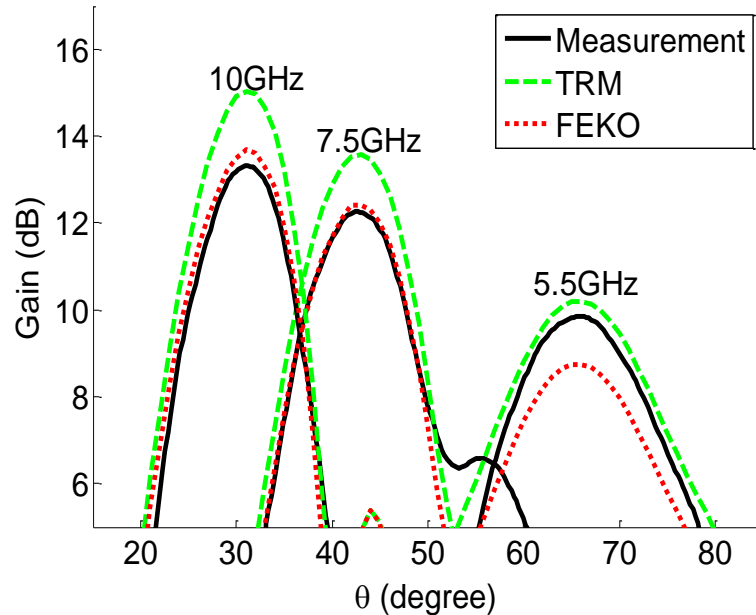


Fig. 2.10. Comparison of radiation patterns between TRM theory, simulation and measurement at three different frequencies. The patterns are plotted versus θ , which was defined with respect to the z-axis in Fig. 2.1.

frequencies. The measured gains are 9.8, 12.4 and 13.3 dBi, respectively. The results from FEKO and the measurement agree well for 7.5GHz and 10GHz. At 5.5GHz, the beam directions from FEKO and measurement are about the same, but the gain agreement is not as good. As for TRM, the beam directions are correct but the directivity values are always higher than the full-wave simulation and measurement results. The predicted gain values are 15.0, 13.6, 10.2dBi, respectively. It may be due to the effect of the feed radiation or the non-symmetrical ϕ -pattern in the actual structure, which were not accounted for in the equivalent magnetic current model discussed earlier.

2.3 CONCLUSION

In this chapter, the literature on microstrip LWA was reviewed. Among different designs, the half-width microstrip LWA was chosen for investigation since it does not require a dedicated excitation structure, which could limit the bandwidth of the antenna. The TRM analysis of the half-width microstrip LWA was summarized. A discussion about the proper choices of the wave numbers was also made. The propagation and attenuation constants of a half-width microstrip structure with a dielectric substrate were computed from 1GHz to 5GHz to discuss the relationship between the radiation properties and the mode characteristics. To verify these theoretical behaviors, a half-width microstrip LWA was built and measure. The propagation and attenuation constants were also computed using TRM from 2GHz to 10GHz. As frequency is increased from 5GHz, the propagation constant starts from nearly zero and approaches one. Correspondingly, the main beam scans from near broadside toward the endfire direction. At the same time, the attenuation constant decreases toward zero, leading to a more uniformly illuminated aperture. Thus, higher gain and narrower beam were observed at higher frequencies. Next, full-wave simulations were carried to compute the radiation

patterns of the built half-width microstrip LWA. Convergence of the full-wave simulation was also investigated. Lastly, an equivalent magnetic current model was discussed and used to compute the radiation patterns from the TRM results. The radiation patterns collected from the measurements, full-wave simulations, and the equivalent magnetic current model agreed reasonably well with one another. A frequency-scanned beam was clearly observed. In the following chapters, several broadband microstrip LWAs will be designed and applied to the human tracking problem in the 2-D range-azimuth plane.

Chapter 3: Tracking Multiple Humans Using Microstrip Leaky Wave Antennas

In this chapter, the frequency-scanned beam of a half-width microstrip LWA is investigated as a simple, low-cost means to achieve 2-D range-azimuth tracking of humans. First, the frequency bandwidth of a microstrip LWA is discussed in Sec. 3.1. This is an important parameter since a much finer range resolution is required to track humans as compared to typical radar targets such as vehicles and airplanes. A broadband microstrip LWA is then designed and built. The radiation pattern is measured and discussed. In Sec. 3.2, the radar concept is illustrated and the associated “target bandwidth” is discussed using the broadband radiation pattern. Afterwards, the processing algorithm is investigated using a point scatterer simulation. In Sec. 3.3, measurement data of stationary trihedrals and moving humans are collected and processed to demonstrate the tracking performance using a microstrip LWA. Sec. 3.4 is the conclusion.

3.1 BROADBAND MICROSTRIP LEAKY WAVE ANTENNA

The frequency-scanned beam of a microstrip LWA and its relationship with the mode properties were discussed in the previous chapter. In this chapter, another important aspect of a microstrip LWA, the frequency bandwidth, is discussed in detail. For most antennas, the bandwidth is defined across the frequencies in which the return loss is greater than a predefined level, such as 10dB. However, the bandwidth of an LWA can be interpreted from a modal perspective. A “radiation bandwidth” can be defined for individual modes. To discuss the idea, the normalized propagation and attenuation constants of three leaky modes on a half-width microstrip LWA with $W/2 = 15\text{mm}$, $h = 0.5\text{mm}$, $\epsilon_r = 4.4$ are plotted in Fig. 3.1. The propagation constants are the

solid curves and the attenuation constants are the dashed curves. The blue, red, and green curves correspond to the three modes in an increasing mode order. The onset frequency of a leaky mode is defined as the frequency where the propagation and attenuation constants are equal. For the three leaky modes in Fig. 3.1, the onset frequencies are 2.3GHz, 7GHz, and 11.7GHz, respectively. The latter two are approximately three times and five times the onset frequency of the lowest order leaky mode. These numbers correspond to the odd order modes on a conventional microstrip LWA. As discussed in Chapter 2, a half-width microstrip LWA can be considered as a conventional microstrip LWA with a vertical PEC symmetry plane inserted at the center of the structure. Thus, only the modes with an odd symmetry on a conventional microstrip LWA can be excited on the half-width design. For each mode, the normalized propagation constant asymptotically approaches the square root of the dielectric constant as the frequency is increased. Moreover, a leaky mode only radiates from the onset frequency to the critical frequency where the propagation constant is equal to the free space wave number. The mode transitions into a guided one above this critical frequency. In Fig. 3.1, it can be observed that the radiating bandwidth of the individual leaky mode is quite narrow. This “radiating bandwidth” gets broader as the order of the mode gets higher. Nevertheless, the frequency bandwidth of a microstrip LWA with a $\epsilon_r = 4.4$ dielectric substrate is not sufficient for the human tracking application.

For comparison, the propagation and attenuation constants of leaky modes on the same geometry but with an air-filled substrate are plotted in Fig. 3.2. The line styles and colors in this figure are labeled in the same way as Fig. 3.1. The onset frequencies of the two lowest modes are 4.7GHz and 14.3GHz, which are about 2.1 times the onset frequencies of those in Fig. 3.1, where a dielectric substrate with $\epsilon_r = 4.4$ is used. This 2.1 factor is the square root of the dielectric constant. It is also observed that the

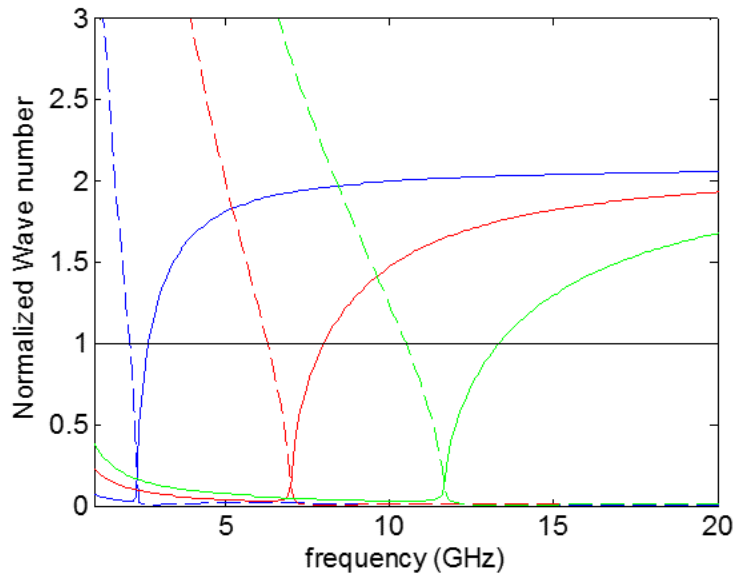


Fig. 3.1 The propagation and attenuation constants of the higher order leaky modes on a half-width microstrip LWA with $\epsilon_r = 4.4$. The propagation constants are the solid curves and the attenuation constants are the dashed curves.

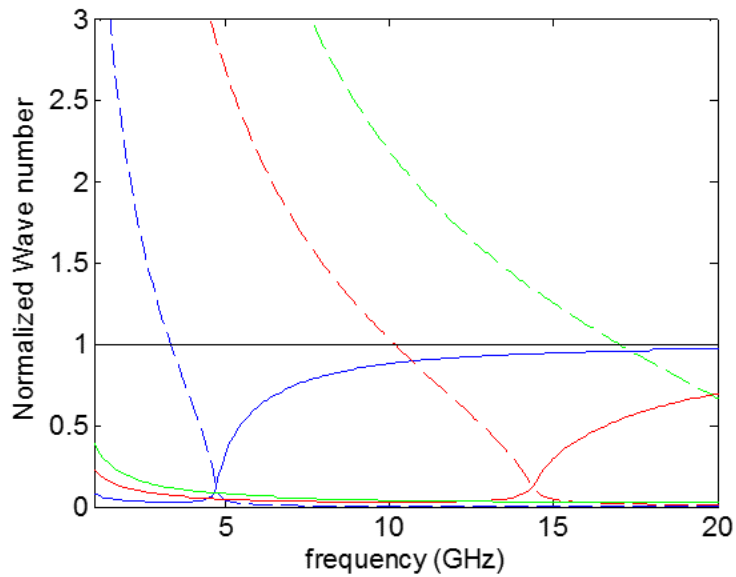


Fig. 3.2 The propagation and attenuation constants of the higher order leaky modes on a half-width microstrip LWA with $\epsilon_r = 1$. The propagation constants are the solid curves and the attenuation constants are the dashed curves.

propagation constant is never greater than the free space wave number, plotted as the horizontal black line, for the air-filled design. This observation indicates that the modes never become guided. In theory, a leaky mode on an air-filled microstrip LWA has an infinite bandwidth. However, it is still preferred to operate the antenna with only a single leaky mode across the frequency band, since frequency-scanned properties of different modes are totally different. In summary, the proper operating bandwidth of this air-filled antenna is from 4.7GHz all the way to 14.3GHz, between the onset frequencies of the two lowest order leaky modes. It corresponds to a 1:3 frequency bandwidth ratio. This broad operating bandwidth is well-suited for the human tracking application.

An air-filled microstrip is built using a milling machine with a modified geometry as shown in Fig. 3.3. The thin copper plate is the top microstrip. The width of the top microstrip ($W/2$) is 15mm and it is suspended 2mm from the ground plane. The aluminum metal block on the left serves the role of the symmetry plan. It is extended vertically to better preserve the field distribution outside the microstrip and to mechanically anchor the copper plate. The antenna prototype is 290mm long and it is mounted on a 260mm wide and 320mm long ground plane, which is made from steel. The structure is excited from an SMA connector directly soldered to the microstrip (at the far end in Fig. 3.3). The propagation and attenuation constants of the built structure are computed using TRM and plotted as the solid and dashed curves in Fig. 3.4. The mode has an onset frequency of 4.3GHz. As frequency is increased from 4.3GHz to 8GHz, the normalized propagation constant changes from 0.24 to 0.85. The beam is expected to steer from 74.7° to 32.1° using the cosine formula in (2.1). Correspondingly, the normalized attenuation constant decreases from 0.24 to 0.02, indicating a higher gain and narrower beamwidth at higher frequencies.

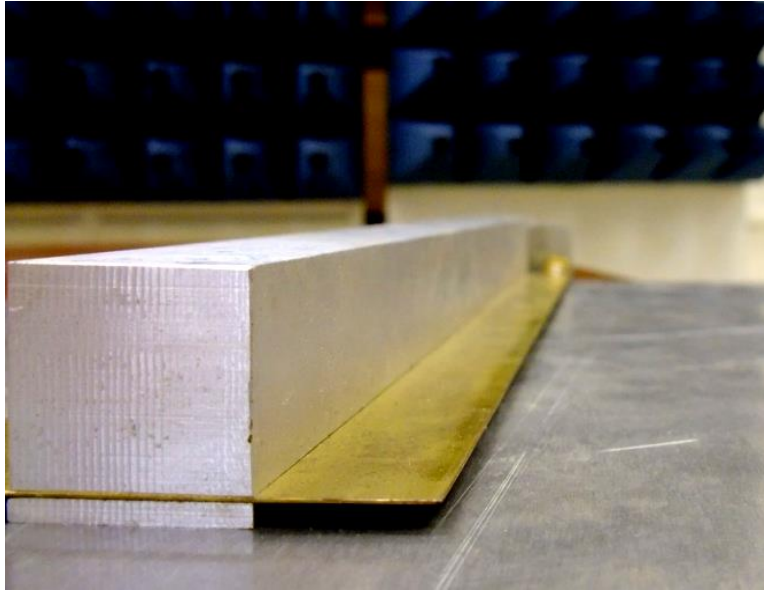


Fig. 3.3 The built half-width microstrip LWA prototype. The far end is an SMA connector with the center tip directly soldered to the top microstrip.

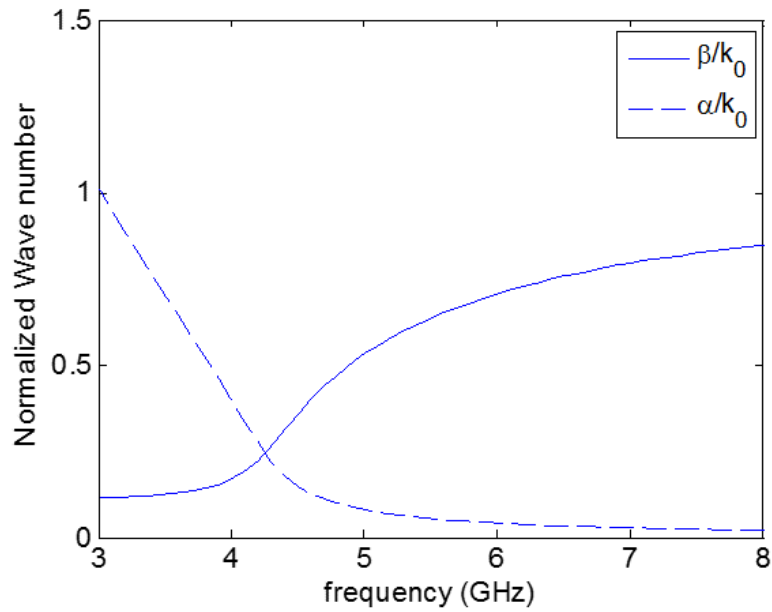


Fig. 3.4 Propagation and attenuation constants of the built prototype calculated using TRM. The structure parameters are $W/2 = 15\text{mm}$, $h = 2\text{mm}$, and $\epsilon_r = 1$.

The broadband gain pattern of the built prototype is measured with the same setup described in Chapter 2. The result is shown in Fig. 3.5. The measured pattern is plotted as a function of both frequency and angle (defined with respect to the longitudinal direction of the antenna). Each horizontal cut in Fig. 3.5 is the gain pattern in the ϕ -direction at a fixed frequency, showing the main beam direction, gain, and beamwidth. The figure is color coded from 0dBi to 15dBi. As frequency is increased from 4.3GHz to 8GHz, the main beam steers from 70° to 33° , which are in acceptable agreement with the TRM predictions. The antenna gain also increases from 6.6dBi to 12.2dBi, while the 3dB beamwidth decreases from 20.5° to 14.2° . In addition, it is observed that the beam scans less at higher frequencies. This corresponds to the slower changing propagation constant at higher frequencies in Fig. 3.4. Hence, we only operate this antenna from 4.3GHz to 8GHz for direction finding, since the antenna does not scan much beyond 8GHz.

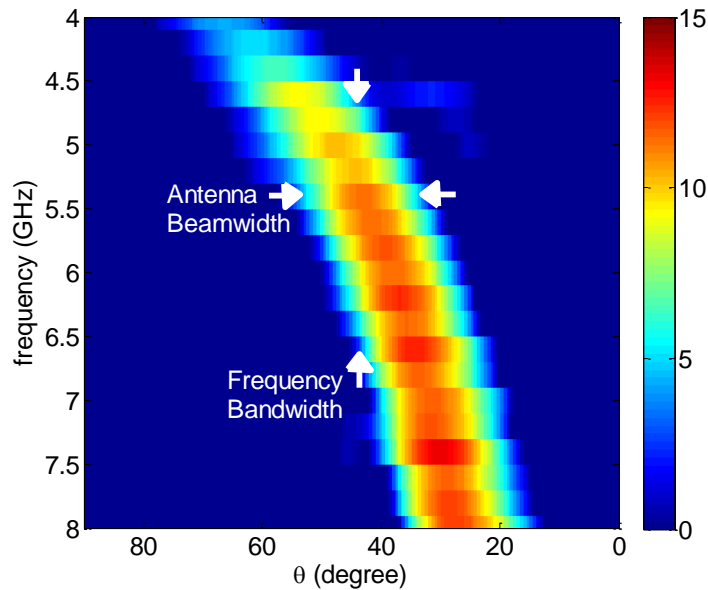


Fig. 3.5 Measured antenna gain pattern plotted as a function of frequency and azimuth angle. The gain value is color coded from 0 to 15dBi.

3.2 RADAR CONCEPT AND PROCESSING ALGORITHM

The concept of using the frequency-scanned beam of a microstrip LWA for range-azimuth tracking is illustrated in Fig. 3.6. In the illustration, the beam is pointed toward two different targets at 5GHz and 8GHz. Therefore, the received frequency response from the radar will show two peaks at these two frequencies. In practice, the peaks in the radar frequency response have a certain bandwidth since the beamwidth of the antenna is finite. This relationship is shown by the white arrows in Fig. 3.5 – the horizontal arrows mark the beamwidth of the antenna and the vertical arrows show the corresponding bandwidth when a target exists in that particular direction. When the antenna beam scans across θ as the carrier frequency is changed, the target is illuminated by multiple frequencies. As a result, this bandwidth can be explored for ranging and it varies for targets at different directions. A direction-dependent “target bandwidth” can be defined correspondingly. The concept of “target bandwidth” is quite different from most antenna bandwidth, which could be defined by the frequency range in which the return loss, gain, or axial ratio varies within a predefined range. In these traditional definitions, the beam

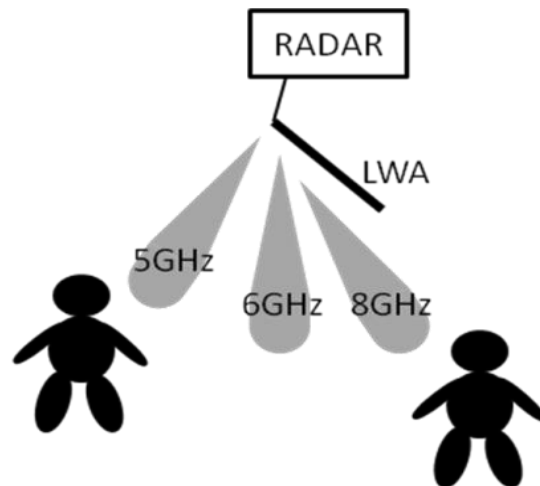


Fig. 3.6 Illustration of the radar concept. The frequency-scanned pattern of the microstrip LWA is used to track humans.

direction is assumed to be independent of the operating frequency. This is certainly not the case for a frequency-scanned antenna. Furthermore, the “target bandwidth” and the “mode bandwidth” discussed in the previous section are two different concepts. The former could be further related to the radar range resolution in that direction and the latter is related to the total bandwidth in which the antenna can radiate. In summary, when a radar target is measured with a frequency-scanned antenna, the amplitude of the frequency response contains the bearing information since frequency peaks are expected corresponding to the directions of targets. In addition, the range information of individual target is contained in the phase response across the frequency bandwidth around the corresponding frequency peak. If the collected signal is processed properly, we should be able to achieve simultaneous ranging and azimuth determination within a single frequency scan.

To develop the processing algorithm for a frequency-scanned antenna to resolve multiple targets, the radar response with two targets in a scene is simulated and examined using the point scatterer model. The radar is assumed to transmit and receive using the same frequency-scanned antenna with gain $G(f, \theta)$, which can be computed using the equivalent magnetic current model discussed in Chapter 2 assuming no metal loss. The transmitter and receiver are assumed matched to the same impedance. Thus, the received power from individual targets can be computed using the radar equation and then converted into voltages. Lastly, the receiving voltages from different targets are weighted with the proper delay and summed as:

$$\frac{V^r(f)}{V^i(f)} = (1 - |\Gamma_{11}|^2) \sum_{i=1}^n \frac{\lambda(f) \sqrt{\sigma_i} G(f, \theta_i) e^{-j2k(f)R_i}}{(4\pi)^{3/2} R_i^2} \quad (3.1)$$

where (R_i, θ_i) and σ_i is the position and radar cross-section (RCS) of the i -th point scatterer. Γ_{11} is the S11 of the antenna. V^i is the excitation voltage and V^r is the total received voltage. In the simulation setup, two targets with unit RCS are placed at $(4\text{m}, \theta = 55^\circ)$ and $(5\text{m}, \theta = 40^\circ)$ from the antenna, respectively. The corresponding main-beam frequencies based on the TRM model are 5.2GHz and 6.7GHz. This setup is simulated using (3.1) assuming $V^i = 1$ and $\Gamma_{11} = 0$. The simulated frequency response is plotted in Fig. 3.7(a). Two frequency peaks at 5.2GHz and 6.7GHz are clearly seen, indicating the targets are already resolved in the azimuth dimension. In addition, some small oscillations are also observed. They are due to the phase interference from the different ranges of the two targets. Fig. 3.7(b) shows the range profile after the frequency response is inverse Fourier transformed into the range domain. Two targets at 4m and 5m are clearly observed. This shows that the different range positions of the targets indeed can be extracted from the phase of the received radar signal. From Fig. 3.7(a) and Fig. 3.7(b), the bearing and range information about the two targets are retrieved. However, there is still a correspondence problem since the observed responses in range and frequency respectively are the projections of all targets into a single dimension. To obtain the range and bearing information simultaneously, it is proposed that we separate the targets in range first before determining their corresponding bearings, since the range response of a target is much sharper than the frequency response comparing Fig. 3.7(a) and Fig. 3.7(b). The processing is accomplished by using a window in range to gate out the range response of a single target first, and then Fourier transforming it back to the frequency domain to determine the bearing of that particular target. Two range gates are illustrated in dashed lines in Fig. 3.7(b). Fig. 3.7(c) shows the resulting range-gated frequency responses of the two targets. The 5.2GHz and 6.7GHz frequency peaks are clearly observed. Such processing also removes the small oscillations in Fig. 3.7(a) due to the

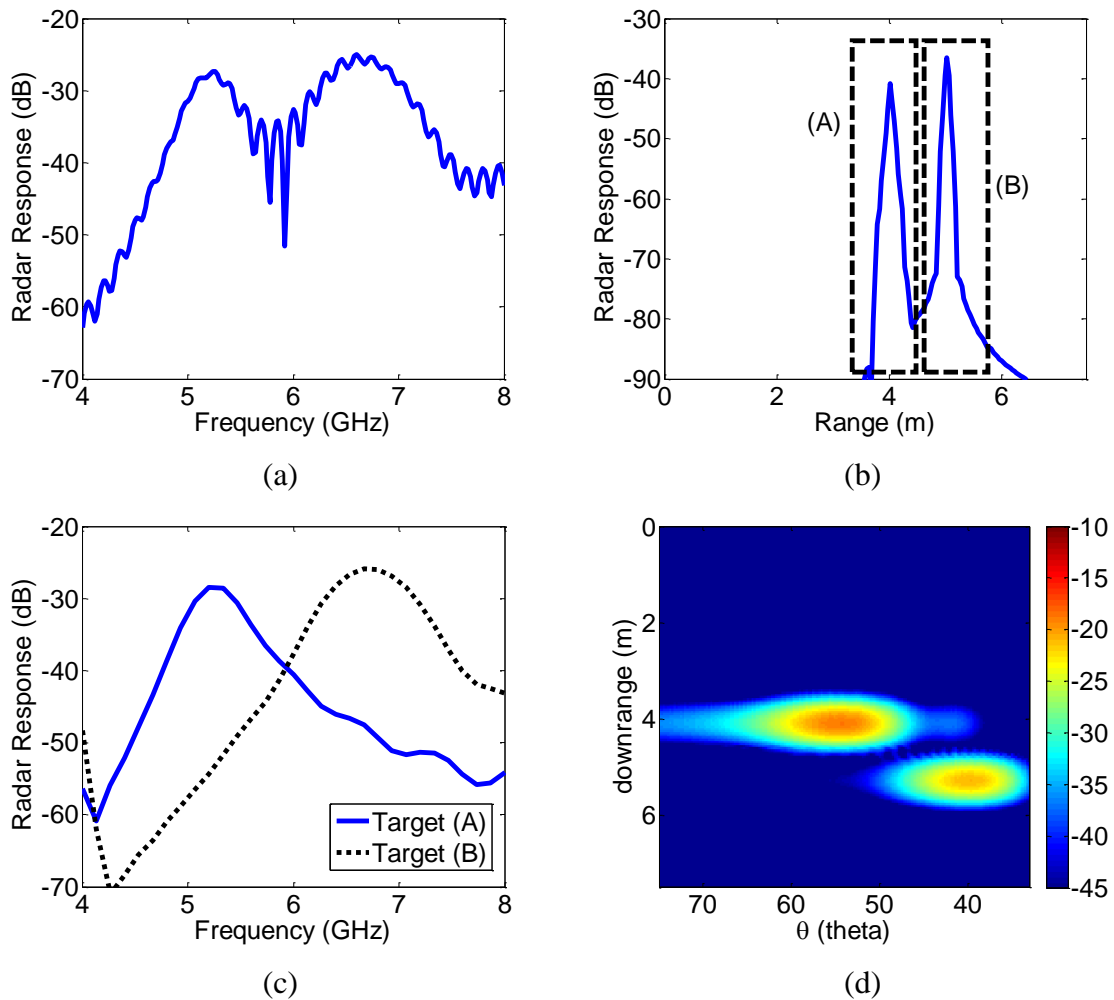


Fig. 3.7 Simulation results based on the point scatterer model. (a) Frequency response of two targets located at different azimuth angles and distances to the antenna. (b) Range profile obtained after the inverse Fourier transform. (c) Range-gated frequency responses for windows (A) and (B) in (b). The individual frequency responses can be used to estimate target bearings. (d) Final range-azimuth image of the simulated scene.

interference from the other target. The range-azimuth positions of the two targets are successfully identified at (4m, $\theta=55^\circ$) and (5m, $\theta=40^\circ$). In the actual implementation, a sliding range window is used to repeatedly generate the frequency (or bearing) response at different range locations. As a result, a two-dimensional range-azimuth image (top-

view of a scene in polar coordinates) can be obtained in this manner. This processing is very similar to the short-time Fourier transform (STFT), which is usually applied to a collected time sequence to analyze the time-varying Doppler frequencies of the radar return. Mathematically, this operation can be written as:

$$X(t, f(\theta)) = \int x(t)w(\tau - t)e^{-j2\pi f(\theta)\tau} d\tau \quad (3.2)$$

where $x(t)$ is the received range profile and $w(t)$ is a window function. In (3.2), the time variable is related to range via the usual $t = 2 * range/c$ formula where c is the speed of light in free space. Fig. 3.7(d) shows the resulting image by using a sliding 113-cm Hamming window. The two targets are resolved in the final range-azimuth image, with the first target at 4m and $\theta = 55^\circ$ and the second target at 5m and $\theta = 40^\circ$. As demonstrated in Fig. 3.7, the antenna beamwidth and “target bandwidth” can be exploited simultaneously using the proposed algorithm. Only a single wideband frequency scan is required to form a 2-D range-azimuth image. This is an important feature for tracking fast moving targets, such as human subjects.

It is noted that a system combining a frequency scanned antenna and an FMCW radar was investigated in [73] for 2-D range-azimuth imaging. The bearing information was first derived from the intermediate frequency of the demodulated waveform. The range was then found through multiple transmitted waveforms with different frequency slopes. This approach requires a long acquisition time since multiple waveforms are required to determine a single range. For comparison, the proposed algorithm can determine the range within a single frequency scan.

To summarize, the steps for generating a range-azimuth image using a microstrip LWA are as follows. First, the collected wideband frequency response is inverse Fourier

transformed to the range domain to reveal the targets. Second, a sliding window is applied to resolve the targets in range. Third, the gated range response is Fourier transformed back to the frequency domain as an azimuth scan at this particular range. Finally, the frequency response is mapped into the azimuth response using the (carrier frequency)–(main beam direction) relationship established in Fig. 3.5. It is noted that the achievable range resolution of the microstrip LWA-based radar is different for targets located at different azimuth directions. This can be seen from Fig. 3.5, where the “target bandwidth” gets narrower as the operating frequency is lowered. Since the range resolution is inversely proportional to the target bandwidth, the coarsest range resolution occurs at the lowest operating frequency, or when the beam is closest to broadside. For the microstrip LWA under consideration, it is estimated that the range resolution to be approximately 50cm at 4.3GHz, or $\theta=70^\circ$. This is the worst case range resolution of the system. It is noted that the antenna beamwidth is also the broadest near the broadside direction. Thus, a target near the broadside of the antenna will experience both the coarsest range resolution and the coarsest azimuth resolution.

3.3 RADAR MEASUREMENTS

A measurement is first carried out using two stationary trihedrals to validate the processing algorithm. Four half-width microstrip LWAs were fabricated into two pairs. They were used in an earlier interferometry application [74]. In work, the two pairs are mounted 60cm apart on the same ground plane as shown in Fig. 3.8 to alleviate self-jamming, since a VNA is used in the continuously transmitting mode. The antennas have the same structure as the one shown in Fig. 3.3. The outer most two antennas are used for the measurement since they have the least coupling. A wood frame, a vise, and a clamp are used to hold the large ground plane vertically. A VNA is used to collect S21 data

from 4GHz to 8GHz in 401 points. The antenna z-axis is tilted with respect to the normal vector to the scene being imaged to best utilize the scanning range of the microstrip LWA from 33° to 70° (see Fig. 3.6). Two identical trihedrals shown in Fig. 3.9 are placed at positions similar to the simulated scene. Data measured with the trihedrals in the scene are subtracted with the data measured without the trihedrals to remove static clutters and residues of self-jamming. The subtracted data are processed with a 113-cm Hamming window and the result is shown in Fig. 3.10. The two trihedrals are clearly resolved in the range-azimuth plane. The target azimuth responses are slightly broader in the measurement than in the point-scatterer simulation. It is due to the physical size of the trihedral, 16cm per side, as shown in Fig. 3.9.



Fig. 3.8 The antenna and measurement setup.



Fig. 3.9 The trihedral target, which is 16cm per side.

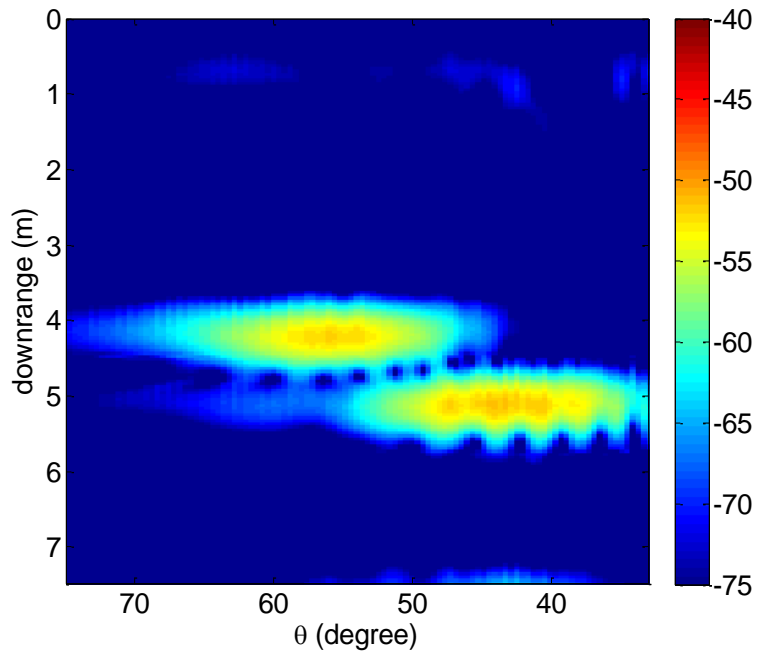


Fig. 3.10 Range-azimuth image generated from measured data of two stationary trihedrals. The two trihedrals are placed at positions similar to the simulated scene in Fig. 3.7.

Next, results of outdoor moving humans are collected. To continuously track moving targets, a script is programmed to automatically save the measured data and restart the next frequency scan. The VNA continuously collects frequency sweeps of S21 data from 4.3GHz to 8.3GHz in 401 points with a 2.5Hz repetition rate. The corresponding unambiguous downrange from the frequency sampling is 15m. An average frequency scan of the whole sequence is computed and stored as the background for all frames. Afterwards, each frequency scan is subtracted with the background data and processed with a sliding 113-cm Hamming window. In the measurement, one human subject (subject A) walks around a circle in the clockwise direction while the other human subject (subject B) walks in the counterclockwise direction. A photo of the two human subjects walking is shown as Fig. 3.11. Four markers were placed on the ground to guide the circular movements.



Fig. 3.11 Snapshot of the two-human tracking measurement.

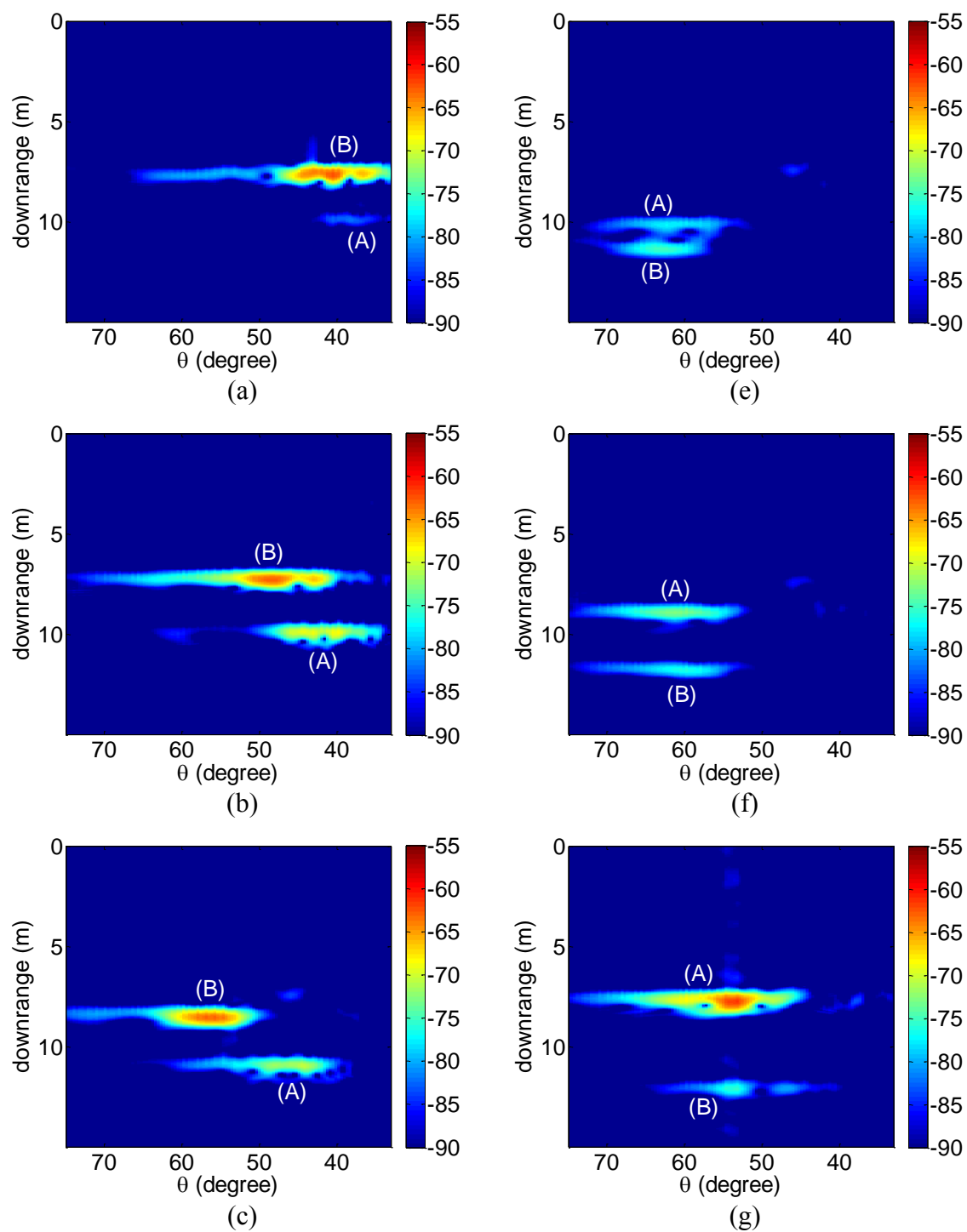


Fig. 3.12 Range-azimuth snapshots from a continuous human tracking measurement. Subject (A) walks in the clockwise direction while subject (B) walks in the counterclockwise direction.

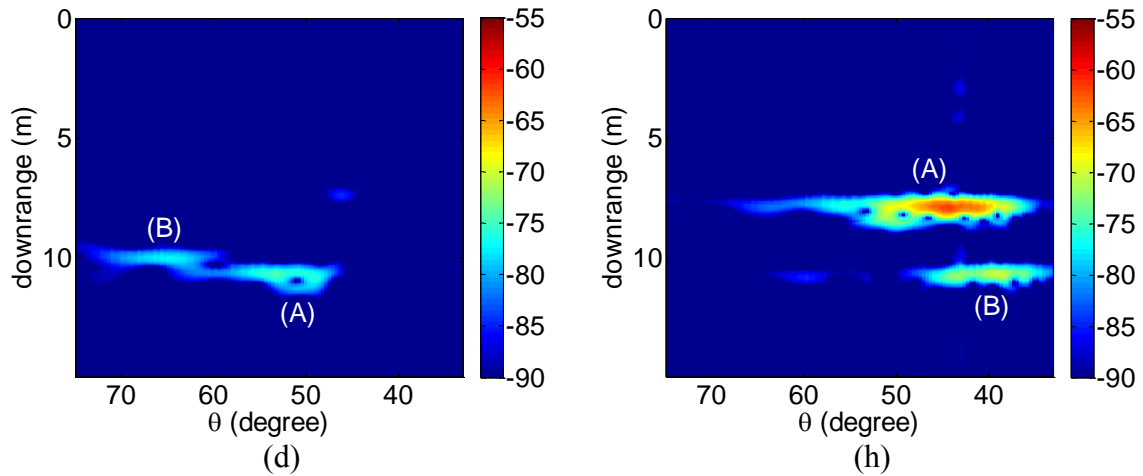


Fig. 3.12 Range-azimuth snapshots from a continuous human tracking measurement. Subject (A) walks in the clockwise direction while subject (B) walks in the counterclockwise direction.

Fig 3.12(a) - Fig 3.12 (h) show eight snapshots from the measurement of two human subjects. The snapshots are spaced by 1.5-second intervals and the color indicates the strength of the return. Their positions can be clearly identified in the sequence of images in Fig 3.12 (a) - Fig 3.12 (h). The subject (A) is observed moving in the clockwise direction and the subject (B) moving in the opposite direction. It is noted that propagation loss is not compensated for in these images. Thus, the farther target shows a weaker response. The azimuth extent of the farther target is also smaller due to the effect of amplitude threshold. Across these figures, the target strength is stronger near the endfire direction, indicating the frequency-dependent antenna gain overpowers the more path loss at higher frequencies. In addition, some shadowing effect can be observed when two targets are at the same azimuth direction. For example, the return from subject (A) is substantially weaker in Fig 3.12 (a) than in Fig 3.12 (b) due to the shadow cast by subject (B). Overall, the microstrip LWA achieves real-time 2-D range-azimuth tracking of two humans using the proposed algorithm.

3.4 CONCLUSION

In this chapter, the concept of tracking multiple humans in the range-azimuth plane using a simple microstrip LWA has been investigated. First, the frequency bandwidth of the leaky modes were discussed from the modal perspective. A broadband air-filled half-width microstrip LWA was designed, built and measured. The frequency bandwidth during the beam dwell on a target was explored to achieve simultaneous ranging and direction finding. Furthermore, the concept of “target bandwidth” was discussed using the measured broadband radiation pattern. It was further related to the range resolutions in different directions. A processing algorithm was developed based on a point scatterer simulation to generate the range-azimuth (top-view) image of a scene. It entailed separating targets in the range domain before their frequency responses were used to estimate the azimuth bearing. A stationary trihedral measurement was carried out to validate the proposed algorithm. An outdoor two-human measurement was presented to demonstrate the tracking performance. In summary, it has been demonstrated that tracking multiple targets in the range-azimuth plane can be achieved with only two microstrip LWAs and two broadband transceivers. The proposed approach achieves simultaneous ranging and direction finding within a single frequency scan. It is well suited for moving targets, such as humans.

Chapter 4: Combining a Frequency-scanned Antenna with a Short-Pulse Radar for 2-D Imaging

4.1 INTRODUCTION

A frequency-scanned antenna is a simple and low-cost way to achieve electronic beam scanning for radar applications. In the previous chapter, the frequency-scanned beam of a MLWA and its frequency bandwidth during the beam dwell were exploited to achieve range-azimuth imaging. It was demonstrated that the 2-D image of a scene can be generated with only a single frequency sweep of a VNA. A stepped-frequency radar system operate in the frequency domain, and the incorporation of a frequency-scanned antenna frontend is quite natural. However, the image refresh rate may be limited by the settling time of the voltage-controlled oscillator in an FMCW radar or the locking time of the phase-lock-loop in a VNA to synthesize the stepped frequencies. In comparison, a short-pulse radar may enable a higher image acquisition rate, which is needed for imaging movers like humans. However, the integration of a frequency-scanned antenna and a short-pulse radar requires additional considerations.

In this chapter, the integration of a half-width MLWA [51] with a short-pulse ultra-wideband (UWB) radar is explored to achieve real-time 2-D imaging of a scene. The short-pulse radar system investigated is the P410 from Time Domain Corporation [75]. An introduction about the hardware architecture of the P410 is presented first. The frequency-domain response of the P410 and the circulator to be used in the system are characterized individually. Next, a new half-width microstrip LWA is designed to match the frequency bandwidth of the P410 and to achieve a narrower beam. The direction-finding capability of the combined system is verified through measurement and full-wave simulation. Afterwards, the STFT is used to form images in both line-of-sight and through-wall measurements of a walking human to demonstrate the 2-D imaging

capability of the resulting system. Lastly, a discussion of the combined frequency-scanned antenna and short-pulse radar system is made.

4.2 THE P410 SHORT-PULSE UWB RADAR

The P410 radar transmits modulated pulses at a pulse repetition frequency (PRF) of 10MHz. The nominal bandwidth of the radar is from 3.1GHz to 5.3GHz and the pulse shape was engineered to meet the Federal Communications Commission (FCC) UWB Mask [76]. As a result, the pulse width of the transmitted waveform is about 2ns, broader than the 0.5ns pulse width had all the in-band frequency components been used equally. Usually, it would require a heterodyne receiver with a broadband Analog-to-Digital Converter (ADC), 2.2GHz of bandwidth in this example, to sample the received waveform without aliasing. However, such ADC usually consumes a lot of power and the number of bits is limited. Different sampling schemes have been proposed, such as subsampling [77] and equivalent time sampling [78, 79, 80]. In the P410, Time Domain Corporation utilizes a 12-finger rake-receiver as shown in Fig. 4.1. The received waveform is sampled with a fast switch, which can be programmed to only a few picoseconds. However, the delay between fingers is fixed at 61.1ps. A range scan is generated by stepping through the programmable delay across the entire desired range. As a result, multiple pulses are required to form a single range scan, while a system with a heterodyne receiver and a broadband ADC can form a range scan at the rate of the pulse repetition frequency. The time to form a single range scan with 61.1ps step size is:

$$T_{scan} = (\# \text{ of range bins}) \times \left(\frac{1}{10MHz}\right) \times \left(\frac{1}{12}\right) \times (\# \text{ of Integration}) \quad (4.1)$$

where pulse integration is utilized to improve the signal quality. There are other limitations for such an approach. For example, the size of the range bin is fixed to 61.1ps

and the number of range bins to be collected must be an integer multiple of 96. It is also noted that the transmitted pulse sequence is pseudo-random coded (it is called channel coding by Time Domain Corporation) to overcome the intrinsic 15m unambiguous downrange (due to the 10MHz PRF) as well as to achieve a smoother spectrum content from the repeated pulses to avoid interfering with other wireless systems. The main advantages of such an approach using a rake receiver are less power consumption and the option to use an ADC with a high dynamic range. The bandwidth requirement of the ADC is reduced from 2.2GHz (the frequency bandwidth of the pulse) to 10MHz (the pulse repetition frequency) in the rake-receiver. Thus, a high dynamic range ADC can be implemented using over-sampling and sigma-delta techniques. A high dynamic range ADC also eliminates the need of a variable-gain-amplifier (VGA) in the P410, which usually degrades the noise performance. Moreover, a high-dynamic range ADC is important for performing background subtraction in the signal processing stage, which is critical for the human tracking problem since the environment will cause a strong static clutter.

In order to operate the P410, two antennas are required to connect to the two SMA connectors on it for transmitting and receiving, respectively. The radar receives user control commands and transfers the whole range scan (with optional motion filtered response or target detection) to the controlling computer through a USB cable. The P410 unit used in this dissertation comes with an optional power amplifier. The output power can be varied from -14.5dBm to 1dBm. It is noted that -14.5dBm is the highest level permitted by FCC and any level higher than that can only be used for research purpose. Lastly, the dimension of a P410 is only 12cm × 9cm × 3.5cm and it can operate tens of hours with a fully charged lithium-ion battery pack. Therefore, the unit is highly portable.

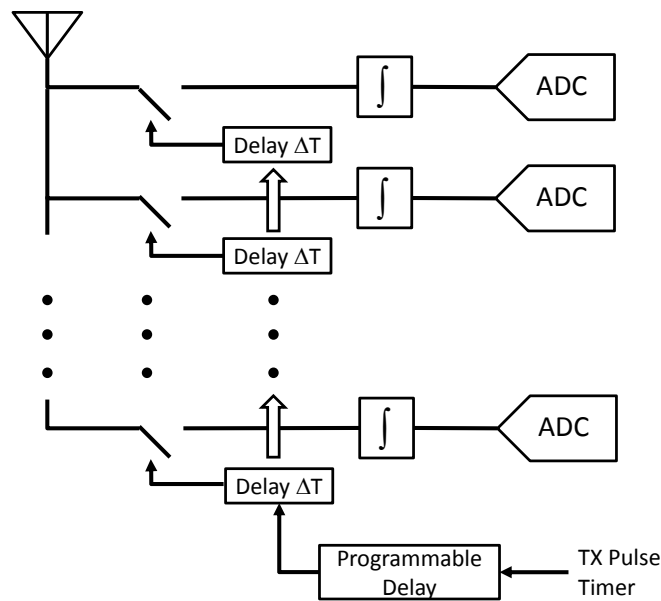


Fig. 4.1 The rake-receiver architecture

The range scan (or range profile) of a trihedral target (16cm per side) was collected indoors and is plotted in Fig. 2. The range scan from 0ns to 152.3ns is collected with a P410 unit set to a transmit power of -14.5dBm and the number of pulse integrations of 2^{15} . The raw range scan shows the trihedral at 50ns and a strong early-time return that saturates the receiver. There is also a lot of room clutter between 30ns to 80ns. Lastly, there is a weak return around 110ns, which corresponds to the 15m raw unambiguous down range. As mentioned previously, the transmitted pulse sequence is pseudo-random coded to overcome the intrinsic unambiguous range, i.e. it can detect a target at a distance more than 15m away from the radar without confusing it with a target within 15m from the radar. However, the transmitter experiences jamming every time a new pulse is transmitted, which occurs at a rate of 10MHz. This “noise band” can be mitigated by pulse integration, which is set to the maximum in Fig. 4.2.

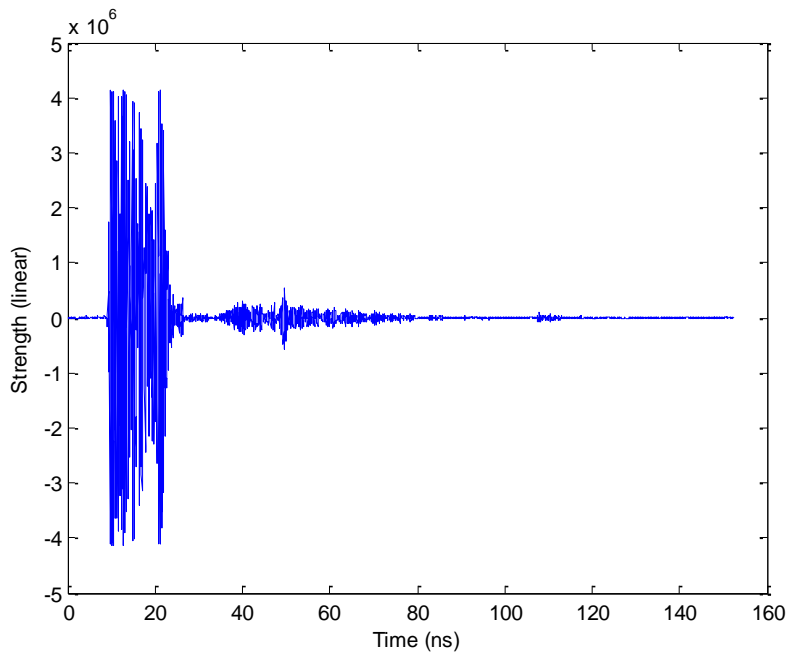


Fig. 4.2 The raw range scan of a trihedral in the scene.

The early time jamming will contaminate the return of a close-in target and requires further discussion. It can be explained in terms of bouncing diagram as shown in Fig. 4.3. The mismatches of the antenna and the low-noise-amplifier are assumed to be -10dB and there is an internal coupling between the power amplifier (PA) and the LNA. The coupling creates the very first return at the receiver side and this pulse is reflected by the input port of the LNA toward the antenna. The reflected pulse travels down the cable and is further reflected toward the receiver by the mismatch of the antenna. As a result, the receiver will experience a delayed pulse with 20dB weaker amplitude compare to the first pulse due to the coupling. The attenuation is the combination of the mismatches of the LNA and the antenna. The time delay between the two pulses is twice the time to travel the length of the cable. Over time, the receiver will experiences a series of pulses,

of which the amplitudes are 20dB weaker consecutively. Moreover, other mechanisms also introduce jamming. The reflection from the transmitting antenna can couple to the receiver through internal coupling and there is also coupling between antennas. All these pulses are sent directly from the PA thus the power level saturates the receiver and requires a while to damp out. This renders the first 20ns of the down range meaningless within the 100ns unambiguous down range as shown in Fig. 4.2. This can be mitigated by using a very short cable, better matched antennas and less coupling between antennas. Further improvements can be achieved in the transceiver with less internal coupling and better matched LNA and PA. It is noted that the received pulse from the target will experience a similar bouncing mechanism along the receiving cable and produce multiple peaks in the down range. There is a potential problem that weak targets are masked by the multiple peaks of a strong target.

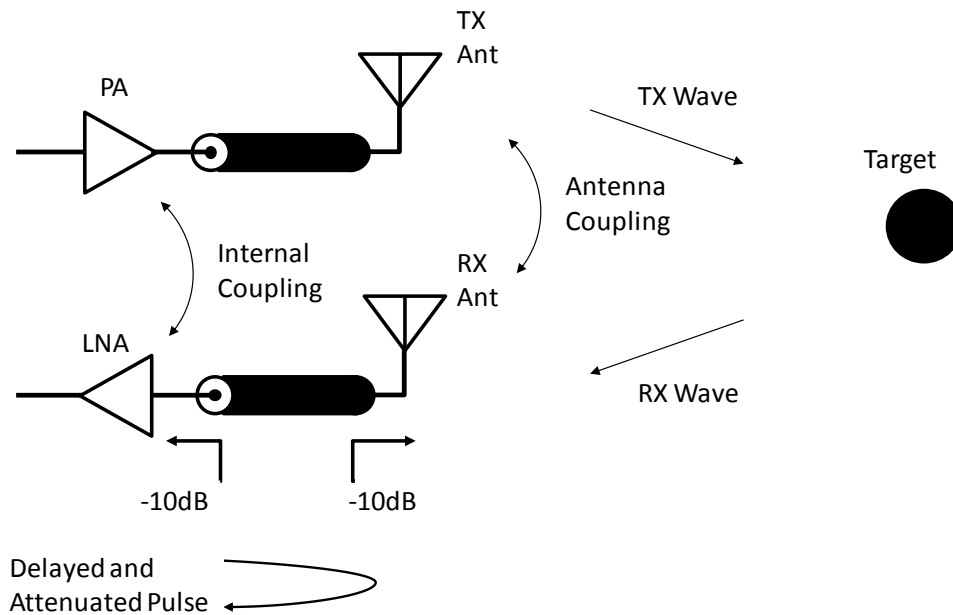


Fig. 4.3 The mechanisms of the early-time jamming.

4.3 A LONG MICROSTRIP LEAKY WAVE ANTENNA FOR THE P410

A half-width MLWA is used as the frequency-scanned antenna due to its simplicity and compact size [51]. The antenna consists of a top microstrip, a side shorting plane, and a ground plane. Air substrate is chosen for a broadband operation from 3.1GHz to 5.3GHz, which is the equivalent frequency bandwidth of the radar. The length of the antenna is chosen to be 90cm to achieve a narrower beam. The cross-sectional dimensions of the antenna are then designed using TRM to satisfy two design criteria. First, the attenuation constant across the band must ensure that at least 90% of the input power is radiated when the leaky wave travels to the far end of the antenna. Second, the antenna must scan across a wide angle span from 3.1GHz to 5.3GHz. The onset frequency of the leaky mode is set at 2.9GHz, to tolerate some manufacturing error and ensure there is a sufficient gain at 3.1GHz. The resulting dimensions of the half-width microstrip are 23mm in width and 1.5mm in height above the ground plane. The antenna is excited with a 10cm long semi-rigid RG-405 cable connecting to the outer edge of the antenna and Fig. 4.4 is a photo of the antenna prototype and a close-up view is shown as the inlet. Fig. 4.5 is the radiation pattern simulated using the MoM solver in FEKO [72]. The antenna is simulated with a thick top microstrip and an infinitely large ground plane. All surfaces are set to PEC. Fig. 4.4 shows the antenna gain plotted in color as a function of frequency and angle θ , which is defined with respect to the longitudinal direction of the antenna. As frequency is increased, the main beam steers from the broadside toward the endfire direction. The beamwidth of this 90cm long antenna is 15° at 3.1GHz and 6° at 5.3GHz. The backlobe in the $\theta > 90^\circ$ region is due to the leaky wave reflected from the far end of the antenna. It is much weaker than the main beam. Its effect on the P410 radar will be discussed later.

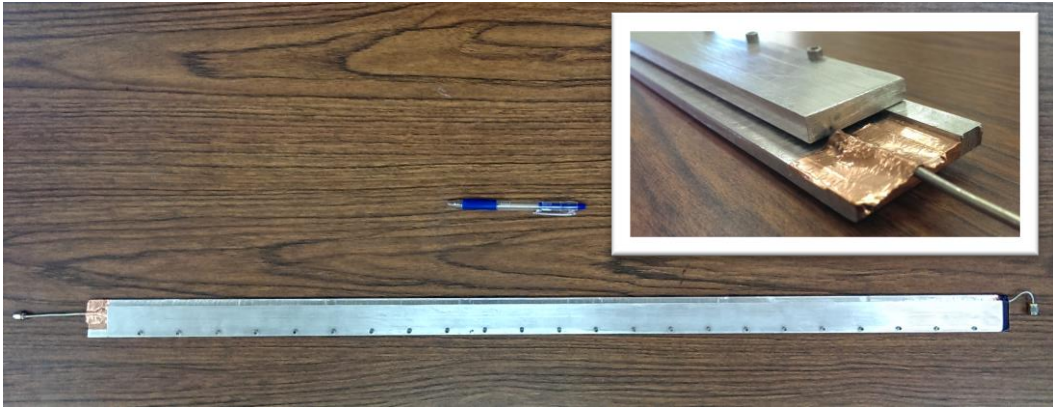


Fig. 4.4 The built antenna prototype. The pen is the dimension reference and a close-up view of the excitation is shown in the inset.

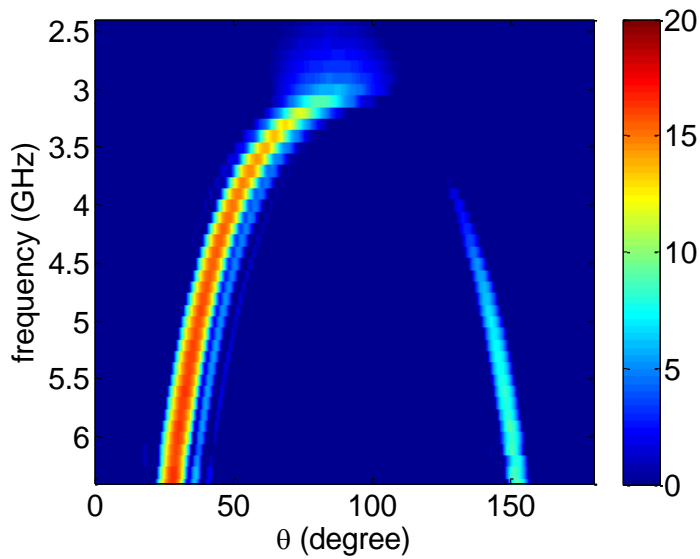


Fig. 4.5 Simulated gain pattern of the MLWA vs. frequency and angle.

The measured S_{11} of the built antenna with the far end left open is shown as Fig. 4.6(a). The S_{11} of the antenna is less than -10dB from 3.1GHz to 5.3GHz . However, the effect of the reflected wave from the far end can be observed in the S_{11} as the strong frequency beating. The beating is less prominent at low frequencies since the attenuation constant is larger, thus very small amount of the signal reaches the far end at low

frequencies. To study if the far end of the antenna will contribute to the early-time jamming or not, we inverse Fourier transform the collected data into the time domain and the result is plotted as Fig. 4.6(b). The first peak around 0ns includes the delay of the 10cm RG-405 cable as well as the mode conversion between the coaxial mode and the leaky mode. The second broad peak at 9ns is due to the reflection of the far end. The strength of the second pulse is attenuated by the two-way radiation loss. As the wave travels toward the far end, power is radiated in the forward beam. After it is reflected and travels in the opposite direction, power is radiated in the backward direction. There is also some radiation loss at the far end. In Fig. 4.6 (b), it is also noted that the pulse-width of the second one is broader than the one at 0ns. Moreover, 9ns corresponds to 135cm of distance in free space, which is longer than the 90cm long structure. These two phenomena arise due the fact that the leaky mode is dispersive. Thus, the group velocity of the wave is less than the speed of light. Different frequency components experience different delays thus the pulse is stretched.

While the reflection due to the far end is attenuated by almost 30dB, the long delay between the receiver and the far end is the problem. Assuming the mismatch of the LNA is -10dB, the reflection of the antenna input port is attenuated 22dB every 1ns, which is the delay of the 10cm RG-405 cable. It only takes 6ns to achieve an attenuation of 132dB. As for the far end of the antenna, the reflection is attenuated 40dB every 9ns and it will take 27ns to achieve an attenuation greater than 120dB. Thus, the reflection at the far end of the antenna must be reduced to mitigate the early-time jamming problem. A 3cm RG-405 cable is soldered at the far end of the antenna and connected with a matched load. The measured S11 of tis modified antenna is shown as Fig. 4.6(c), which shows much less frequency beating and the S11 is slightly improved across the band. The inverse Fourier transformed response is shown as Fig. 4.6 (d). The reflected strength at

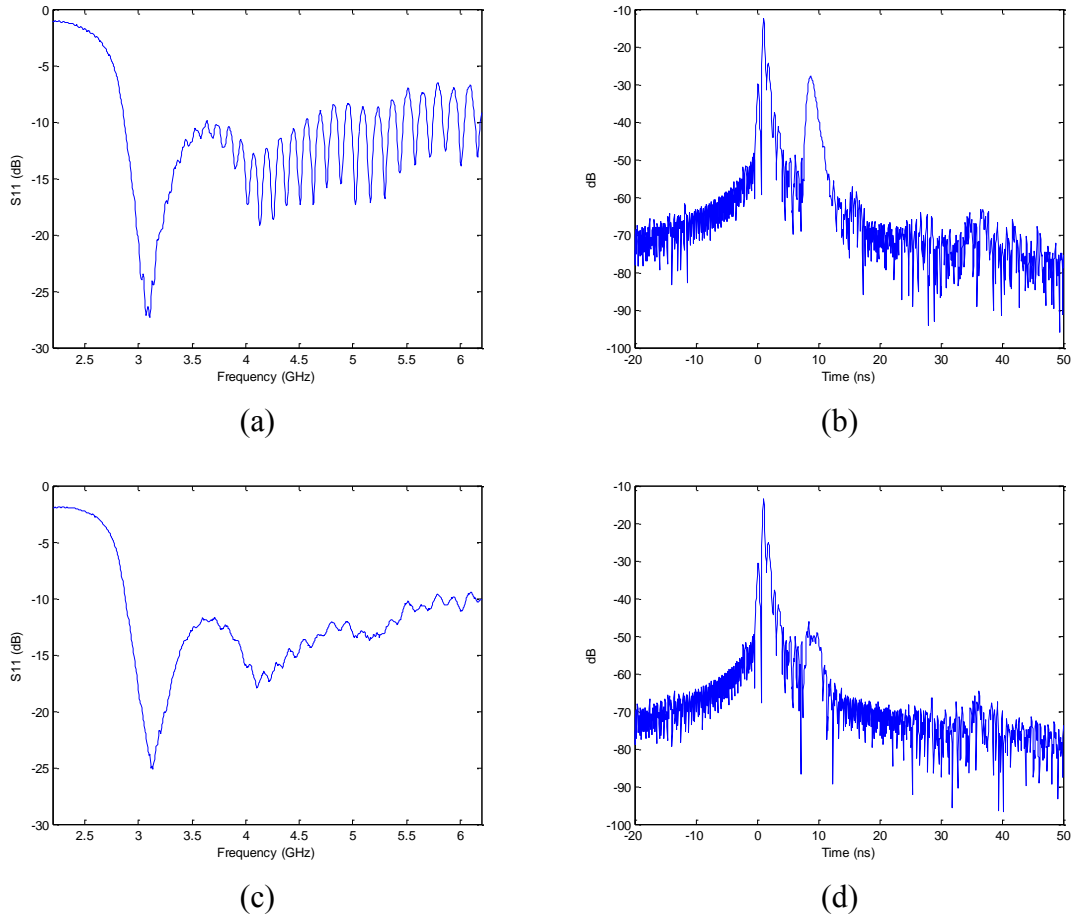


Fig. 4.6 (a) S11 of the built prototype with the far end left open. (b) The time response of the antenna with the far end left open. (c) S11 of the built antenna with a matched far end. (d) The time response of the antenna with a matched far end.

the far end is attenuated by 24dB comparing to Fig. 4.6(b). It only takes only 18ns to achieve an attenuation of 128dB. Overall, this approach significantly reduces the early-time jamming caused by the far end of the antenna.

4.4 SYSTEM INTEGRATION AND CHARACTERIZING THE P410

The concept of the combined radar-antenna system is shown in Fig. 4.7, where a short pulse is transmitted and received through the frequency-scanned antenna. In such a manner, the original short-pulse is decomposed into separate pulses with different carrier frequencies and each radiates into a different spatial direction. The received waveform is the sum of all these pulses modified by the targets at different directions. Considering each pulse has a different carrier frequency, the combined waveform requires processing to convert back into an azimuth scan. A circulator is inserted between the antenna and the radar so that the antenna is used for both transmitting and receiving. In such a configuration, the overall system beamwidth is better than one where the frequency-scanned antenna is only used on the transmitter or the receiver alone. Of course, the beamwidth performance of using a circulator can be achieved with two frequency-scanned antennas on both the transmitter and receiver. However, this would require the two antennas to have identical frequency-scanned beams, which could be quite challenging from the manufacturing point of view due to the length of the antennas. Using two antennas would lead to a better isolation between the transmitter and receiver. For the system using a circulator, the isolation between the transmitter and the receiver is dominated by either the return loss of the antenna or the isolation of the circulator. A poor isolation between the transmitter and receiver will result in self-jamming as discussed before, which is a major problem for a stepped-frequency system, where the steady-state amplitudes and phases are measured at different frequencies. However, this very early return can be gated-out in a time-domain system as long as there is no target within the range of the early-time jamming. A compact circulator also helps since the equivalent cable length is short and the pulses damp out in less time, thus the early-time jamming contaminates fewer range bins.

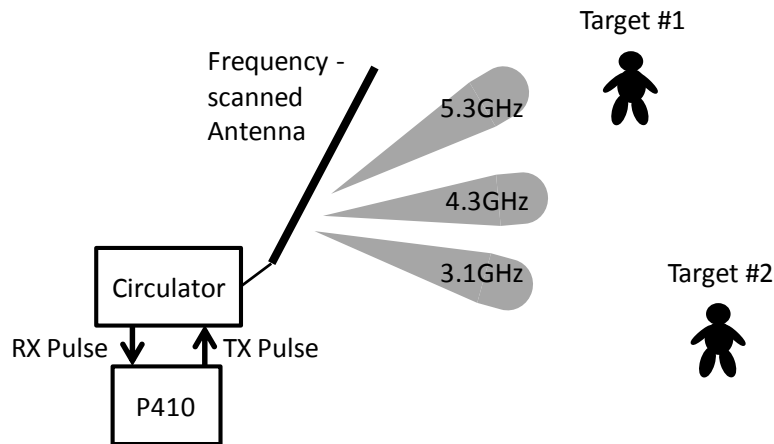


Fig. 4.7 Illustration of the system concept.

4.4.1 Circulator

The circulator adopted for the system is a CS-16-50 from MLCI Corporation. It has a bandwidth from 3GHz to 6GHz and can handle an average power of 50W. Port 1 and port 2 of the circulator were measured using a VNA while port 3 was connected to a matched load. The results are plotted as Fig. 4.8. The two ports show similar input mismatch, which is less than -20dB from 2.8GHz to 6.6GHz. The insertion loss is less than 0.6dB from 2.5GHz to 6.6GHz. The isolation is better than 8dB from 1GHz to 8GHz, or better than 15dB from 2.8GHz to 6.6GHz. It can be observed that the circulator does not have a sharp roll-off at low frequencies, which is a desirable feature for the system since the exact bandwidth of the P410 may extend below 3.1GHz. As stated before, the overall self-jamming is governed by either the isolation of the circulator or the mismatch of the antenna. Comparing Fig. 4.6 and Fig. 4.8, the isolation of the circulator is better than the antenna input mismatch. As a result, the self-jamming in the proposed system is mostly from the mismatch of the antenna across the band. The insertion loss (S_{21} in Fig. 4.8) and the isolation (S_{12} in Fig. 4.8) of the circulator from 2.8GHz to

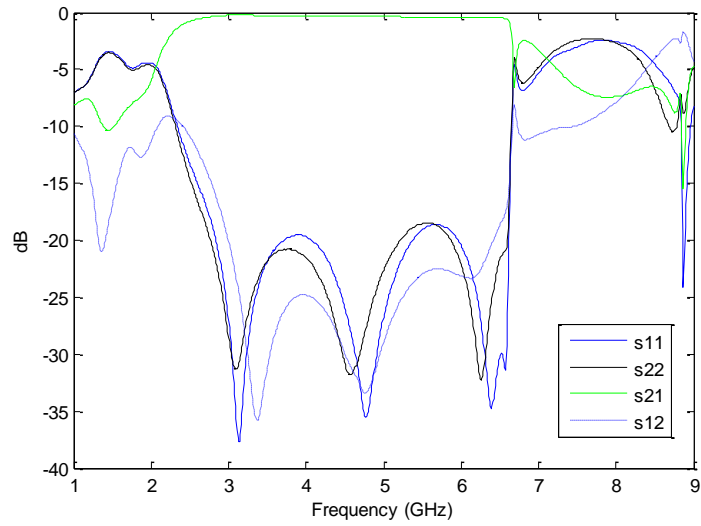


Fig. 4.8 The measured S-parameters of the CS-16-50 circulator.

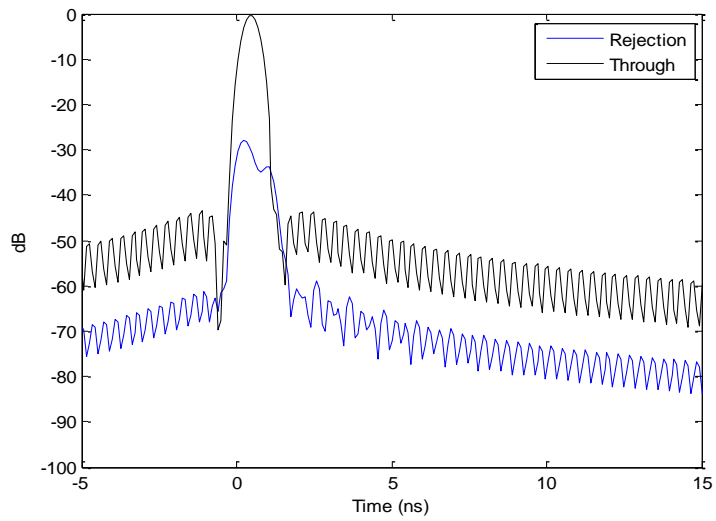


Fig. 4.9 The pulse shapes of the Fourier transformed insertion loss and isolation. They are labelled as through and rejection, respectively.

5.6GHz are inverse Fourier transformed into the range domain with a Hamming window and plotted as Fig. 4.9. They are labeled as through and rejection, respectively. The nice pulse shape of the through response indicates that the circulator achieves nearly linear phase shift across the frequencies. Thus, it will not deteriorate the transmitted pulse shape from the P410. The rejection response has a magnitude of -29dB in the time domain. This indicates when the circulator is connected to P410, the coupling between the transmitter and receiver through the circulator is very weak.

4.4.2 Equivalent frequency response of the P410

In order to generate the azimuth response of a scene, the frequency response of the system must be dominated by the frequency-scanned antenna but not the other components. It has been shown that the frequency response of the circulator is flat across the band of operation. In this section, we set out to characterize the equivalent frequency response of the P410 radar. Instead of measuring the transmitter and receiver frequency response separately using a fast oscilloscope and a high speed signal generator, the P410 unit is considered as a single unit and the equivalent frequency response is calibrated using a scattering measurement with time-gating. In this setup, the reflections due to mismatches of components are confined in the early time while the main late time reflection is due to the target, which can be separately characterized by VNA measurements for comparison and equalization.

Two broadband horns and a 13” calibration sphere are setup and an S21 measurement is made using the VNA first. Background subtraction is applied to remove the coupling between the antennas, the indoor clutters, and the supporting base of the sphere. The collected frequency response is inverse Fourier transformed into the time domain and plotted as Fig. 4.10(a). The target is located at 18ns and the pulse shape

includes the dispersion of the horn, path loss, as well as target-related response. The target response around 18ns is gated and Fourier transformed back to the frequency domain as shown in Fig. 4.10(b). The strength gets weaker as the frequency is increased, corresponding to the frequency-dependent path loss. Next, the same setup is measured using a high- power P410 unit set to -14.5dBm. Background subtraction is applied as well. The time response is plotted as Fig. 4.10(c). The response is then time-gated about the target response at 30ns and Fourier transformed into the frequency domain as shown

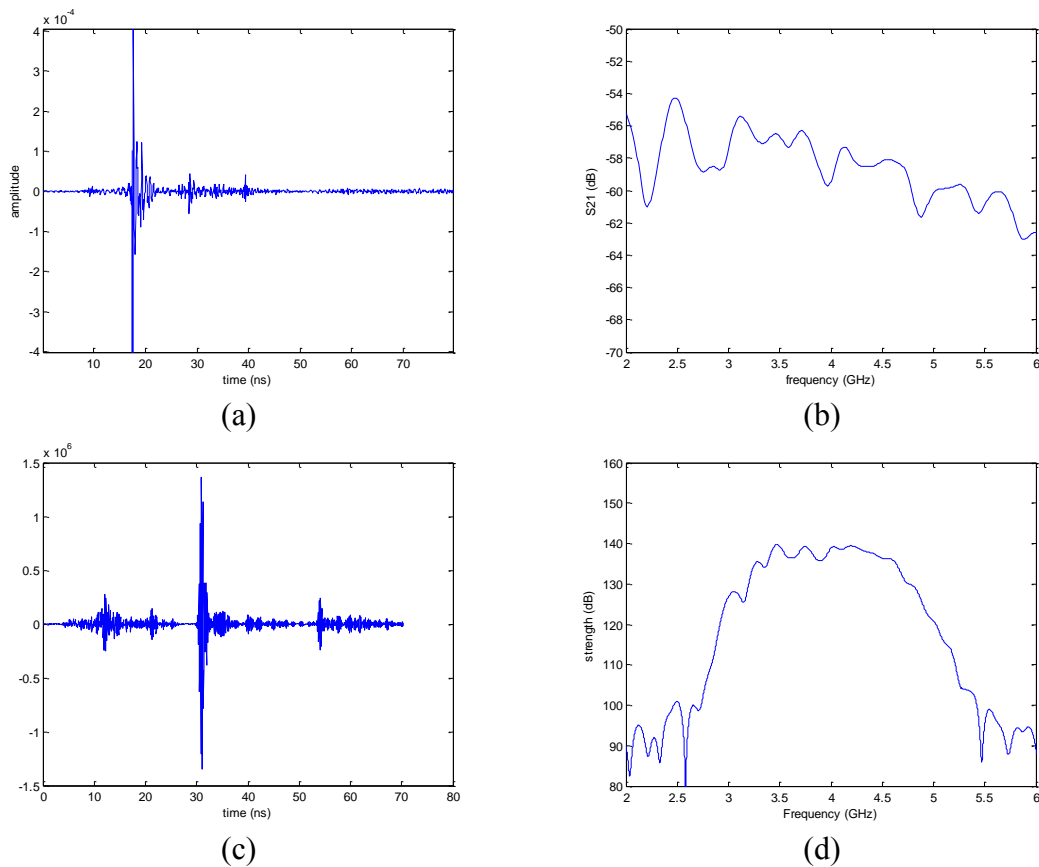


Fig. 4.10 The scattering calibration. (a) VNA measured equivalent time response. (b) VNA measured, time-gated equivalent frequency response. (c) P410 measured target response. (d) P410 measured, time-gated equivalent frequency response.

in Fig. 4.10(d) for comparison. The residual of the background subtraction in the early time is clearly seen in Fig. 4.10(c). It is also noted that the time delays for the target in Fig. 4.10 (a) and Fig. 4.10(c) are different, indicating there are extra delay inside the P410. As for the equivalent frequency response in Fig. 4.10(d), it does show a finite bandwidth with a plateau from 3.3GHz to 4.6GHz. It is also noted that the roll-off is different at low frequencies and high frequencies. Lastly, the complex frequency response in Fig. 4.10(d) is divided by the one in Fig. 4.10(b) to yield the equivalent frequency response of the P410, assuming the frequency response of the VNA is perfectly flat. The antennas, path-loss, and target response are removed in this manner. The result is shown as Fig. 4.11. The amplitudes at 3.1GHz and 5.3GHz are -15dB and -34dB below the peak, respectively. The phase is within 45° from 3.4GHz to 5.3GHz. It is noted that the low frequency end has higher power but experiences more phase shift.

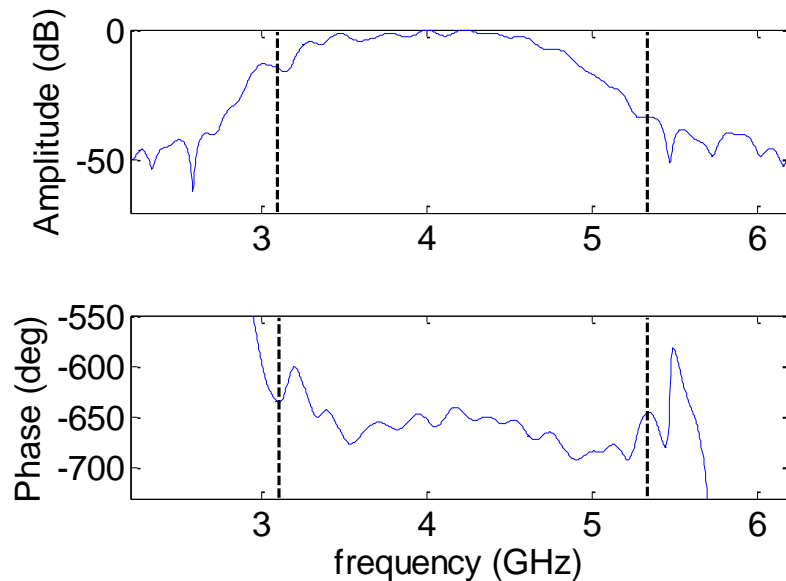


Fig. 4.11 The complex equivalent frequency response of the P410 transceiver.

4.4.3 Validation with full-wave solver

To verify that the system will produce frequency peaks corresponding to the directions of the targets, a trihedral is placed at various directions and collected using a P410 with background subtraction. The results are plotted as Fig. 4.12(a) - Fig. 4.12(c). The targets are placed about 80° , 60° , and 40° with respect to the longitudinal direction of the antenna. The distance is about three meters. It can be seen that the target at 80° returns very weak power and does not show a strong frequency peak. This is due to two factors. First, the carrier frequency with a main beam direction at 80° is 2.9GHz, where the P410 transmits very little power as shown in Fig. 4.11. Second, the gain at this direction is very low comparing to other directions, since this is the onset frequency of the mode. The other two target directions both show prominent peaks at different frequencies, indicating that the target is resolved by the frequency-scanned beam. For comparison, a 16cm dihedral is simulated using the MoM solver in FEKO. A simulated S11 without the dihedral is subtracted from S11 with the dihedral to remove the reflection due to the antenna. The remaining frequency response is multiplied by the equivalent frequency response in Fig. 4.11. The results with the dihedral placed at different directions are plotted as Fig. 4.12(d) - Fig. 4.12(f) and they all show different frequency peaks. The agreement between the Fig. 4.12(a) - Fig. 4.12(c) and Fig. 4.12(d) - Fig. 4.12(f) is reasonable. Lastly, the measured response outside the 3.1GHz to 5.3GHz is substantially higher comparing to the simulated counterpart. This could be due to noise and intermodulation from the non-linearity of the transceiver.

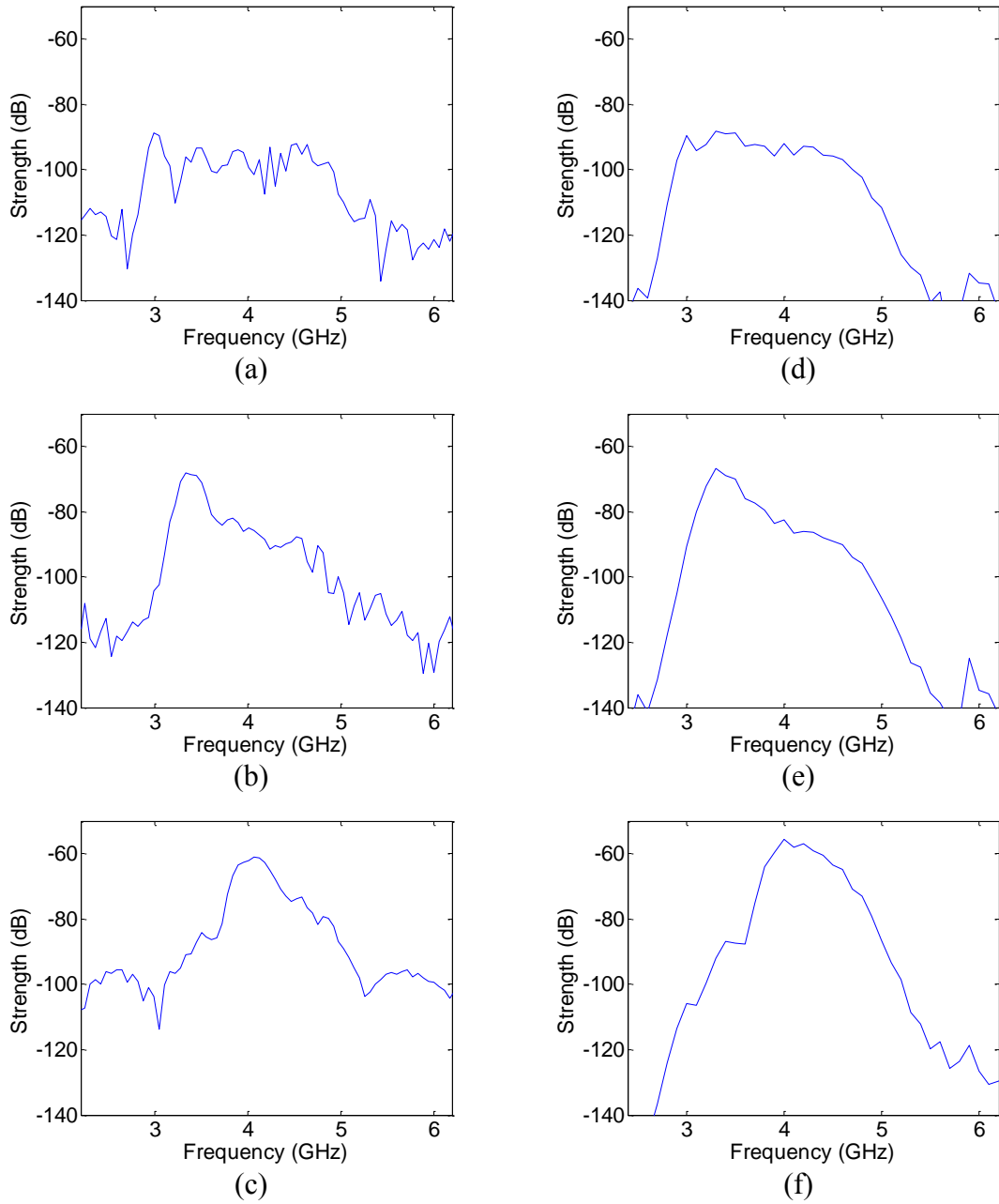


Fig. 4.12 (a) - (c) Measured frequency response of targets at about 80°, 60°, and 40°. (d) - (f) Combined response of full-wave simulations and the equivalent frequency response of the P410.

4.5 LINE-OF-SIGHT AND THROUGH-WALL TRACKING OF HUMAN

The direction-finding capability of the system has been demonstrated in the previous section and it shows that the low-end cutoff of P410 limits the scanning range near the broadside direction. In this section, two measurements were collected and processed to show the capability of the combined system. It is noted that the STFT can directly applied to the collected time domain data without the need to Fourier transform the collected frequency data into the time domain as in the previous chapter. Line-of-sight and through-wall measurements of a human subject walking were collected first. An average frame is computed from the whole sequence as the background and it is subtracted from all the frames to remove static clutter as well as the early-time jamming. Afterwards, the data are processed using the STFT with a 6ns Hamming window. Snapshots of the line-of-sight measurement are shown as Fig. 4.13(a) - Fig. 4.13(f). The time interval between snapshots is about 1.5sec. During this measurement, the subject walked from the endfire toward the broadside direction of the antenna while maintaining the same distance to the radar. The sequence of snapshots clearly shows the subject walking from the endfire direction (high frequency) toward the broadside direction (low frequency). It is also noted that the target response is different in each snapshot. This may be due to the frequency response of the antenna and the posture of the subject at different frames.

Next, the antenna was put right next to a 23cm-thick exterior wall to test the through-wall performance as shown in Fig. 4.14. The antenna and radar were on an 89cm tall wood bench. Instead of using a constant background subtraction, a two-second moving average is used to generate the background for each frame. This moving average background is subtracted from each frame to remove the return due to static clutter, especially the wall. The snapshots of a human subject walking are shown in Fig. 4.15(a) -

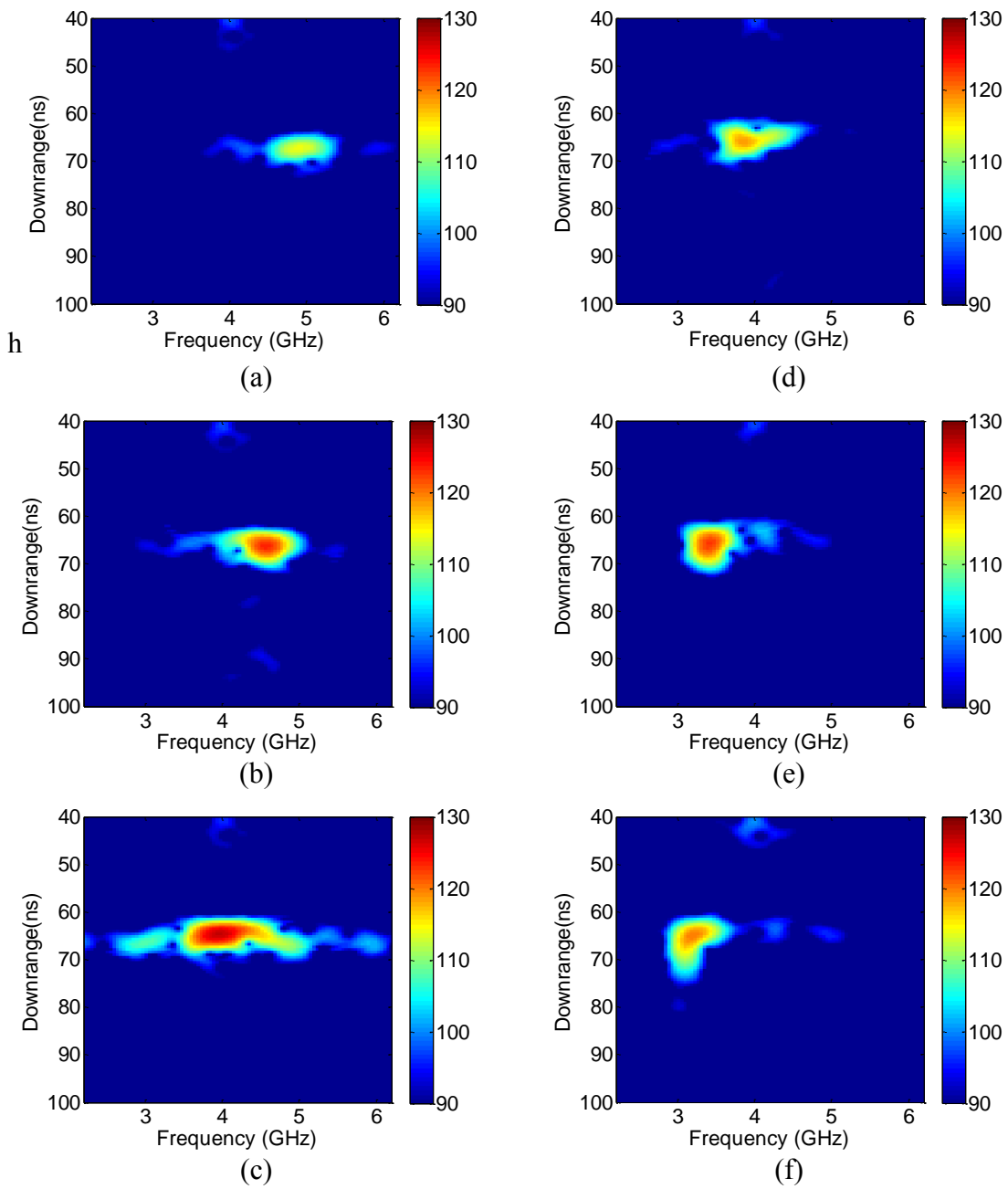


Fig. 4.13 Snapshots of the line-of-sight measurement of a walking human subject.

Fig. 4.15(f). The first three snapshots are the subject walking near the broadside direction of the antenna and toward the radar. The last three snapshots are the subject walking along the endfire direction of the antenna. The signal to noise ratio is not as good as the line-of-sight measurement since the wall not only attenuates the transmitted power but also introduces a strong reflection, which can be considered as a strong early-time reflection that masks the other targets and may even saturate the receiver. Overall, the human subject still can be tracked in the through-wall environment. However, the target response is less focused compared to Fig. 4.13. Moreover, the signal strength near the endfire direction is much weaker than those near the broadside direction due to two factors. First, the wall attenuates high frequency components more than low frequency components. Second, the transmitted power is much weaker at higher frequencies as shown in Fig. 4.11. An ADC with a higher dynamic range and a high power PA together may improve the through-wall performance. Lastly, the wall may cause refraction that distorts the DOA information.

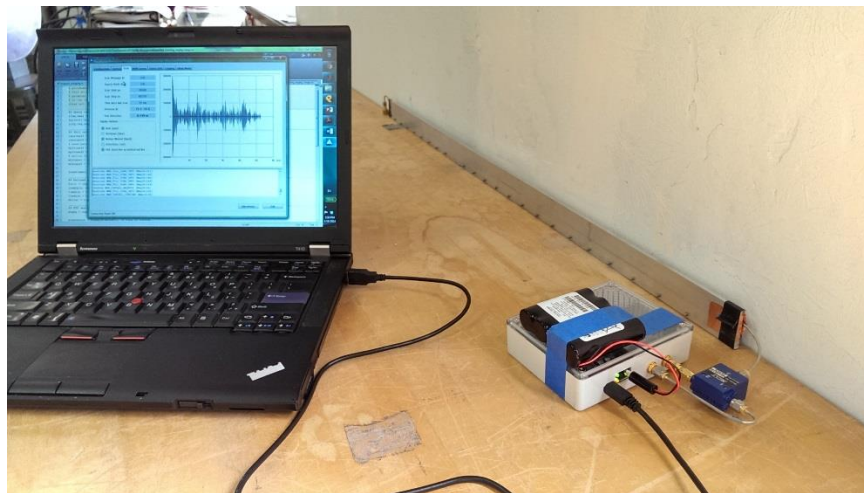


Fig. 4.14 The setup of the through-wall measurement. The antenna is put right against the wall.

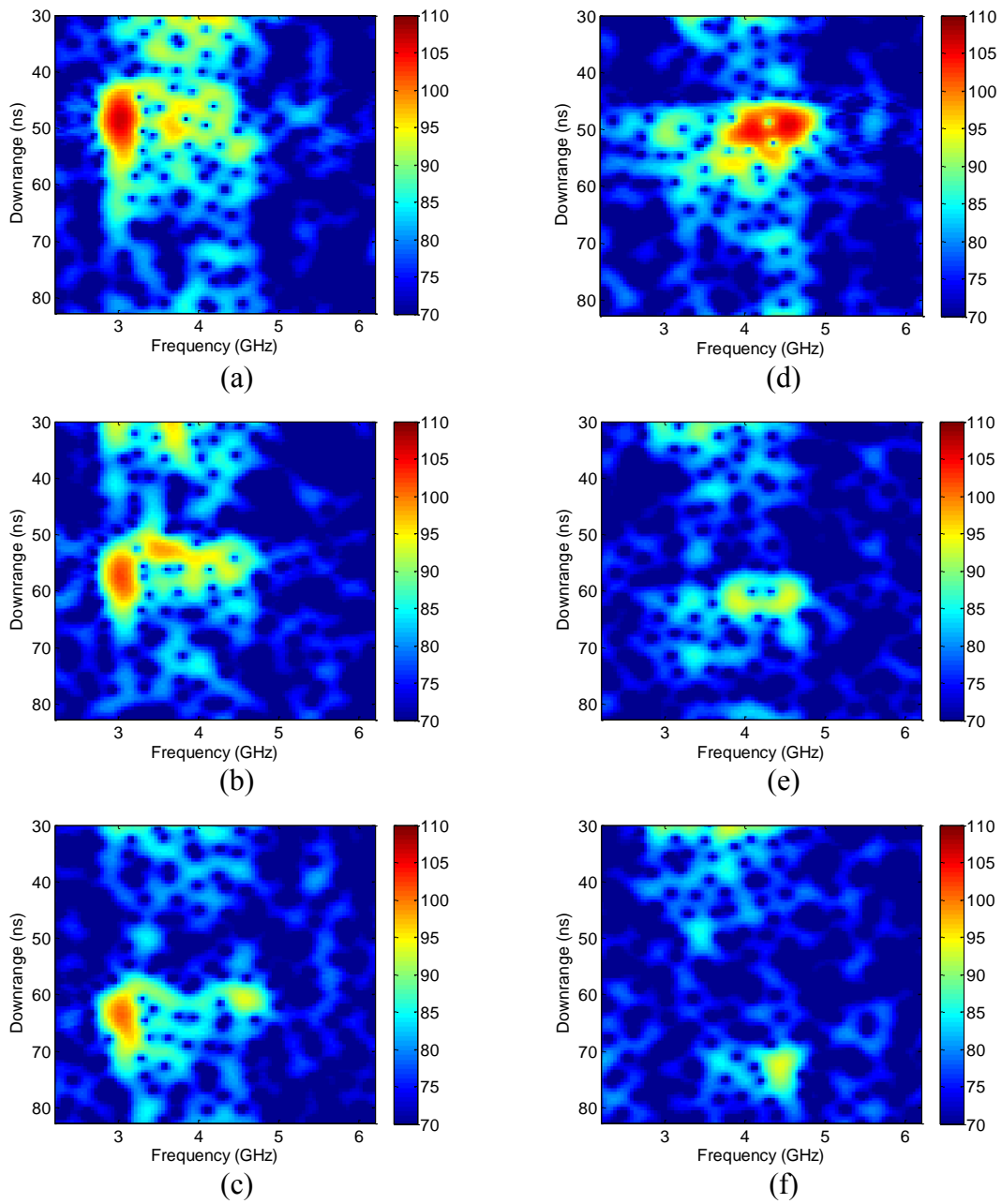


Fig. 4.15 Snapshots of the through-wall measurement of a walking human subject.

4.6 CONCLUSION

In this chapter, a frequency-scanned antenna was combined with a short-pulse radar to achieve 2-D range-azimuth imaging of a scene. The early-time jamming of the short-pulse radar was studied in detail. A long antenna was designed and built to achieve a better azimuth resolution than the short microstrip LWA used in Chapter 3, and to match the frequency bandwidth of the radar. The far end of the antenna was effectively matched to reduce the early-time jamming. Next, the system concept was discussed and a circulator was inserted between the antenna and the radar to effectively use the antenna for both transmit and receive and therefore achieve a narrower azimuth resolution. The frequency responses of the circulator and the short-pulse radar were characterized in detail through a set of measurements. Next, the direction-finding capability of the combined system was verified with static target measurements and full-wave simulations. Both line-of-sight and through-wall images of a human subject were presented. These results demonstrate the performance of this simple and compact system, which can be readily tailored for law enforcement or perimeter security applications.

The detailed study of the relationship between the short-pulse radar and the frequency-scanned antenna also leads to other observations that may improve the overall performance by changing the design of the transceiver. First, early-time jamming can be reduced with less internal coupling and better matched LNA and PA. Second, a smoother window function, instead of a nearly square window, in the rake receiver can be implemented for a better sidelobe performance in the frequency domain. Lastly, a higher transmitted power, especially at higher frequencies, and a receiver with a better dynamic range can improve the through-wall performance.

Chapter 5: Two-section Microstrip Leaky Wave Antenna

5.1 INTRODUCTION

The half-width microstrip LWA was used in the previous two chapters to demonstrate the imaging capability of a frequency-scanned antenna with both a stepped-frequency radar and a short-pulse radar. Furthermore, a long antenna was designed in the previous chapter to match the frequency bandwidth of the short-pulse radar as well as to improve the direction-finding capability. Usually, the beamwidth of an antenna can be reduced by increasing its electrical size. However, this is not always the case for an LWA since the attenuation constant also affects the effective antenna length. As a rule of thumb, the length of an LWA is usually chosen for the antenna to radiate 90% of the accepted power at the frequency with the smallest attenuation constant within the operating bandwidth. Therefore, both a small attenuation constant *and* a long aperture are needed for an LWA to achieve a narrow beam. In this work, a two-section microstrip LWA is proposed to achieve a small attenuation constant and a narrow beam.

This chapter is organized as follows. The proposed antenna geometry and the associated TRM analysis are presented in Sec. 5.2. The effects of the geometrical parameters on the propagation and attenuation constants are examined. In Sec. 5.3, a microstrip LWA is designed based on the TRM analysis. A short prototype is then built and measured. The antenna gain patterns and the extracted propagation and attenuation constants are further compared to TRM results to verify that the proposed structure indeed achieves a small attenuation constant. In Sec. 5.4, a longer version of the proposed LWA is simulated using the full-wave solver FEKO. Its narrow-beam performance is demonstrated in comparison to a conventional half-width microstrip LWA. Some implications of the proposed antenna for radar applications are discussed in Sec. 5.5, and Sec. 5.6 is the conclusion.

5.2 ANTENNA GEOMETRY AND TRM ANALYSIS

The cross-section views of a conventional half-width microstrip LWA and the proposed two-section design are illustrated in Fig. 5.1(a) and Fig. 5.1(b), respectively. The longitudinal direction is chosen to be the z-axis and the transverse direction is along the y-direction. A half-width microstrip LWA consists of a top microstrip, a large ground plane, a dielectric substrate, and a side shorting plane. The dielectric substrate is shown in green in Fig. 5.1(a). Note that even though this dissertation focuses on the air-filled design due to the broader antenna bandwidth, the derivation here will be kept more general by considering a dielectric substrate. The width of the half-width microstrip is W and the thickness of the dielectric substrate is h . Microstrip LWA is usually fabricated using PCB technology and the shorting plane can be implemented using vias. It is noted that the attenuation constant of the dominant leaky mode in this structure is strongly dependent on the thickness of the substrate, as it controls the radiation leakage from the structure. Although a very thin half-width microstrip LWA would have a small attenuation constant, it would also affect the characteristic impedance of the leaky mode and complicate the input impedance matching to the antenna. In order to reduce the radiation leakage while retaining most of the original field distribution, it is proposed to add another thinner section of microstrip to a conventional half-width microstrip LWA. The proposed two-section microstrip LWA is illustrated in Fig. 5.1(b). The total width of the top microstrip becomes $(W_1 + W_2)$ and the thicknesses of the dielectric substrate in the individual section are h_1 and h_2 , respectively.

Next TRM is applied to solve for the complex propagation constant of the proposed two-section design. The transverse equivalent circuit is shown in Fig. 5.2. It includes two transmission lines with different characteristic impedances, two load impedances on the two ends, and a lump capacitor to model the stored energy due to the

step. Since the heights are much smaller than the widths in the individual sections, transverse electromagnetic (TEM) modes are assumed. As a result, the impedance in the individual section is proportional to the height h_i and the transverse wave numbers in the two sections are the same. The impedance of the thicker section as unity and the impedance of the thinner section as h_2/h_1 , without loss of generality. The complex propagation constant of the proposed two-section microstrip LWA can be computed by solving the following transverse resonance condition:

$$Y^+ + Y^- + jB = 0 \quad (5.1)$$

where Y^+ and Y^- are the admittances looking into the thicker and thinner sections, respectively, and B is the capacitive susceptance per unit length of the step discontinuity. The individual quantities are discussed separately. First, the admittance Y^+ is the reciprocal of the familiar impedance expression of a shorted transmission line with a transverse wave number k_y and length W_1 :

$$\frac{1}{Y^+} = j \tan(k_y W_1) \quad (5.2)$$

For B , the capacitive susceptance per unit length of an E-plane step discontinuity between two parallel plate waveguides is used, where the characteristic impedances of the two transmission lines are unity and h_2/h_1 respectively. This was derived in [81] using conformal mapping, with the result:

$$B = \frac{\sqrt{\epsilon_r} k_0 h_1}{\pi} \left[2 \ln \frac{h_1^2 - h_2^2}{4h_1 h_2} + \left(\frac{h_1}{h_2} + \frac{h_2}{h_1} \right) \ln \left(\frac{h_1 + h_2}{h_1 - h_2} \right) \right] \quad (5.3)$$

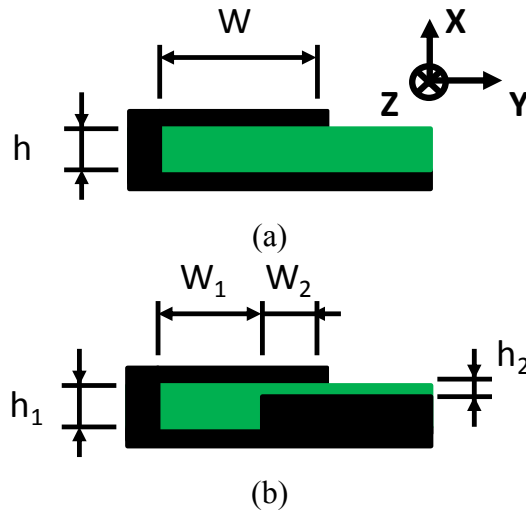


Fig. 5.1 (a) The geometry of a conventional half-width microstrip LWA. It consists of a top microstrip, a ground plane, and a side shorting plane. (b) The proposed two-section microstrip LWA. It consists of two microstrip LWA sections with different thicknesses of dielectric material. The top microstrip is kept at the same height.

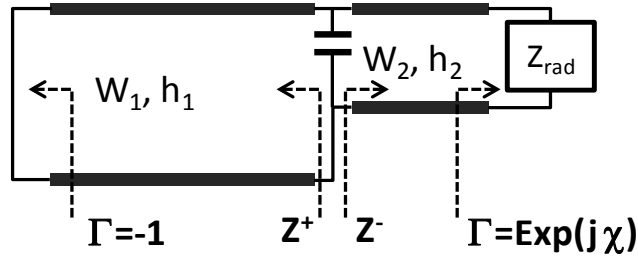


Fig. 5.2 The transverse equivalent circuit model of the proposed two-section microstrip LWA. The left most edge represents the shorting plane and the right most impedance represents the radiation impedance from a parallel plate waveguide connecting to an extended dielectric slab. The capacitor in the middle models the step discontinuity.

where k_0 is the free space wave number and ε_r is the dielectric constant. It is found through the subsequent validation with measurements, that the inclusion of this susceptance is crucial to correctly model the propagation constant. To obtain Y^- , the following equation is derived by Chang and Kuester [54] for the reflection coefficient, $\Gamma = \exp(j\chi)$, of a thin parallel plate waveguide connected to an infinitely extended dielectric substrate. The detail of χ was summarized in Chapter 2. Therefore, Y^- can be expressed as the transformed impedance of the complex radiating impedance due to a section of transmission line:

$$\frac{1}{Y^-} = -j \frac{h_2}{h_1} \cot\left(k_y W_2 - \frac{\chi}{2}\right) \quad (5.4)$$

Combining (5.2), (5.3), and (5.4) into (5.1), the final transcendental equation is expressed as:

$$\cot(k_y W_1) = \frac{h_1}{h_2} \tan\left(k_y W_2 - \frac{\chi}{2}\right) + B \quad (5.5)$$

To compute the complex wave number of the lowest order leaky mode, it is assumed that both the cotangent and tangent functions in (5.5) are within the first branch cut and (5.5) is solved for k_y at each frequency. Higher order modes can be solved in a similar fashion with the proper choice of branch cuts. Lastly, the longitudinal wave number k_z , which governs the radiation properties of the leaky wave antenna, can be computed using (2.9) in Chapter 2 after k_y is found.

In order to show the relationship between the geometry and the resulting mode properties, complex propagation constants of different air-filled two-section designs are

computed and plotted. The air-filled design was chosen in Chapter 3 because of the inherent broad bandwidth for ranging. This will be assumed throughout the remainder of the chapter. Fig. 5.3 shows the propagation constant, β , and attenuation constant, α , for various values of h_2 , while h_1 is fixed at 2mm. W_1 and W_2 are 15mm and 0.5mm, respectively. As h_2 is reduced from 2mm to 0.1mm, the propagation constant becomes larger while the attenuation constant becomes smaller for frequencies higher than the cutoff frequency, which is the point at which the attenuation and propagation constants are equal. The change in the propagation constant is similar to the effect of a capacitive loading on the open edge [66]. In fact, the narrow second section can be considered as a parallel plate capacitor. As h_2 becomes smaller, the increased capacitance leads to an increase in the propagation constant. Moreover, a larger difference between h_1 and h_2 increases the local stored electric energy in the step. This effect also contributes to an increased propagation constant. In Fig. 5.4, W_2 is changed to show its effect on the complex propagation constant while W_1 , h_1 , and h_2 are fixed at 14.3mm, 2mm, and 0.3mm, respectively. The propagation constant increases and the attenuation constant decreases at a fixed frequency as W_2 becomes wider. The change of the propagation constant can be explained by the increase in capacitance, similar to the argument for the change in h_2 .

To better illustrate the effects of the geometry on the attenuation constant, which is one of the key factors to achieve a narrow-beam microstrip LWA, the propagation and attenuation constants versus frequency plot of a given structure is converted into a (attenuation constant)-(beam direction) plot using the frequency scanning property. The main beam direction θ , which is defined with respect to the z-axis, is computed using the $\cos\theta = \beta/k_0$ formula. As a result, each pair of α and β versus frequency curves in Fig. 5.3 and Fig. 5.4 is converted into a single α vs. θ curve in Fig. 5.5(a) and Fig. 5.5(b).

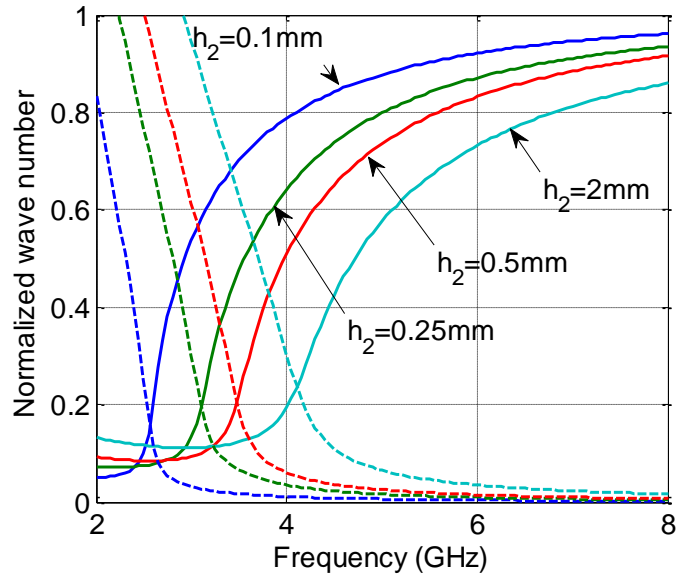


Fig. 5.3 Complex normalized propagation constants for different heights in the second section. Solid lines are propagation constants and dashed lines are attenuation constants.

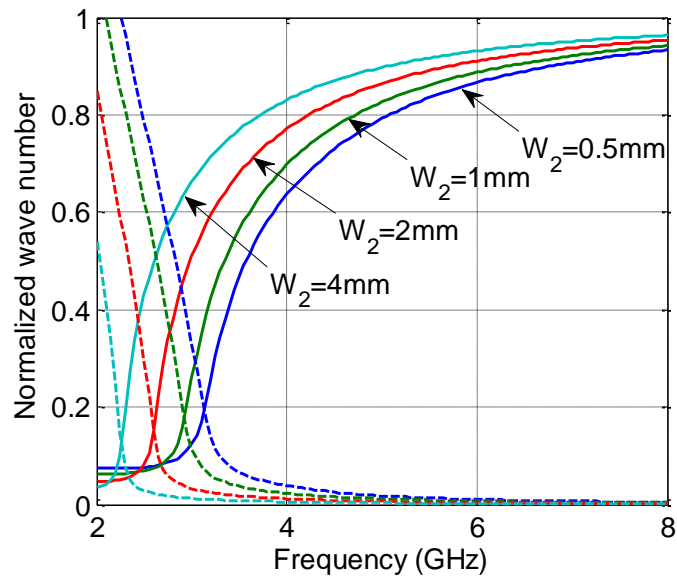


Fig. 5.4 Complex normalized propagation constants for different widths in the second section. Solid lines are the propagation constants and dashed lines are attenuation constants.

These figures show the absolute (not normalized) attenuation constant versus beam direction for different geometries. If all structures are infinitely long, the antenna with the smaller absolute attenuation constant will have a narrower beamwidth. From Fig. 5.5(a) and Fig. 5.5(b), it is apparent that to design a narrow-beam two-section microstrip LWA, a thin and wide second section is needed. Moreover, it can be observed that the beamwidth is always the narrowest near the end-fire direction (small θ). However, by designing for a small attenuation constant, the beamwidth variation across scan angles is reduced.

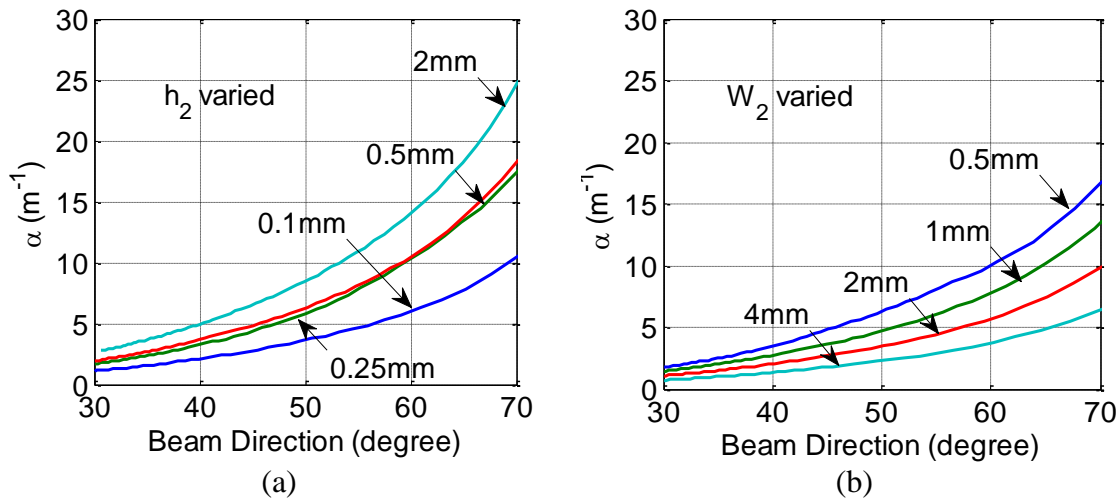


Fig. 5.5 (a) Attenuation constants at different beam directions of the geometries discussed in Fig. 5.3. (b) Attenuation constants at different beam directions of the geometries discussed in Fig. 5.4.

5.3 PROTOTYPE AND MEASUREMENT

To verify the TRM analysis, two-section microstrip LWA was designed and built. Its performance is then compared to the conventional half-width microstrip LWA implemented earlier in Chapter 3. The prototype of the proposed two-section design is shown in Fig. 5.6. It consists of two aluminum blocks. The green region in Fig. 5.1(b) was first removed from the bottom block using a milling machine and the top block works as the top microstrip with an increased thickness for better mechanical stability. In the structure, $W_1=11.6\text{mm}$, $W_2=4.42\text{mm}$, $h_1=1.8\text{mm}$, and $h_2=0.343\text{mm}$. The length was chosen to be 26cm, the same as the half-width microstrip LWA prototype in Chapter 3 for a direct comparison. To excite the leaky modes, 0.085 in. semi-rigid 50Ω coaxial cables were used as the feeds for both antennas. The center conductor of the coaxial cable was soldered to the edge of the top microstrip in the conventional half-width prototype and to the top microstrip in the proposed two-section design at where the step is. The outer connectors were both soldered to the ground planes. The measured radiation patterns of the proposed two-section design and the conventional half-width design are plotted respectively in Fig. 5.7 and Fig. 5.8. The horizontal axis is the angle θ measured with respect to the z-axis and the vertical axis is the frequency. The measured antenna gains are color coded with a dynamic range from -2dBi to 13dBi. In this format, the frequency-scanned beam is well illustrated. Comparing Fig. 5.7 and Fig. 5.8, the beam steers more quickly as frequency is varied in the proposed two-section design than in the conventional half-width design. More significantly, a much stronger back lobe (in the $\theta > 90^\circ$ sector) is observed in the proposed two-section design. This is a clear indication of a smaller attenuation constant of the leaky mode in the new structure. When combined with the short length of the antenna, this leads to a backward traveling wave reflected from the far end of the antenna and a strong back lobe. The peak gain is also observed to

fluctuate as a function of frequency. This is due to the interference between the radiated fields from multiply reflected leaky waves between the two ends of the proposed two-section structure.

Since the antenna pattern shows a prominent back lobe, it may be possible to relate its strength to the attenuation constant. This could provide a useful way to obtain the attenuation constant of the guiding structure from the measured antenna pattern. Here a simple retrieval procedure is carried out to approximately determine the attenuation constant from the radiation pattern. It is assumed that the radiation of the antenna is from the equivalent magnetic current on the outer edge of the structure, which carries the complex propagation constant of the leaky mode. Next, only one forward propagating wave and one backward propagating wave are assumed on the structure. They give rise to the beams in the forward and backward directions, respectively. The two waves have the same field distribution, except they travel and decay in opposite directions. Therefore, their resulting radiation patterns are symmetrical about $\theta=90^\circ$ while the field strengths are proportional to the strengths of individual magnetic currents.



Fig. 5.6 The prototype of the proposed two-section microstrip LWA consists of two aluminum blocks. The air-filled region is removed from the bottom ground plane using a milling machine and the top aluminum block works as the top microstrip.

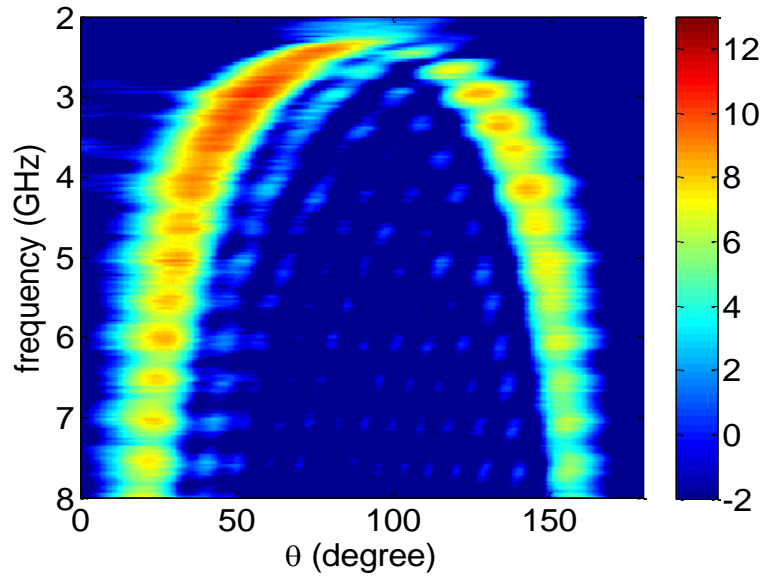


Fig. 5.7 Measured radiation pattern of the proposed two-section microstrip LWA prototype.

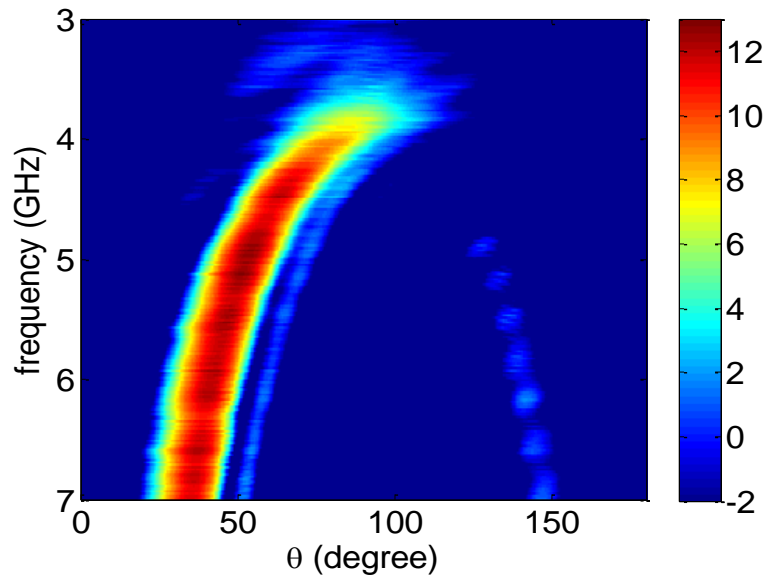


Fig. 5.8 Measured radiation pattern of the conventional half-width microstrip LWA prototype.

It is further assumed that the field in the backlobe direction due to the forward propagating wave is much weaker than the field in the same direction due to the backward propagating wave. As a result, the gain ratio of the forward and backward lobes can be approximated by the square of the ratio between the amplitudes of the forward and backward propagating equivalent magnetic currents. The result is simply $\exp(-2\alpha L)$, where L is the physical length of the antenna. The normalized attenuation constant can thus be expressed as:

$$\frac{\alpha}{k_0} = \frac{G_{fwd}(dB) - G_{bwd}(dB)}{k_0 \cdot 20L \cdot \log_{10}(e)} \quad (5.6)$$

where G_{fwd} and G_{bwd} are the gains in the forward and backward directions in dB scale. This formula is only an approximate one since the actual structure could support multiply reflected waves. In addition, it is assumed that 100% of the power is reflected from the far end of the antenna.

Fig. 5.7 and Fig. 5.8 are processed using (5.6) to show the retrieved attenuation constants. Results of the proposed two-section microstrip LWA are shown in Fig. 5.9 and results of the conventional half-width microstrip LWA are shown in Fig. 5.10. The propagation constant is also plotted in these figures by using the standard cosine formula (2.1) given in Chapter 2. The measurement-extracted results are plotted as solid curves and the TRM results are plotted as dash curves for comparison. The blue curves are the attenuation constants and the green curves are the propagation constants. The range of the normalized attenuation constant is only from 0 to 0.1 in order to better illustrate the very small attenuation constants while the range of the normalized propagation constant is still from zero to one. The propagation constant curves derived from the measured beam

directions agree well with those from TRM. Although the retrieved attenuation constant curves contain some undulations due to the higher-order multiple reflections present in the actual structure, they show fairly good agreement with the TRM results. It is also noted that the retrieved attenuation constant in Fig. 5.10 is not accurate below 5GHz, since (14) is not accurate when the backlobe is not prominent. Overall, the results show that the complex propagation constant of the new structure based on TRM agrees reasonably well with the measurement results. More importantly, the designed two-section microstrip LWA has a small α and can achieve narrow-beam performance when the aperture is made sufficiently long.

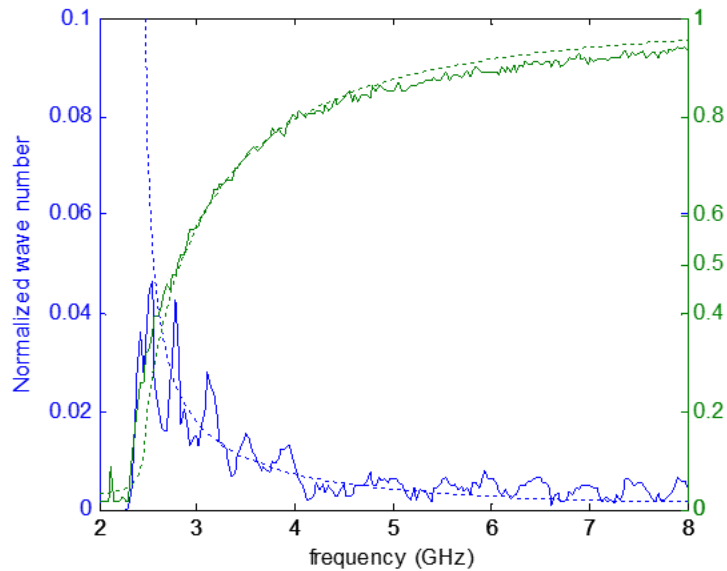


Fig. 5.9 Retrieved propagation and attenuation constants from the radiation pattern of the proposed two-section microstrip LWA. Dashed curves are the attenuation and propagation constants computed using TRM.

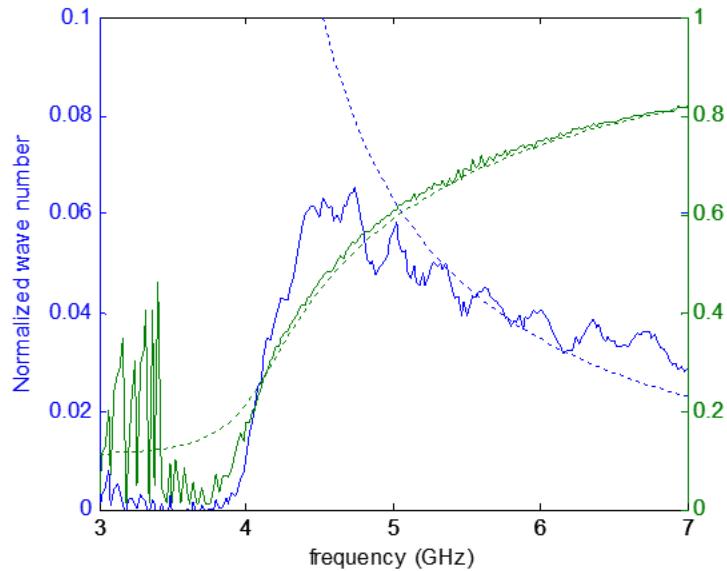


Fig. 5.10 Retrieved propagation and attenuation constants from the radiation pattern of the conventional half-width microstrip LWA. Dashed curves are the attenuation and propagation constants computed using TRM.

5.4 NARROW BEAM ANTENNA DESIGN

The antenna design from the previous section is next extended to a long aperture to demonstrate its narrow-beam performance. Based on the 90% radiated power criterion at 4.5GHz, the length of the antenna is chosen to be 200cm long. The antenna is operated between 2.5GHz and 4.5GHz since this is the frequency range where the beam steers the most. The structure is simulated using the MoM solver in FEKO. The finite ground plane and the thick top microstrip shown in Fig. 5.6 are both modeled. The width and maximum thickness of the ground plane are 49.94mm and 5.68mm, respectively. For the top microstrip, the dimensions are 32mm and 6.18mm. The 0.085 in. semi-rigid 50Ω coaxial cable is also modeled in the simulation with a cable length of 3cm. All surfaces are simulated as PEC.

The simulated radiation patterns of the proposed two-section design are plotted in a polar format in Fig. 5.11. The angle is defined with respect to the longitudinal direction (so zero degree is the endfire direction), and the dynamic range is from -10dBi to 20dBi. The simulated patterns at 2.9GHz, 3.4GHz and 3.9GHz are plotted as the blue curves. The resulting directivities are 18.3dBi, 19.4dBi, and 20.0dBi, respectively. The corresponding main beam directions are 56°, 45°, and 38°. Moreover, the 3dB beamwidths are 3.7°, 3.4°, and 3.2°. Theoretical radiation patterns based on the TRM results are also computed for comparison. They are plotted as the black curves in Fig. 5.11. An infinite number of multiply reflected waves is assumed and summed in closed form in the formulation. It is observed that full-wave simulation and TRM results show good agreement. The predicted directivities from TRM are slightly lower than the FEKO simulation result. This may be due to the fact that the finite ground plane modeled in FEKO produces a not axial-symmetric pattern in the ϕ -direction, thus leading to an increased directivity.

In order to show the interplay between the attenuation constant and the length of a leaky wave antenna, a 200cm long conventional half-width microstrip LWA is simulated using FEKO for comparison. The structure is simulated as PEC on an infinitely large ground plane. Radiation patterns are plotted in polar format in Fig. 5.12. FEKO-simulated patterns at 5.3GHz, 6.2GHz and 7.1GHz are plotted in blue. The directivities are 11.0dBi, 13.4dBi, and 14.9dBi, respectively. The corresponding main beam directions are 58°, 46.5°, and 39.5°, and the 3dB beamwidth are 13.0°, 8.5°, and 6.6°. Radiation patterns based on TRM in conjunction with the equivalent magnetic current model are plotted in black. Again, the agreement between full-wave simulations and TRM-derived patterns is good. Comparing Fig. 5.11 and Fig. 5.12, it can be seen that the proposed two-section

design achieves a higher directivity and a narrower beamwidth at approximately the same beam directions even though both antennas are 200cm long.

To complete the performance comparison, the FEKO-simulated directivity and beamwidth of the conventional half-width MWLA and the proposed two-section design are summarized in Table 1 and Table 2, respectively. Table 1 shows the results for a short (26cm) and a long (200cm) conventional half-width microstrip LWA. It is observed that the beamwidth of the 200cm antenna is comparable to that of the much shorter antenna at low frequencies, becoming narrower only at high frequencies, where the attenuation constant is smaller. Table 2 summarizes the performance of a short (26cm) and a long (200cm) two-section microstrip LWA. It shows that the longer antenna always significantly outperforms the short one. The 200cm long two-section microstrip LWA achieves a beamwidth between 6.3° and 3.3° , with a scan range between 32° and 74° . It is clear that a microstrip LWA with a small α and a long aperture provides the highest directivity, the narrowest beamwidth, and the widest scanning range.

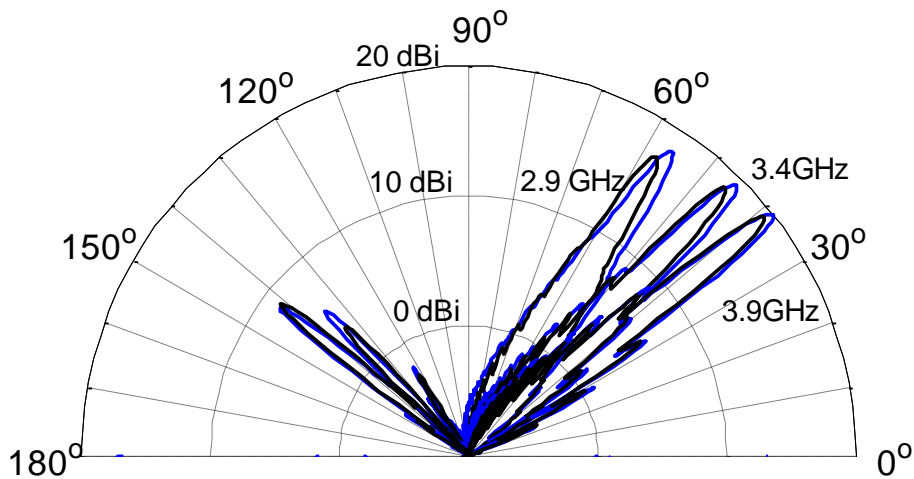


Fig. 5.11 The radiation patterns of the proposed two-section microstrip LWA at 2.9GHz, 3.4GHz and 3.9GHz. FEKO simulation results are shown as blue curves and the TRM predicted results are shown as black curves.

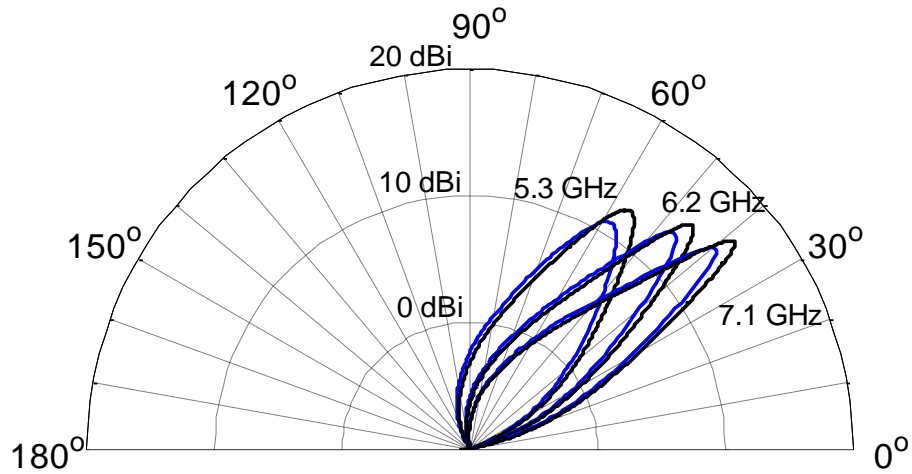


Fig. 5.12 The radiation patterns of the conventional half-width microstrip LWA at 5.1GHz, 6GHz and 7GHz. FEKO simulation results are shown as blue curves and the TRM predicted results are shown as black curves.

Table 1: Simulated Performances of Conventional Half-width microstrip LWAs.

| Frequency | DIR(dBi) | beamwidth | DIR(dBi) | beamwidth |
|-----------|-----------|-----------|------------|-----------|
| | 26cm long | | 200cm long | |
| 4.5 GHz | 7.2 | 32.7° | 7.2 | 32.6° |
| 5.0 GHz | 9.7 | 18.1° | 9.9 | 16.3° |
| 5.5 GHz | 10.9 | 15.3° | 11.7 | 11.5° |
| 6.0 GHz | 11.7 | 14.2° | 12.9 | 9.2° |
| 6.5 GHz | 12.2 | 13.8° | 13.9 | 7.7° |
| 7.0 GHz | 12.5 | 13.4° | 14.8 | 6.8° |

Table 2 Simulated Performances of Two-section microstrip LWAs.

| Frequency | DIR(dBi) | beamwidth | DIR(dBi) | beamwidth |
|-----------|-----------|-----------|------------|-----------|
| | 26cm long | | 200cm long | |
| 2.5 GHz | 10.2 | 20.6° | 15.3 | 6.3° |
| 2.9 GHz | 9.8 | 21.8° | 18.4 | 3.7° |
| 3.3 GHz | 9.6 | 22.5° | 19.5 | 3.4° |
| 3.7 GHz | 9.6 | 23.7° | 20.1 | 3.3° |
| 4.1 GHz | 9.7 | 24.4° | 20.5 | 3.3° |
| 4.5 GHz | 9.8 | 22.4° | 20.8 | 3.3° |

5.5 DISCUSSION

A two-section microstrip LWA with a narrow beam was designed in the previous sections. Here some radar related implications will be discussed. First, a narrow-beam microstrip LWA will improve the azimuth resolution for the range-azimuth tracking of targets. However, the narrower beamwidth will also reduce the “target bandwidth” and thus hamper the range resolution. This can be seen from the frequency-scanned radiation pattern in Fig. 5.8. As the beamwidth becomes narrower, the “target bandwidth” on a target located in a particular direction (corresponding to a vertical cut in Fig. 5.8) will also decrease. The trade-off between the antenna beamwidth and frequency bandwidth is an intrinsic property of the microstrip LWA and must be considered carefully for the intended application.

Second, while beamwidth is the primary concern for radar applications, the antenna radiation efficiency is also worth consideration. To simulate efficiencies while maintaining a reasonable computation time, the structures (both the conventional and the proposed two-section microstrip LWAs) are modeled as thin metal (copper or steel)

sheets on an infinitely large PEC ground plane. The efficiencies of the two 200cm long antennas in the previous section are plotted in Fig. 5.13. Both antennas are simulated with copper and steel. Efficiencies of the copper antennas versus frequency are plotted as blue curves, while those of the steel construction are plotted as black curves. The dash curves are the efficiencies of the conventional half-width microstrip LWAs. Results show that the efficiency is better than 94% with either copper or steel. The two solid curves are the efficiencies of the two-section microstrip LWAs. The efficiency of the steel antenna drops to 46% at 4.5GHz while the copper one is 87%. It is concluded that the efficiency is lower in the proposed two-section structure. This is because of the higher field confinement in the structure that leads to the lower attenuation constant. Consequently, construction with highly conductive metals is preferred. For dielectric-filled designs, dielectric loss will further lower the efficiency. The lower radiation efficiency of the new structure will lead to a slightly lower gain and lower received signal strength. However, the goal of achieving a narrower beamwidth is nonetheless achieved.

The reflection coefficient (S_{11}) of the 200cm two-section MWLA is also simulated in FEKO and shown in Fig. 5.14. It is seen that the coaxial cable feed achieves a better than -10dB matching between 2.6GHz and 3.6GHz. From 3.6GHz up to 4.5GHz, the matching is still better than -6dB (75% of the available power accepted by the antenna). Additional feed designs could be explored to further improve the matching performance [59].

The 200cm-long antenna with such fine features with high precision cannot be built at our machine shop. However, it is believed the construction is possible with proper machining tools. Also, even though 200cm appears to be quite long, there are platforms can support such an antenna, such as a vehicle or even a police stick, which can be

carried by law enforcement personnel. The proposed two-section microstrip LWA may serve well in these applications.

Lastly, we would like to point out some earlier works with similar structures [82, 83]. They are both based on rectangular waveguides and only air-filled structures were analyzed. Our analysis, derived from the MLWA, is applicable to different dielectric filling. Although our built prototype is air-filled and has a thick top conductor, we consider the proposed structure as a microstrip rather than a rectangular waveguide due to limitations in our TRM formulation. The thick top conductor could change the boundary condition around the edge of the top microstrip. However, the effect is not prominent since the measured results with a thick top conductor agree with those computed using TRM as shown in Fig. 9.

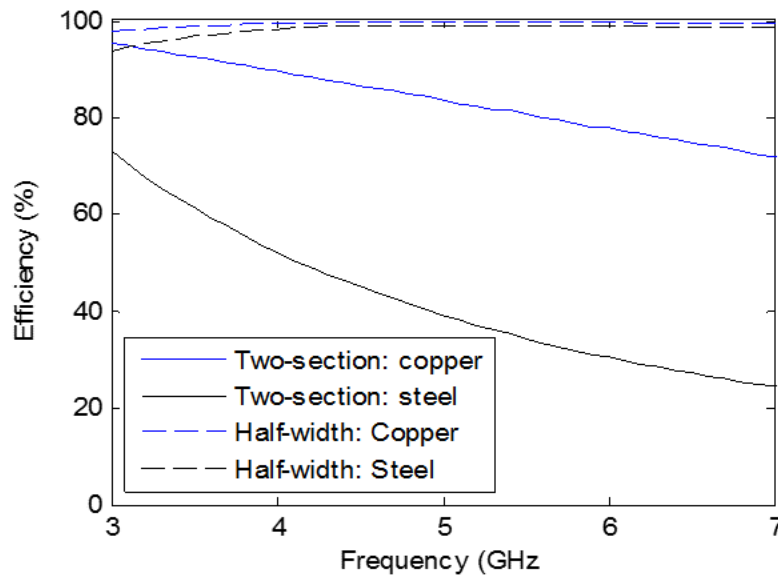


Fig. 5.13 Simulated efficiencies of the 200cm long conventional half-width microstrip LWA and the 200cm long two-section microstrip LWA. Both structures are simulated with copper and steel.

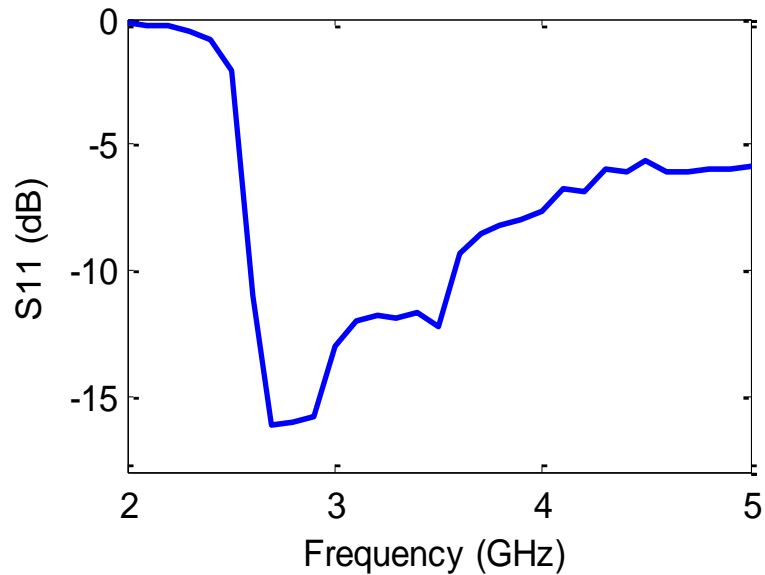


Fig. 5.14 Simulated S11 of the proposed 200cm two-section microstrip LWA using the MoM solver in FEKO.

5.6 CONCLUSION

In this chapter, a new two-section microstrip LWA was proposed to achieve a smaller attenuation constant in the structure. The complex propagation constant was derived using TRM and the results of different geometrical parameters were examined. Next, a two-section microstrip LWA was designed and built to the length of the conventional half-width microstrip LWA in Chapter 3 for a direct comparison. The propagation and attenuation constants of the new structure were extracted from the measured far-field patterns and they agreed well with the TRM results. Lastly, a long microstrip LWA antenna was simulated using full-wave simulation. The results showed that a narrow-beam microstrip LWA could be achieved by combining the small attenuation constant structure with a long aperture. Finally, the implications of employing a narrow-beam microstrip LWA for radar applications were discussed.

Chapter 6: 2-D Imaging Using a Microstrip LWA with Compressive Sensing

In the previous chapter, the azimuth resolution of a 2-D tracking system was improved by designing a microstrip LWA with a narrower beam. However, the trade-off between the antenna beamwidth and its frequency bandwidth becomes a major consideration for system planning. In this chapter, a different signal processing technique than the STFT is applied to improve the performance of the 2-D tracking system. Sec. 6.1 first discusses the compressive sensing technique, which is an emerging signal processing technique that can solve a highly underdetermined matrix equation under the sparsity constraint. Next, the 2-D tracking problem using a microstrip LWA is formulated in the framework of compressive sensing. The compressive sensing technique is tested with both point scatterer simulation and static target measurement. In Sec. 6.3, it is applied to measurement data of two walking human subjects and the results are compared with those processed with the STFT in Chapter 3. Furthermore, the capabilities to resolve closely spaced targets using compressive sensing for a short and a long microstrip LWA are discussed in Sec. 6.4 and Sec. 6.5, respectively. Sec. 6.6 provides some conclusions reached from this study.

6.1 COMPRESSIVE SENSING

Compressive sensing [84, 85] addresses the problem of how to reconstruct a complex signal $x \in \mathcal{C}^N$ from a linear measurement $y = Ax, A \in \mathcal{C}^{M \times N}$ when the problem is underdetermined, i.e. $M < N$. Since the problem is underdetermined, there exist many possible solutions and the solution with the least amount of non-zero entries is desired among all the solutions. The underlying assumption is that the sparsest solution is

often the most desirable one in many physical problems of interest. This process can be written as an optimization problem as:

$$\min_{\mathbf{x} \in \mathcal{C}^N} \{\|\mathbf{x}\|_0, \text{subject to } \mathbf{y} = \mathbf{Ax}\} \quad (6.1)$$

where $\|\cdot\|_0$ denotes the L-0 norm. However, the above optimization problem is NP-hard and can only be solved by exhaustively comparing the L-0 norms of all solutions. As the measurement matrix gets larger, this exhaustive approach is not feasible. Alternatively, a basis pursuit problem can be formulated using the L-1 norm [86]:

$$\min_{\mathbf{x} \in \mathcal{C}^N} \{\|\mathbf{x}\|_1, \text{subject to } \mathbf{y} = \mathbf{Ax}\} \quad (6.2)$$

It has been shown that under certain conditions [87, 88, 89, 90, 91], the solutions of the two problems are unique and identical. Moreover, the problem in (6.2) is a convex problem and can be solved as a linear program with inequality constraints. There exist various numerical methods developed for this type of problem. However, these solvers are not designed for a large amount of inequality constraints encountered in a compressive sensing problem. Other efficient algorithms have been developed, such as first-order primal-dual algorithms [92, 93]. The name follows the fact that these methods explicitly update both the primal and dual variables at every iteration. They are more efficient in two ways. First, they take fewer steps to converge. Second, they can take advantage of certain type of matrices, such as the discrete Fourier transform matrix, for a fast matrix-vector product operation. In this chapter, the YALL1 solver [93] based on the first-order primal-dual alternating direction algorithm is used.

Compressive sensing has already been applied to various radar imaging problems to date [94]. For example, it has been combined with randomized frequencies to overcome the unambiguous down range limit of using linearly spaced frequencies. The concept was implemented in random binary waveforms and frequency-hopped measurements [95, 96]. Compressive sensing has also been applied to mono-static synthetic aperture radar (SAR) with randomized sampling position to overcome the beamwidth, grating lobe, and sidelobe limitations of an array with uniform spacing [97]. Lastly, it has been applied to compute the joint time-frequency distribution of targets to achieve a more localized time-frequency content, which is an essential tool to find the target range and velocity at once [98, 99]. In the next section, I will reformulate the problem of forming a 2-D range-azimuth image into the framework of compressive sensing.

6.2 PROBLEM FORMULATION AND VALIDATION

In Chapter 3, it has been shown that a 2-D image can be generated from the 1-D frequency data collected through a frequency-scanned antenna. We first inverse-Fourier transformed the collected frequency response into the range domain for target separation. Afterwards, we applied the STFT to generate a 2-D range-azimuth image. The problem to form a 2-D range-azimuth image from the 1-D frequency data received through a frequency-scanned antenna is essentially an underdetermined problem, i.e. to find a few targets in a large 2-D space while the measurement is a 1-D data set. The problem appears to be well suited for compressive sensing. We can consider the \mathbf{x} vector in (6.2) with N entries as N possible target positions, and the received frequency response as the \mathbf{y} vector, which has M frequencies. As for the matrix \mathbf{A} , we interpret the equality constraints in (6.2) as a linear combination of vectors:

$$\mathbf{y} = \mathbf{A}\mathbf{x} = \sum_{i=1}^N \mathbf{a}_i x_i \quad (6.3)$$

where \mathbf{a}_i is the i -th column vector of the \mathbf{A} matrix. In this form, the total frequency response (\mathbf{y}) is a linear combination of N frequency responses (\mathbf{a}_i) weighted by N targets (x_i). We compare (6.3) with the point scatter model used in Chapter 3. The frequency response due to all the targets can be computed using the following equation, which is simplified and reorganized from (3.1):

$$\frac{V^r(f)}{V^i} = \sum_{i=1}^N \left[\frac{\lambda(f) G(f, \theta_i)}{(4\pi)^{3/2}} \cdot \frac{e^{-j2k(f)R_i}}{R_i^2} \right] \sqrt{\sigma_i} \quad (6.4)$$

where (R_i, θ_i) and σ_i are the position and RCS of the i -th point scatterer, V^i is the excitation voltage which is assumed to be constant across the frequency band, and V^r is the total received voltage, which is a function of frequency. By comparing (6.3) and (3.1), we see that x_i can be equated to the square root of the RCS of the i -th target while \mathbf{a}_i corresponds to the frequency response of a target with unity RCS placed at (R_i, θ_i) . To apply compressive sensing to generate an image, we take the following steps. First, we choose the potential target positions. An arbitrary shape of interested area could be used. Next, we compute the corresponding \mathbf{a}_i using (3.1) with the theoretical directivity values derived from TRM. Lastly, we assemble the final \mathbf{A} matrix and apply the compressive sensing solver, YALL1, to find the target positions from the frequency response. It is noted that higher order interactions between targets are ignored. Otherwise the problem cannot be solved by compressive sensing.

The compressive sensing imaging using a microstrip LWA is first tested with point-target simulation data. The potential target positions are limited to a polar sector of

space, where the range extent is set from 0m to 15m and the azimuth extent is set from 33° to 75° . This area is further uniformly discretized into pixels with 3.75cm in range and 1° in azimuth. The corresponding \mathbf{a}_i for all these positions are computed and assembled as the \mathbf{A} matrix. Two targets are placed in the scene at (4m, $\theta=55^\circ$) and (5m, $\theta=40^\circ$) with unity RCS for testing. The target positions are the same as in Sec. 3.2. The simulated frequency response is first generated using the computed \mathbf{A} matrix and the target information. The resulting data are then inverted into an image using the same \mathbf{A} matrix and YALL1. YALL1 supports a number of cost functions, and we found the best result using the combined L1-L2 cost function:

$$\min \left\{ \|\mathbf{x}\|_1 + \frac{1}{\rho} \|\mathbf{y} - \mathbf{A}\mathbf{x}\|_2 \right\} \quad (6.5)$$

where ρ is a weighting parameter to add the residual L-2 norm of the linear constrains in the cost function. The residual L-2 norm of the linear constrains is usually from the additive white Gaussian noise in the \mathbf{y} vector. The choice of ρ is related to the signal-to-noise ratio. Overall, we can consider (6.5) as a combined imaging and de-noising algorithm. The resulting quality of the image is sensitive to the choice of ρ . If ρ is set too high, targets will not be revealed. If ρ is set too low, the target response will show too much spreading. In this chapter, the parameter ρ is experimentally determined for different sets of data. Fig. 6.1(a) shows the range-azimuth image obtained by using YALL1 for the point-scatterer simulation data with ρ set to $1e-5$. In comparison to Fig. 3.6(d), the two targets are much better focused in both range and azimuth. Next, the range-azimuth image of the two-trihedral measurement in Sec. 3.2 is also generated using YALL1 with ρ set to $1e-4$. In this case, the computed \mathbf{A} matrix is still used. The result is shown in Fig. 6.2. In comparison to Fig. 3.7(d) in Chapter 3, the compressive sensing

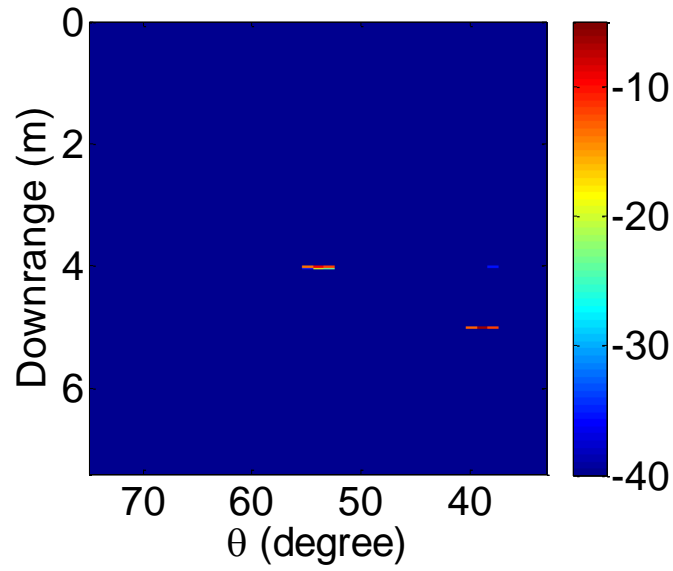


Fig. 6.1 Range-azimuth images generated using the L1-norm minimization with point scatterer simulation.

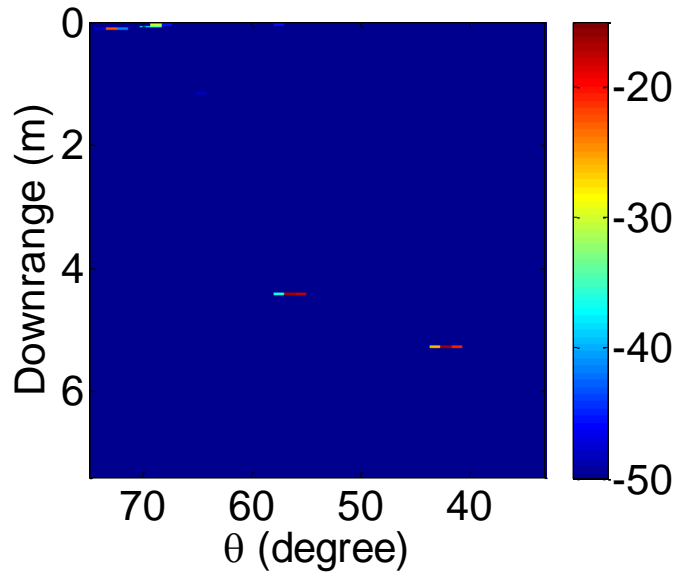


Fig. 6.2 Range-azimuth images generated using the L1-norm minimization of the two-trihedral measurement.

gives a much more focused image. In these two cases, ρ is set to the maximum values that still reveal the two targets in the individual data sets.

6.3 SNAPSHOTS OF 2-D TRACKING USING COMPRESSIVE SENSING

The entire sequence of human measurement data are then processed with ρ set to $1.5e-7$. This value is kept for the whole sequence since the noise level should remain the same in the measurement. Eight snapshots are presented from Fig. 6.3(a) to Fig. 6.3(h). These figures are one-to-one counterparts of those in Fig. 3.8. Over the entire sequence, the compressive sensing always gives a better localization of the targets as compared to the STFT processing. In Fig. 6.3(a), only target (B) is seen. This is because the shadow casted on target (A) from target (B) makes target (A) disappear altogether in the snapshot. This is different from the same snapshot generated using the STFT shown in Fig. 3.8(a). In the other seven snapshots, both targets can be seen with a focused response for each one. It is also noted that the sharpening of target responses comes at the expense of computation time. Each snapshot of the human tracking measurement took more than six minutes to process using YALL1 while the STFT processing took less than 0.15 sec on the same computer (with an Intel® Core™ i5 CPU and 8GB of memory).

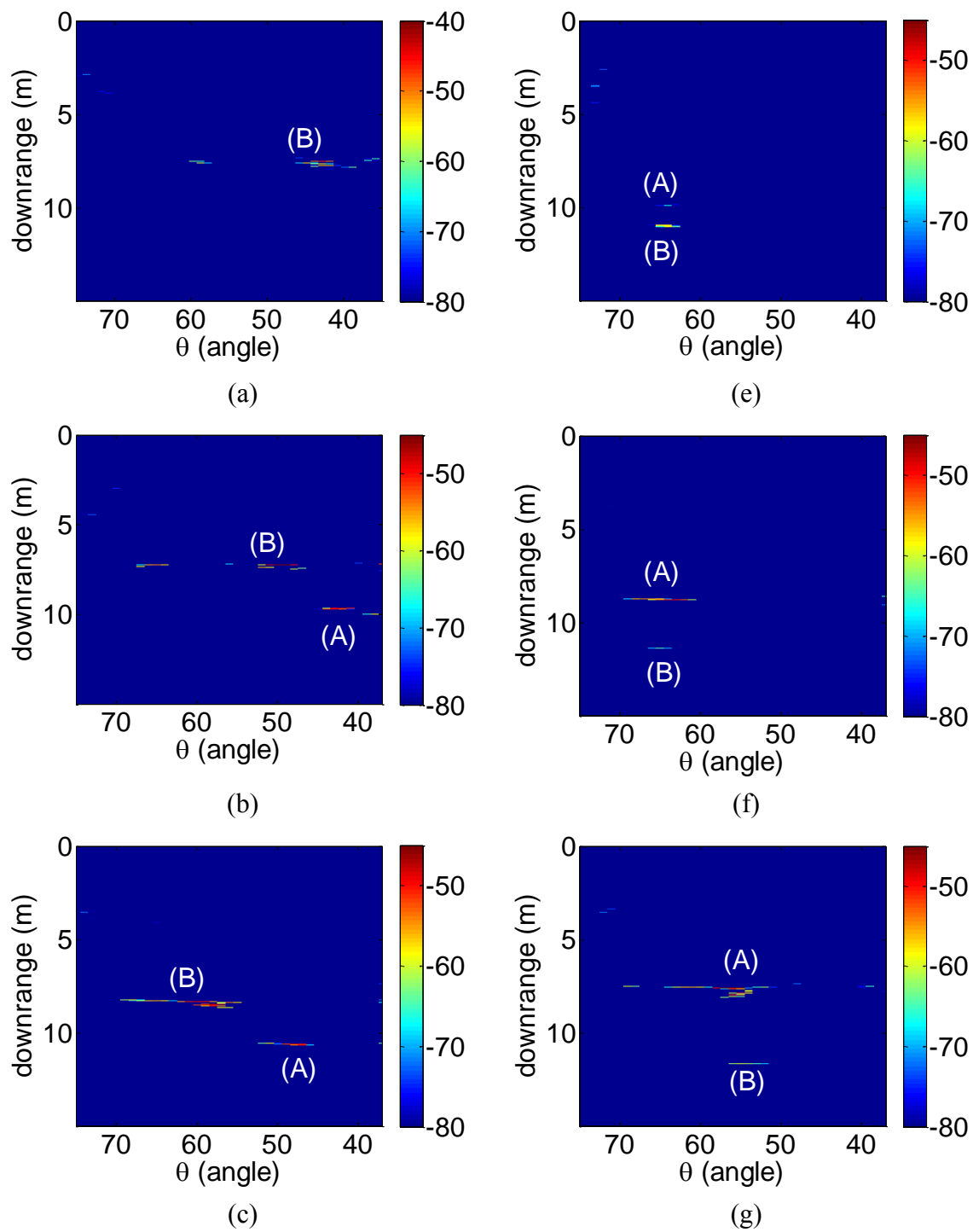


Fig. 6.3 Range-azimuth images of the human tracking measurement generated using L1-norm minimization. (a) - (h) are the same snapshot as Fig. 3.12(a) - (h).

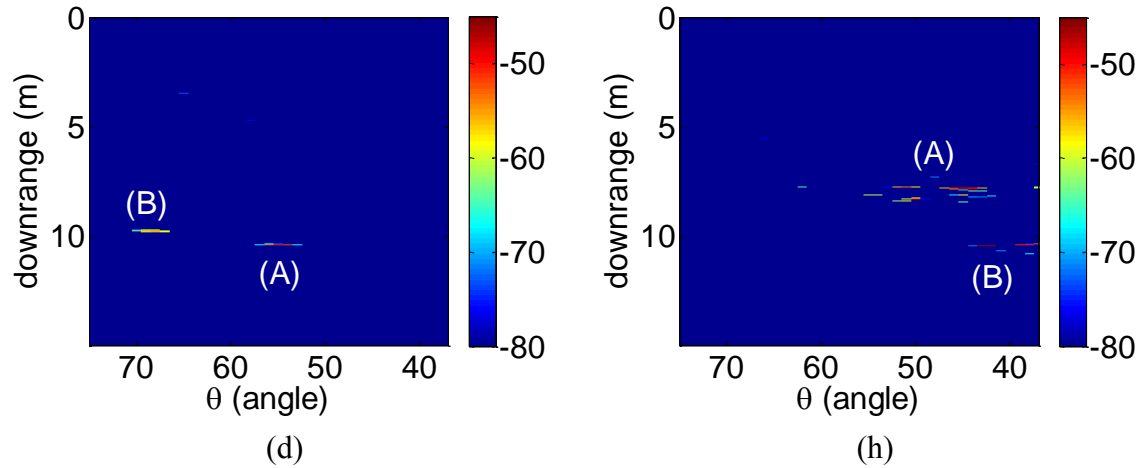


Fig. 6.3 Range-azimuth images of the human tracking measurement generated using L1-norm minimization. (a) - (h) are the same snapshot as Fig. 3.12(a) - (h).

6.4 RESOLVING CAPABILITY OF COMPRESSIVE SENSING

In the previous section, it has been shown that compressive sensing works well for measurement data of two walking humans. The resulting images are better focused compared to the snapshots generated using the STFT. However, the capability to resolve closely spaced targets is not verified yet. For conventional array processing, the azimuth resolving capability is the 3dB beamwidth of the antenna and the down range resolution is inversely proportional to the 3dB frequency bandwidth. In order to test the resolving capability of the short microstrip LWA using compressive sensing, a point scatterer simulation is carried out. The spacing of the targets in the azimuth dimension is set to the 3dB beamwidth and the range difference corresponds to the 3dB frequency bandwidth. Afterwards, a simulated frequency response of these closely spaced targets is generated using the point scatterer model. Lastly, YALL1 is applied to form the 2-D image. The 3dB beamwidth and bandwidth of the 28.5cm long half-width microstrip LWA are shown

in Fig. 6.4. It is noted that the “target bandwidth” and azimuth beamwidth are both functions of the direction. The beamwidth is about 8 degrees for most of the target directions and the 3dB bandwidth ranges from 700MHz to 2GHz. The frequency bandwidth is widest at 38° , of which the higher edge of the 3dB bandwidth corresponds to the highest frequency in the setup, 8.3GHz. As the target moves even closer to the endfire direction, part of the 3dB bandwidth will not be collected and it shows as the reduced bandwidth. In the testing, three sets of targets are placed around $\theta = 40^\circ, 60^\circ, 70^\circ$ to evaluate the resolving capability. The ground truth image is shown in Fig. 6.5(a). All the targets have unity RCS. Next, the simulated frequency response of all the targets present is processed with compressive sensing and the settings are as follows. The frequency is set from 4.3GHz to 8.3GHz with 401 frequency points. The azimuth pixel size is set to one degree, and the range pixel size is set to 3.75cm. The 2-D image generated by compressive sensing is shown in Fig. 6.5(b). It can be observed that the two targets at the same range are barely resolved in the azimuth dimension. Moreover, the target closest to the broadside direction of the nine targets is substantially weaker than the others. It is also noted that there are significant artifacts in the azimuth dimension for the two sets at $\theta = 60^\circ$ and 70° . Lastly, the targets are resolved in down range in all three sets but the range response is not as focused as the ground truth.

The same data are also processed with the STFT using two different windows. The results with a 113cm and a 30cm Hamming windows are shown in Fig. 6.6(a) and Fig. 6.6(b), respectively. The 113cm Hamming window resolves the closely spaced targets in azimuth but cannot resolve the targets in down range for all three sets of targets. Moreover, there are artifacts in the azimuth domain (similar to the compressive sensing result) and the azimuth responses are broader compared to compressive sensing. As for the 30cm Hamming window, it resolves the down range in the three sets of targets.

However, the 30cm window cannot resolve the closely spaced targets in azimuth. Overall, the size of the Hamming window determines the trade-off of the resolutions in the azimuth and down range dimensions when the STFT is used to image a 2-D scene with a frequency-scanned antenna. As observed in Fig. 6.6, the target separation can be achieved either in the down range or the azimuth dimension, but not simultaneously. For comparison, the targets are always resolved both in the azimuth and down range dimensions when compressive sensing is applied. It can be concluded that compressive sensing has higher resolving capability than the STFT. However, compressive sensing can barely resolve targets spaced by the 3dB beamwidth. The result also contains artifacts in the azimuth dimension. It seems that compressive sensing does not improve the azimuth resolution much.

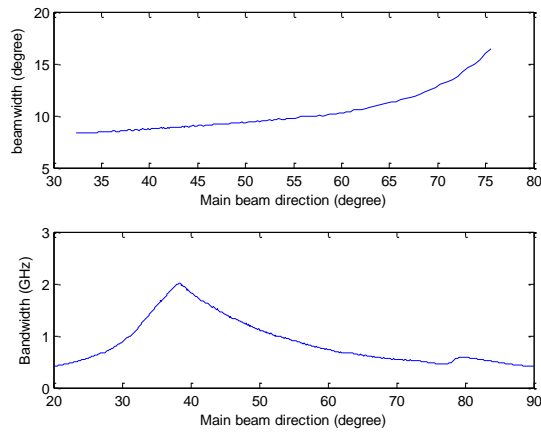


Fig. 6.4 The two-way 3dB beamwidth and bandwidth of the 28.5cm long half-width microstrip LWA.

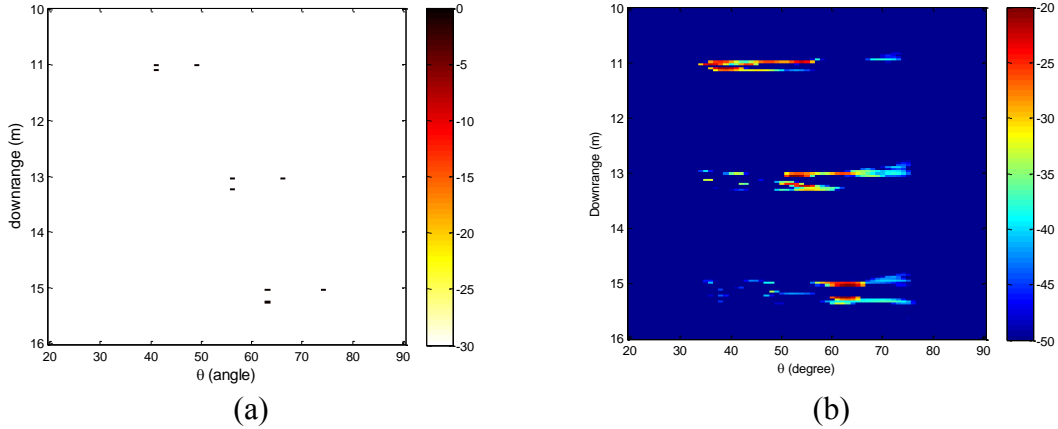


Fig. 6.5 (a) The ground truth of three sets of targets placed 3dB in azimuth and down range locations. The color code is reversed compared to the others to better show the targets. (b) The 2-D image generated by compressive sensing.

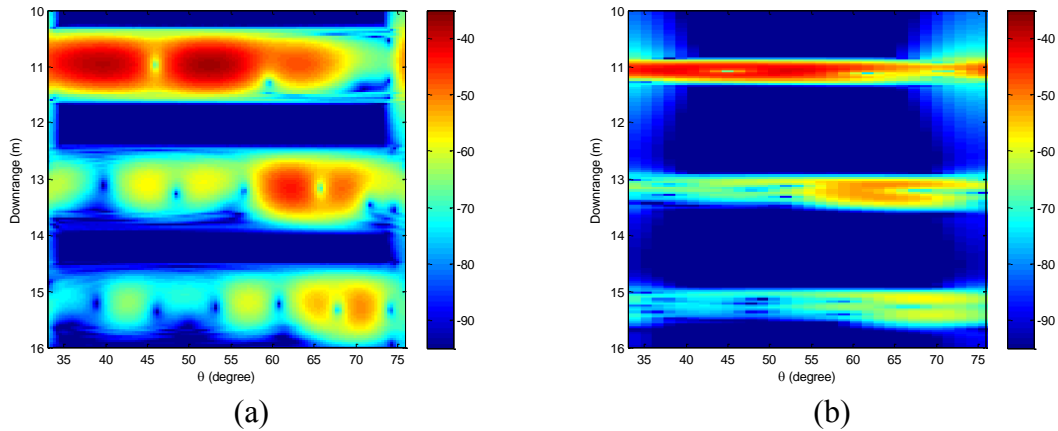


Fig. 6.6 The 2-D image generated using the STFT. (a) 113cm Hamming window. (b) 30cm Hamming window.

6.5 COMPRESSIVE SENSING AND A LONG MICROSTRIP LWA

In order to further improve the azimuth resolution of the 2-D imaging system, the 90cm long half-width microstrip LWA developed in Chapter 4 is combined with compressive sensing. However, the far field distance of the 90cm long antenna at 5.3 GHz is 28.6m based on the $(2D^2)/\lambda$ formula. As a result, the targets to be imaged will likely be in the near field region of the antenna and the point source approximation of the

antenna is no longer valid. In order to test the potential performance degradation due to the model mismatch, the electric near field of the antenna is calculated using numerical integration as:

$$\frac{-jk_0}{4\pi} \int_0^{0.9} \sin(\theta(z)) \cdot \exp[(-\alpha - j\beta)z] \cdot \frac{\exp[-jk_0R(z)]}{R(z)} dz \quad (6.6)$$

where R and θ are respectively the distance and direction of a near-field target to different parts on the antenna aperture. The target response is the square of the electric near field multiplied by the square root of the RCS of the target. A grid of targets is setup for testing as shown in Fig. 6.7(a) to Fig. 6.7(d), where the targets are placed at 90m, 30m, 10m, and 3m in these figures, respectively. The results obtained using compressive sensing with the far-field \mathbf{A} matrix are shown in Fig. 6.7(e) to Fig. 6.7(h). It can be seen that as the targets get closer to the antenna, the resulting images get blurrier. It is particular obvious in Fig. 6.7(h), where the targets are placed at 4m, 6m, and 8m away from the radar. The three targets at 4m are blurrier than the targets at the other distances. It can be concluded that the model mismatch due to the far-field \mathbf{A} matrix is the worst when the target is very close to the radar.

For comparison, a near-field \mathbf{A} matrix is computed exhaustively by changing the target position across the whole image plane. The image of the targets placed from 4m to 8m using the near-field \mathbf{A} is shown in Fig. 6.8. In comparison to Fig. 6.7 (h), it is clear that all the targets are now much better focused. It is noted that although the targets near the broadside direction are better focused compared to Fig. 6.7 (h), they are still blurrier than the other targets in Fig. 6.8. This is because the antenna beam is the broadest near the broadside direction. Therefore, the ability of compressive sensing to focus the target in azimuth is still limited by the physical beamwidth of the antenna.

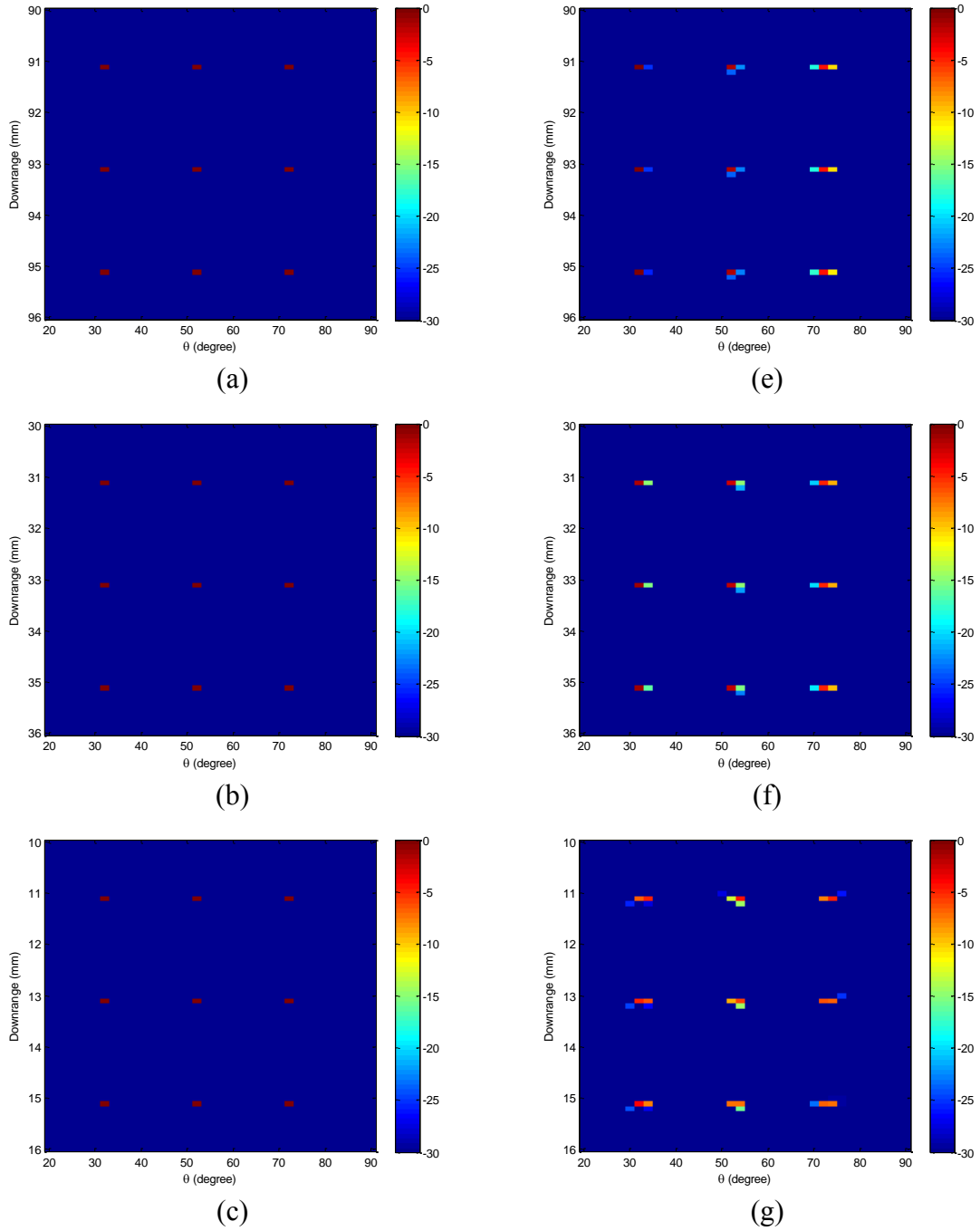


Fig. 6.7 Testing of the near field effect at 90m, 30m, 10m, and 3m. The ground truths are on the left and the images obtained using compressive sensing are shown on the right.

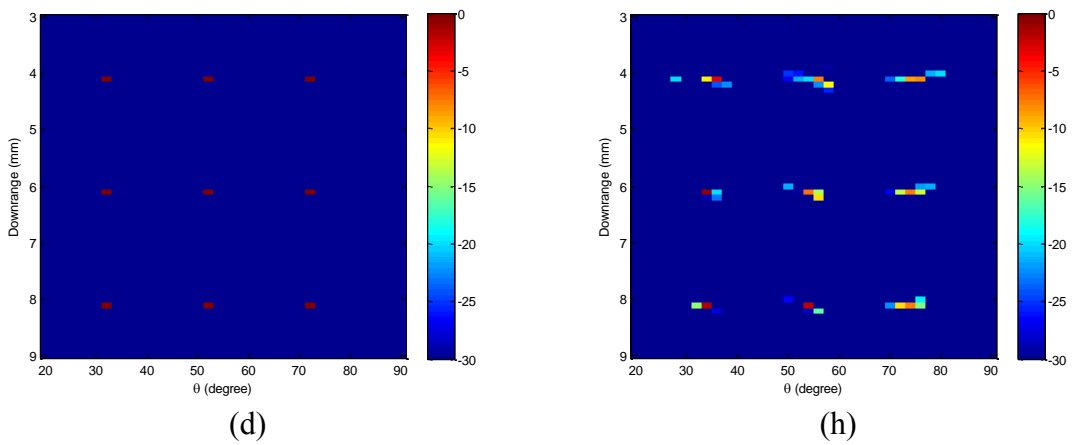


Fig. 6.7 Testing of the near field effect at 90m, 30m, 10m, and 3m. The ground truths are on the left and the images obtained using compressive sensing are shown on the right.

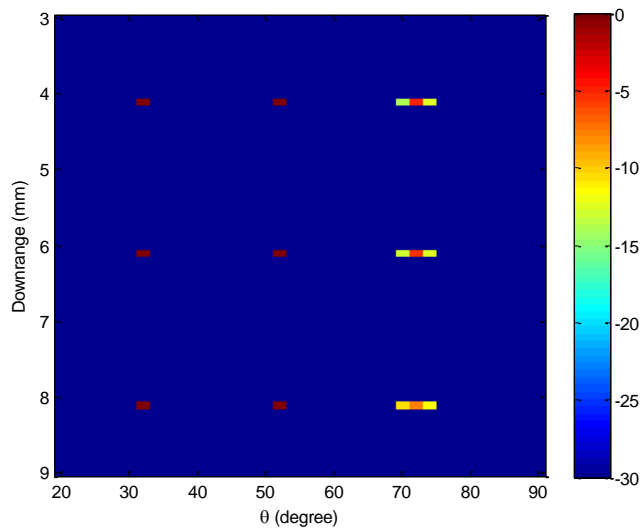


Fig. 6.8 The reconstructed near-field image using a matching near-field \mathbf{A} matrix.

The resolving capability of combining compressive sensing, a long microstrip LWA, and a near-field \mathbf{A} matrix is next examined. The same nine targets used in the previous resolution testing in Fig. 6.5(a) are tested with the 90cm long antenna. The resulting compressive sensing image is plotted in Fig. 6.9. It is clear that the range and azimuth of all 9 targets are resolved. However, there are also some artifacts near the targets around 13m as well as 11m in both the down range and azimuth dimensions. The 3dB beamwidth and bandwidth of the 90cm long half-width microstrip LWA are shown in Fig. 6.10. Comparing to Fig. 6.4, the 90cm-long antenna achieves a narrower beamwidth across the whole scanning range. However, the corresponding bandwidth is much narrower. The frequency bandwidth ranges from 200MHz to 1GHz, compared to 700MHz to 2GHz of the short antenna. This indicates that the long antenna may not resolve the targets in the down range dimension. However, the long antenna can actually

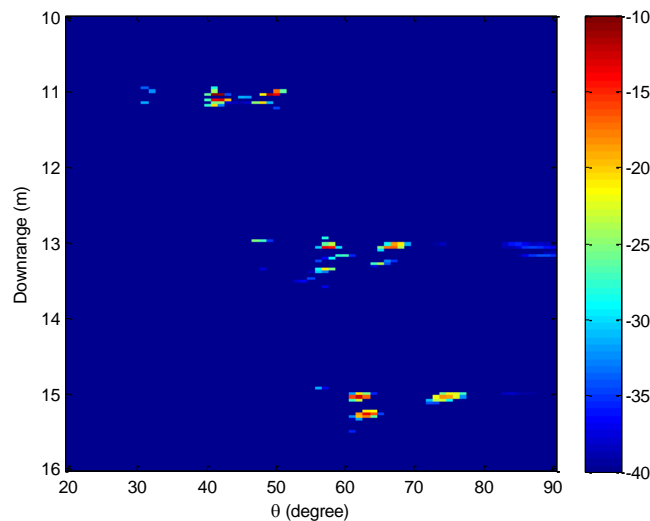


Fig. 6.9 The compressive sensing image of Fig. 6.5(a) using the 90cm-long microstrip LWA. The targets are clearly resolved in both the azimuth and down range dimensions.

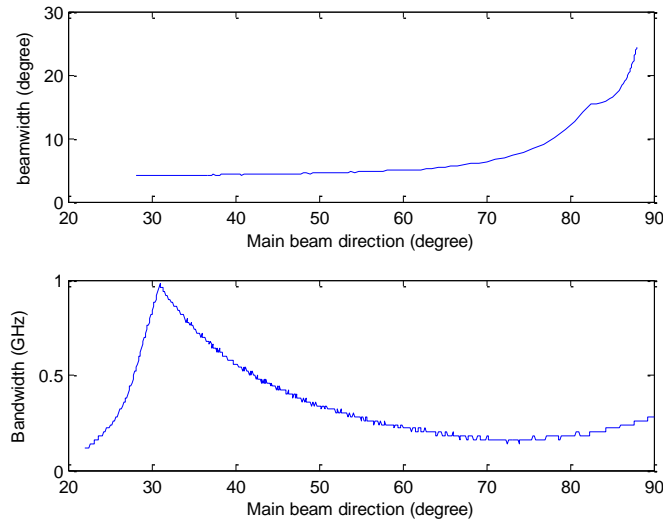


Fig. 6.10 The 3dB beamwidth and bandwidth of the 90cm-long microstrip LWA.

resolve the down range dimension as shown in Fig. 6.9. Thus, it is concluded that the long antenna improves azimuth resolution with a narrower beam while compressive sensing achieves super resolution in the down range dimension with the expense of some artifacts. Overall, the combination of a long microstrip LWA and compressive sensing achieves the best result.

6.6 CONCLUSION

In this chapter, the compressive sensing technique was applied to the 2-D range-azimuth imaging problem using a frequency-scanned microstrip LWA. The problem to find the targets in a large 2-D range-azimuth space with a 1-D (frequency) data was formulated into the framework of compressive sensing. Compressive sensing resulted in a more focused image than the STFT in both the case of point scatterer simulation and measured data for two static targets. Next, compressive sensing was applied to a sequence of data of two walking human subjects and sharper images were also achieved. However, a more focused image does not necessarily mean two closely spaced targets

can be resolved. The compressive sensing approach was tested against point scatterer simulations with closely spaced targets in both the down range and azimuth dimensions to verify its resolving capability. The results showed that the azimuth resolution is still predominantly governed by the antenna beamwidth. Lastly, a long microstrip LWA with a narrow beam was combined with compressive sensing. It was found that a near-field data model was required since the antenna is long and the operating frequency is high. Comparing the compressive sensing images using a short and a long microstrip LWAs, the long antenna achieved a better azimuth resolution with the narrower beam. At the same time, compressive sensing essentially compensated for the loss of bandwidth in the long antenna and achieved nearly the same down range resolution as the short antenna. Therefore, the combination of a long microstrip LWA with compressive sensing yielded the best imaging performance.

Chapter 7: Radar Cross-Section of a Microstrip LWA

7.1 INTRODUCTION

In the previous chapters, the microstrip LWA was applied to the human tracking problem. Different aspect of the system was investigated in the different Chapters, including radar architecture, antenna design, and signal processing. In this chapter, the objective is not to improve the tracking performance but focuses on the radar cross-section (RCS) of a microstrip LWA. This property of an antenna is important because it could be the prominent contributor of the total RCS of a stealthy vehicle. Moreover, the scattering from an antenna cannot be fully eliminated since the antenna still receives and radiates power. As a result, the RCS characteristic of the antenna may be used to identify different vehicles [100].

The RCS of two structures related to the microstrip LWA have been investigated in the past. The RCS of a microstrip patch antenna was reported in [101]. Since a patch antenna is a high-Q resonator, the fundamental as well as higher order resonances can be observed through its RCS response. A more closely related structure to the microstrip LWA is a long trough, which can arise from gaps and seams in a smooth conducting body. In [102], Shamansky and Dominek showed that the traveling wave mechanism in the trough gives rise to prominent features in the RCS. In this work, the RCS of a half-width MLWA is investigated. First, the monostatic RCS of a microstrip LWA obtained using full-wave simulation and measurement are presented in Sec. 7.2. To better understand the various scattering features, the antenna mode scattering and structural mode scattering are separately modeled using different approximations in Sec. 7.3. As a result, the correspondence between the observed features and the different scattering mechanisms can be clearly established. In Sec. 7.4, the behavior of the antenna mode scattering is further interpreted using a time-of-arrival ray picture. It is shown that the

unique range-extended feature is due to a combination of the finite continuous aperture and the dispersive group delay of the leaky mode. Sec. 7.5 is the conclusion.

7.2 RADIATION PROPERTIES OF A MICROSTRIP LWA

Before presenting the RCS of a microstrip LWA, the radiation characteristics of a microstrip LWA is first reviewed, which are closely related to the properties of the microstrip leaky mode. The cross section of the half-width microstrip LWA for studying the RCS is illustrated in the inset of Fig. 7.1. The antenna under consideration consists of a metal ground plane, a 15mm wide microstrip line elevated 2mm from the ground plane, and a vertical shorting plane on the left side. The length of the antenna in the longitudinal direction (z-direction) is 29cm. The antenna is fed on one end via a coaxial line while the other end is left as an open. The antenna operates from 4GHz to 8GHz with a frequency-scanned beam. The propagation constant (β) and attenuation constant (α) of the two lowest order leaky modes are computed from 2GHz to 20GHz using TRM and shown in Fig. 7.1. Below 13GHz, only the lowest order leaky mode can exist. Its propagation constant determines the progressive phase shift along the z-direction, and thus controls the main beam direction. On the other hand, the attenuation constant determines the amplitude tapering along the aperture length, and thus affects the gain value and the antenna beamwidth. As frequency is increased, the propagation constant increases from nearly zero to the free space wave number. As a result, the beam steers from the broadside ($\theta=90^\circ$) toward the endfire direction ($\theta=0^\circ$). Along with the change in the propagation constant, the attenuation constant decreases as a function of frequency. This results in a higher antenna gain and a narrower beamwidth at higher frequencies. As for the second order leaky mode, the general operating principle is the same but starts at a higher frequency.

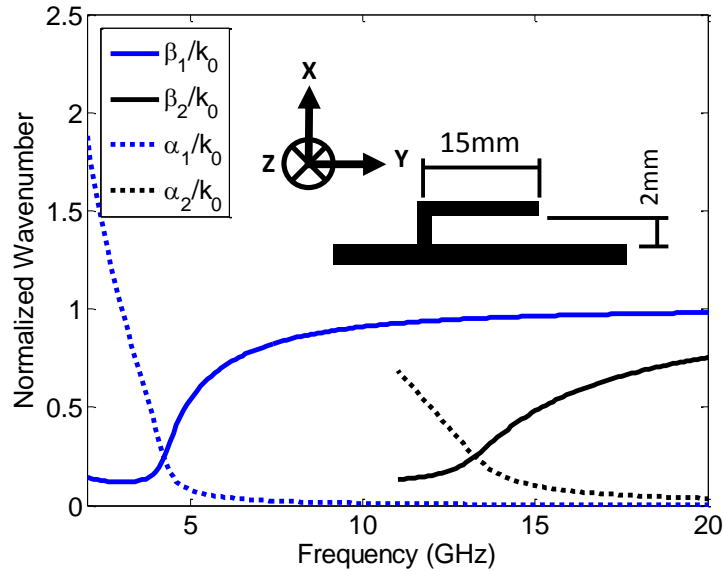


Fig. 7.1 The propagation and attenuation constants of a half-width microstrip LWA shown in the inset. These quantities are computed using TRM and normalized with respect to the free space wave number. The blue curves are for the lowest order leaky mode and the black curves are for the next higher order leaky mode.

Next, the broadband RCS of the half-width microstrip LWA is simulated and measured. The microstrip LWA is first simulated using the method of moments solver in FEKO [72]. In the simulation setup, the antenna is embedded in an infinite ground plane and the feed port is connected to a short load. The polarization of the incident plane wave is set to H-pol, i.e., the electric field is in the y-direction in Fig. 7.1. The simulated monostatic HH-pol RCS versus frequency (from 2GHz to 13GHz) and aspect is plotted in Fig. 7.2. It is noted that only the lowest order leaky mode is excited below 13GHz. The peak RCS is normalized to 0dB and the aspect angle θ is defined with respect to the z-axis. Two prominent features, labeled as (i) and (ii), are observed. Feature (i) is a strong function of the aspect angle and frequency. As frequency is increased, the RCS peak changes from broadside to the endfire direction. Such phenomenon is similar to the

frequency-scanned beam of a microstrip LWA. Feature (ii) is a strong flash that occurs at broadside, with associated sidelobe patterns in the angular dimension.

An alternative way of displaying the RCS data is in the range-aspect domain. The RCS data from 2GHz to 13GHz are windowed using a Hamming window and inverse-Fourier transformed to the range domain for each aspect angle. Moreover, the rotation center at the left edge is shifted to 29cm in range to better illustrate the early time features. The result is presented in Fig. 7.3. It shows three prominent features in the range-aspect plot and they are labeled as (a), (b) and (c) in an increasing order of range delay. Feature (a) is a range-focused feature, which corresponds to the response of a point scatterer that is offset by 29cm from the rotation center. Feature (b) is a range-extended one. It starts from 29cm and extends more in range as θ is increased. Feature (c) is similar to feature (b) but with a narrower range extension and it starts at 58cm.

Measured RCS data are also collected from a half-width microstrip LWA with the described parameters. The antenna is mounted on a 60cm long almond-shape ground plane and the whole unit is mounted on a rotator to perform the frequency-aspect measurement. A broadband horn is connected to a vector network analyzer to continuously collect data from 2GHz to 13GHz. Two sets of measurement are collected, the RCS data of the ground plane alone and the RCS data with the half-width microstrip LWA mounted on the ground plane. The first result is then subtracted from the second one to remove the effect of the finite ground plane. In addition, the gain and phase variations of the horn are equalized. The result is processed and plotted in the range-aspect format as shown in Fig. 7.4 with the peak amplitude normalized to 0dB. The three prominent features identified in Fig. 7.3 are clearly seen in the measurement, although the signal-to-noise ratio is limited in comparison to the simulation. The three features will be further modeled and discussed in the next section.

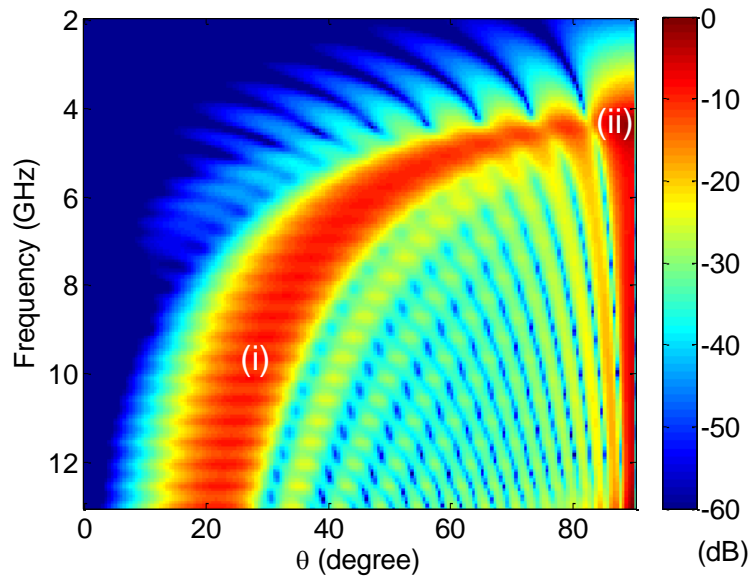


Fig. 7.2 Simulated RCS of a 29cm-long half-width microstrip LWA as a function of frequency and aspect angle.

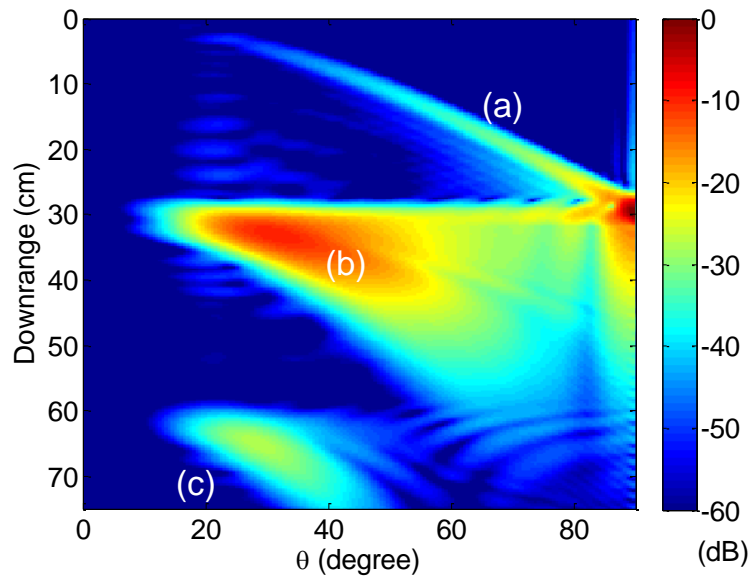


Fig. 7.3 Simulated RCS of a 29cm-long half-width microstrip LWA as a function of range and aspect angle.

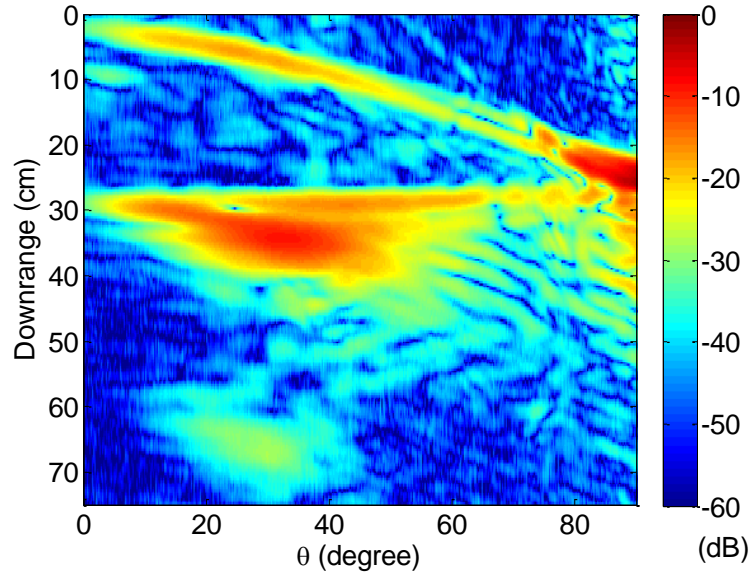


Fig. 7.4 Measured RCS of a 29cm-long half-width microstrip LWA as a function of range and aspect angle.

7.3 MODELING OF INDIVIDUAL SCATTERING MECHANISMS

It is well-known that the scattering from an antenna can be divided into the antenna mode scattering and structural mode scattering [103]. The former is related to the radiation property of the antenna. Power received into the antenna can be reflected back by the source impedance connected to the antenna input port. Then, the reflected power re-radiates as a source of backscattering. The relationship between the antenna mode scattering and the radiation property of the antenna is given explicitly in [103] as:

$$\sigma_{ant} = \frac{\Gamma^2 G^2(\theta, \phi) \lambda^2}{4\pi} \quad (7.1)$$

where σ_{ant} is the RCS due to the antenna mode scattering, Γ is the reflection coefficient due to the mismatch between the source impedance and the antenna, G is the antenna

gain pattern and λ is the wavelength. On the other hand, the structure of the antenna itself also contributes to backscattering and it should be modeled separately.

The antenna mode scattering is modeled based on the gain of the antenna. To compute the antenna gain pattern, it is assumed that an equivalent magnetic current bearing the propagation and attenuation constants of the leaky mode exists on the open edge of the microstrip LWA. Image theory is used to account for the ground plane. The far-field pattern is then readily found by using the free-space radiation integral over the 29cm length of the antenna. Although (7.1) is a power relationship, the full complex scattered field is computed to preserve the phase information, which will allow us to model the range domain characteristics. The antenna mode scattering is computed over frequency (2GHz to 13GHz) and aspect using (7.1) with the computed antenna gain. The data are then processed into the range-aspect plot as described in the previous section. The results are shown in Fig. 7.5(a). It is observed that the predicted feature matches quite well with the range-extended feature (b) in Fig. 7.1. It is also noted that the region around $\theta=30^\circ$ is particularly strong. This is because the structure is exposed to the broadest bandwidth in this angular region, as can be seen through the RCS vs. frequency and aspect pattern in Fig. 7.2. Moreover, the azimuth direction of this prominent feature is related to the frequency bandwidth used.

Higher-order bounces in the antenna mode scattering can also be modeled in a similar fashion. It is assumed the excited leaky mode bounces between the two ends of the microstrip LWA structure where the far end of the antenna is a perfect open. The RCS contribution from the first higher-order bounce (i.e., one additional round trip in the antenna) is then simply the antenna mode scattering discussed in the last paragraph multiplied by $\exp[(-\alpha - j\beta)2L]$, where α is the attenuation constant, β is the propagation constant, and $L = 29\text{cm}$ is the length of the antenna. The resulting range-

aspect plot due to this mechanism is shown in Fig. 7.5(b). It is observed that this feature matches well with feature (c) in Fig. 7.3. It is also noted that only a wave with a small α can persist after multiple bounces. Since the α of the leaky wave is smaller at higher frequencies, the multiple-bounce antenna mode scattering is dominated by returns at

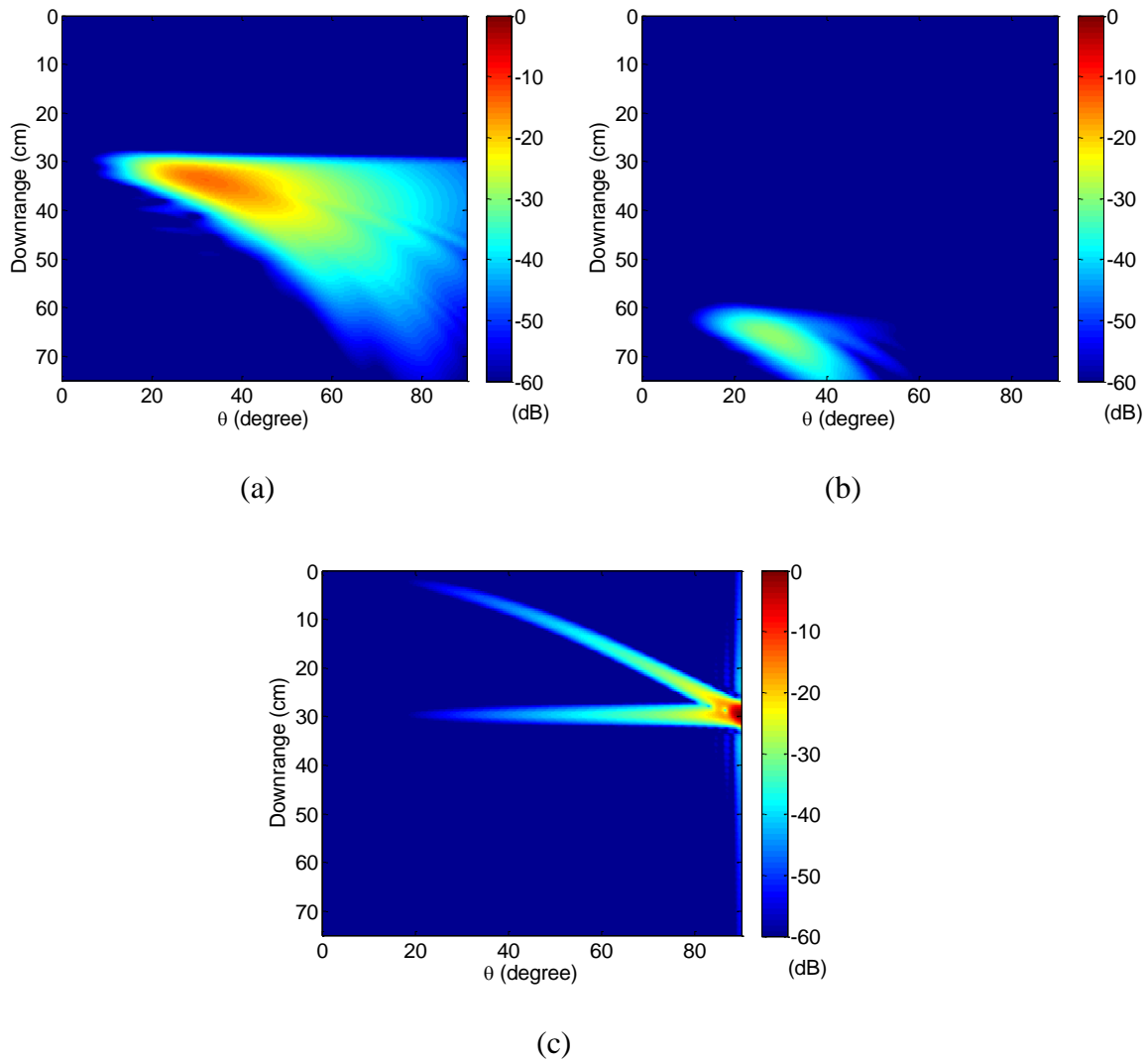


Fig. 7.5 Three scattering features modeled individually and displayed in the range-aspect plane. (a) Primary antenna mode scattering. (b) First higher-order bounce antenna mode scattering. (c) Structural mode scattering.

higher frequencies, which are clustered near the endfire direction. This trend can be noted by comparing Figs. 7.5(a) and (b).

Lastly, structural mode scattering is modeled using the physical optics (PO) approximation. The top microstrip is replaced with the induced PO current and the short vertical metal strip is neglected. Image theory is then applied to account for the ground plane. It is noted that the image current does not completely cancel the PO current on the top strip since the two are offset from the ground plane. The resulting range-aspect plot is shown in Fig. 7.5(c). The RCS features of the PO current are equivalent to two point scatterers at the two ends of the antenna. One is located at the rotation center on the left edge and the other is 29cm away on the right edge. The structural mode scattering also shows a strong flash at the broadside direction ($\theta=90^\circ$) located at a range of 29cm.

In summary, by individually modeling the scattering mechanisms, it has been shown that the prominent features (a), (b) and (c) in Fig. 7.3 can respectively be attributed to the structural mode scattering, the primary antenna mode scattering, and the first higher-order bounce antenna mode scattering. Note that both the primary antenna mode scattering and the structural mode scattering contribute to the horizontal line RCS feature at 29cm. However, the former is stronger near the endfire direction ($\theta=0^\circ$) while the latter is stronger near the broadside direction ($\theta=90^\circ$).

7.4 TIME DOMAIN INTERPRETATION OF ANTENNA MODE SCATTERING

The modeling work in the previous section provided a way to interpret the scattering mechanisms associated with the different RCS features observed in Sec. 7.2. However, the range-extended return of the antenna mode scattering warrants further examination. To better interpret such behavior, a time-of-arrival ray picture is provided here to dissect the details of this mechanism. The antenna mode scattering is first divided

into a coupling ray and a re-radiation ray (see Fig. 7.6(a)). Furthermore, the ray propagates at a slower group velocity in the antenna structure due to the dispersive leaky mode. Thus the total propagation delay of an arbitrary ray pair with respect to the left edge can be expressed as:

$$t_{delay}(\theta_{main}) = \frac{(L_1 + L_2)}{v_g(f(\theta_{main}))} - \frac{(L_1 + L_2)}{c} \cos(\theta_{main}) \quad (7.2)$$

As shown in Fig. 7.6(a), the coupling ray (in red) is assumed to couple into the antenna at location L_1 while the re-radiation ray (in black) leaves the structure at location L_2 . The group velocity v_g can be numerically computed from the propagation constant in Fig. 7.1. v_g is a function of frequency, which can be further related to the main beam direction, θ_{main} .

The time or range delay of any ray pair with an arbitrary L_1 and L_2 can be computed using (7.2) given an observation direction θ . The lower bound on the time delay occurs when $L_1=L_2=0$. The corresponding ray pair is labeled as (i) in Fig. 7.6(b), with the coupling ray impinging on the structure at the left edge and the re-radiation ray departing at the left edge. The upper bound on the time delay occurs when $L_1=L_2=L$. The corresponding ray pair is labeled as (ii) in Fig. 7.6(b), with the coupling ray impinging on the structure at the right edge and the re-radiation ray departing at the right edge. Shown in Fig. 7.7 is the complex sum of the three modeled features discussed in the last section with each feature computed under the same plane wave excitation. The lower and upper bounds computed from (7.2) are overlaid in dashed and dotted lines in the figure, where the rotation center (the left edge) is at the range of 29cm. It is seen that the range-extended feature (b) indeed falls in between the two calculated bounds. Therefore, it can

be concluded that the antenna receives and radiates as a continuous aperture such that a ray can enter and leave the structure at any point along the antenna aperture.

A shorted load is assumed to model the source impedance at the antenna input port throughout this paper to simplify the discussion. A source impedance that is better matched to the antenna will decrease the strength of the antenna mode scattering, as indicated by Γ in (7.1).

7.5 CONCLUSION

In this paper, the RCS of a half-width microstrip leaky wave antenna has been investigated in detail. It was found through simulation and measurement that distinct RCS features in the range-aspect plane can be observed. By modeling the scattering mechanisms individually, we were able to identify the observed features as the primary antenna mode scattering, higher-order bounce antenna mode scattering and structural mode scattering. The unique range-extended return due the antenna mode scattering was further interpreted using a time-of-arrival ray picture. It was shown that the extended range delay can be directly attributed to the continuous aperture of the microstrip LWA and the frequency-dependent group velocity of the leaky mode. It can also be inferred that the next higher order leaky mode will contribute to the RCS in a similar fashion, while multiple modes will be excited at the same time. Overall, the theories explained the monostatic RCS features of the microstrip LWA well. Moreover, the phenomenology described in this paper should be applicable in other types of leaky wave antennas, including those based on waveguide designs [104].

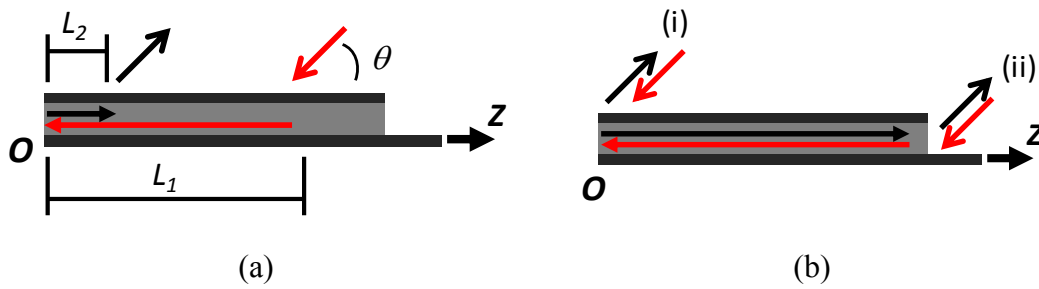


Fig. 7.6 (a) The coupling ray (in red) and the re-radiation ray (in black) along the sideview of the antenna. (b) The earliest and the latest ray pairs are labeled as (i) and (ii). Their corresponding time delays are plotted as the dashed and solid lines in Fig. 7.7.

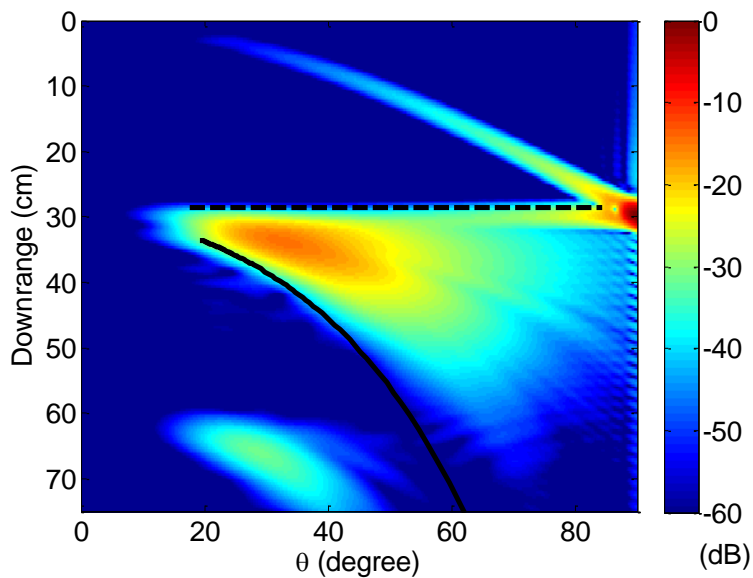


Fig. 7.7 Total RCS in the range-aspect plane by adding the three individually modeled scattering mechanisms. The dashed and dotted lines correspond respectively to the lower and upper bound in the range delay of the the primary antenna mode scattering.

Chapter 8: Conclusions and Future Work

8.1 CONCLUSIONS

The combination of a frequency-scanned antenna, a short-pulse radar, and radar signal processing algorithms for tracking humans in the 2-D range-azimuth plane has been studied in this dissertation. This approach is very attractive since only one antenna and one transceiver are required. The complexity and cost are vastly reduced compared to a traditional phased array system. A microstrip LWA was chosen as the frequency-scanned antenna in this dissertation due to the simple structure and well-studied antenna behaviors. Various aspects of this system were investigated.

In Chapter 2, the operating principle of a microstrip LWA was reviewed. The frequency-scanned property was related to the dispersion nature of the higher order leaky modes on a microstrip. A half-width microstrip LWA was designed, built, and measured to demonstrate the frequency-scanned beam. A 36° scanning range was covered from 5.5GHz to 10GHz. In Chapter 3, the frequency bandwidth, which is related to the down range resolution, was discussed in a modal perspective. The concept of “target bandwidth” was further elaborated. It was shown that the range resolution of a frequency-scanned antenna is a function of target directions. Next, the frequency bandwidth and antenna beamwidth were explored simultaneously to achieve ranging and direction-finding within a single frequency scan. To convert the collected frequency response into a range-azimuth image, targets were separated in the down range domain first. The range-gated target response was inverse Fourier transformed to the frequency domain and further related with the azimuth response. It was shown that this operation is equivalent to the STFT. Measurements of static trihedrals and moving humans were conducted with two microstrip LWAs and a VNA. Range-azimuth images were generated and the system successfully tracked two walking humans with a 3Hz repetition rate.

In Chapter 4, a half-width microstrip LWA was integrated with a short-pulse radar. A long half-width microstrip LWA was designed and built to match the frequency bandwidth of the short-pulse radar. The antenna was lengthened to improve the azimuth resolution. A circulator was included in the setup to reduce the required number of antennas and self-jamming. It was shown that, although the UWB radar transmits short pulses in time while the frequency-scanned antenna operates in the frequency domain, the two modules can be combined to operate effectively. A single human was tracked in both line-of-sight and through-wall setups. The scanning range of this portable system is less than the VNA-based system due to the roll-off at higher frequencies of the short-pulse radar.

In Chapter 5, a two-section microstrip LWA structure was proposed to achieve a narrow beamwidth. It was shown that the antenna beamwidth of a LWA can only be narrowed by both making the antenna longer and reducing the attenuation constant of the leaky mode. TRM analysis of the new structure was carried out to compute the complex propagation constant. The structure was modeled with two transmission lines. The step discontinuity was modeled as a lump capacitor. The results showed that a thin and wide second section is required to lower the attenuation constant. A short prototype was built and compared with TRM results with good agreement. Full-wave simulations of long antennas were carried out to demonstrate the performance of the proposed two-section microstrip LWA. In comparison to a half-width design, the two-section design can achieve a narrower beamwidth with a slightly wider scanning range. However, the narrower antenna beamwidth also results in a narrower frequency bandwidth. The trade-off between these two properties is intrinsic to frequency-scanned antennas.

In Chapter 6, the STFT was replaced with a compressive sensing technique to produce a narrower target response in both the down range and azimuth dimensions. It

was shown that compressive sensing is well suited for the imaging problem using a frequency-scanned antenna, viz., finding a few targets in a large 2-D space from 1-D frequency data. The combined L1-L2 cost function was chosen to control noise encountered in measurements. Compressive sensing was tested with point scatterer simulation, static target measurement, as well as two moving human measurement. The target responses in all these results were sharper when compared to those produced using the STFT. Next, the resolving capability of compressive sensing was tested with closely spaced targets in both the down range and azimuth dimensions. The testing results showed that compressive sensing achieves super resolution in the down range dimension. However, the azimuth resolution is still governed by the antenna beamwidth. Afterwards, a long antenna was combined with compressive sensing. The near field effect was included since the antenna was long and targets were close. This combination achieves the best resolution in both the down range and azimuth dimensions.

In Chapter 7, the radar cross section of a microstrip LWA was studied. The antenna mode scattering and the structural mode scatter were modeled separately. The former was related to the frequency-scanned property of the antenna and the latter was modeled with physical optics. The unique range-extended return due the antenna mode scattering was further interpreted using a time-of-arrival ray picture. It was shown that the extended range delay can be directly attributed to the continuous aperture of the microstrip LWA and the frequency-dependent group velocity of the leaky mode.

Overall, this dissertation considered the combination of a frequency-scanned antenna, radar hardware, and signal processing to achieve tracking of humans in the 2-D range-azimuth plane. A portable system consists of a single antenna and a single transceiver was demonstrated. It was also found that the performance could be further

improved by either a new antenna structure, the application of more advanced signal processing, or both.

8.2 FUTURE WORK

The results reported in this dissertation showed that a frequency-scanned antenna is a viable alternative to a complex phased array system for human tracking. The concept can be further extended to various other radar monitoring applications discussed in Chapter 1. The frequency-scanned tracking system can be combined with Doppler processing to achieve simultaneous tracking and target identification. A 3-D range-azimuth-elevation imaging is also possible by utilizing multiple frequency-scanned antennas as a 2-D aperture. The beam can be steered in one dimension using the frequency-scanned property and in the other dimension by phased shifters. Future research topics in antenna and radar hardware are discussed to meet these new challenges.

Comparing to a phased array system, a frequency-scanned antenna has limited angular coverage. The angular coverage of a phased array could extend up to 180° while that of the microstrip LWA used in this dissertation is only about 45° . This is due to the dispersive nature of the higher order leaky mode. Researchers have been studying other types of LWAs, such as meta-material LWAs [105, 106]. One major strength of a meta-material LWA is that it can cover a wide scanning range by seamlessly connecting two leaky modes. Periodicity is introduced into the LWA and a backward wave can be created correspondingly. The structure is carefully designed such that the onset of the backward and forward waves are seamlessly connected at the broadside direction. A nearly 180° scanning range can be achieved. However, there are two potential drawbacks for radar applications. First, a dielectric substrate is usually required to implement the

two modes. This will certainly limit the frequency bandwidth of the modes and hamper the range resolution as discussed in Chapter 3. Second, numerous sub-wavelength structures are required in this type of antenna to properly create the two modes. This could potentially lead to a higher conductor loss and a larger total attenuation constant. As discussed in Chapter 5, a high conductor loss limits the antenna beamwidth. The problem to design an LWA with a wide scanning range, broad frequency bandwidth, and a narrow beam is an interesting research problem worth investigating.

A VNA and a short-pulse radar were used in this dissertation to drive the frequency-scanned antenna. The VNA was operated as a stepped-frequency radar. A continuous wave was sent for a certain duration and the receiver collected data at the same time. A long duration was used to improve the signal-to-noise ratio (SNR). In all, the VNA achieves an absolutely flat frequency response, superior dynamic range, and high SNR at the cost of data acquisition time. Another major drawback of the VNA is the self-jamming problem, since the receiver collects data while the transmitter is transmitting the signal. On the contrary, the short pulse radar with a coherent receiver requires a shorter acquisition time. The short-duration transmit pulse also eliminates the self-jamming problem. Most of the static residues are from environmental clutters instead of the radar itself. However, the transmitted power from the P410 is low. This is done intentionally in order to meet regulatory requirements. Acceptable SNR is only obtained with a large number of pulse integrations. As a result, the refresh rate is reduced. A broadband power amplifier (PA) is desirable to improve the SNR while keeping a very high refresh rate.

The frequency response of the receiver in the P410 was designed to match the frequency content of the transmitted pulse. While this architecture can achieve the highest SNR for most applications, it deteriorates the received waveform from a

frequency-scanned antenna. The corresponding frequency-finding capability is hampered. Moreover, the internal sampling switches are optimized to produce the sharpest time domain step response. However, this architecture creates side lobes in the frequency domain. The time domain behavior of the sampling switch can be optimized to achieve less frequency side lobes and yield a better frequency domain response. It is interesting that a coherent short-pulse radar can be designed to suite operations in the frequency domain. Lastly, any early reflections within the radar can create deep nulls in the frequency response. The transmit/receive switch inside the P410 radar currently causes this problem. A careful PCB layout, component selection, and possibly using multiple circulators could improve the purity of the pulse. This is required to achieve better performances in both the time and frequency domains.

In order to obtain the Doppler frequencies of targets, the phase responses from one range scan to the next are compared. This can be readily incorporated in the existing system. However, the rate to update the range scans must be twice faster than the highest Doppler frequencies of targets to avoid aliasing. For humans, the maximum Doppler frequency is about 100Hz for a 4.3GHz carrier frequency. The highest refresh rate achieved in the measurement using a P410 was 20Hz. It is clear that the Doppler frequencies of the collected data are aliased. To increase the refresh rate, the range extend and the number of integration must be reduced. As discussed previously, a broadband high-power PA could help improve the SNR. A heterodyne receiver may also be worthwhile to investigate, as range profiles can be generated at the rate of the pulse-repetition rate. However, a fast analog-to-digital converter (ADC) is required and it may take a lot of power to operate. Moreover, the dynamic range of a fast ADC is also limited. In short, a transceiver must be designed and built carefully to achieve a sufficient refresh rate to detect the Doppler frequencies of a human.

Lastly, multiple transceivers and frequency-scanned antennas can be combined to form a 2-D aperture. The major challenge is the synchronization between transceivers. Pico-second accuracy is required for a short-pulse system. The pulse distribution network needs to distribute pulses to different antennas with equal delays and low dispersion. It also requires careful design and layout to remove any minor reflections that could deteriorate the frequency response. It is a challenging microwave engineering problem on its own. A simpler approach is to only use a single transmitter. Different receivers can operated independently. The direction of targets can be analyzed later using software beam forming. Such a low-cost 2-D aperture could be useful for many applications, considering the number of transceivers is on the order of a traditional 1-D linear phased array.

REFERENCES

- [1] J. L. Geisheimer, E. F. Greneker III and W. S. Marshall, "High-resolution Doppler model of the human gait," *Proc. SPIE, Radar Sensor Tech. Data*, vol. 4744, pp. 8-18, July 2002.
- [2] P. van Dorp and F. C. A. Groen, "Human walking estimation with radar," *Proc. Inst. Elect. Eng. - Radar, Sonar Navig.*, vol. 150, no. 5, pp. 356-365, Oct. 2003.
- [3] T. Thayaparan, S. Abrol, E. Riseborough, L. Stankovic, D. Lamothe and G. Duff, "Analysis of radar micro-Doppler signatures from experimental helicopter and human data," *IET Radar Sonar Navigation*, vol. 1, no. 4, pp. 289-299, Aug. 2007.
- [4] T. Dogaru, C. Le and G. Kirose, "Time-frequency analysis of a moving human Doppler signature," U.S. Army Research Laboratory, Feb. 2009.
- [5] S. S. Ram, C. Christianson, Y. Kim and H. Ling, "Simulation and analysis of human microDopplers in through-wall environments," *IEEE Trans. Geosci. Remote Sens.*, vol. 48, no. 4, pp. 2015-2023, 2010.
- [6] P. Setlur, M. Amin and F. Ahmad, "Urban target classifications using time-frequency micro-Doppler signatures," in *Int. Symp. Signal Processing and Its Application*, Feb. 2007.
- [7] M. D. Anderson and R. L. Rogers, "Micro-Doppler analysis of multiple frequency continuous wave radar signatures," *Proc. SPIE , Radar Sensor Technology XI*, vol. 6547, p. 65470A, May 2007.
- [8] S. S. Ram and H. Ling, "Micro-Doppler signature simulation of computer animated human and animal motions," in *IEEE Antennas Propag. Int. Symp.*, San Diego, July 2008.
- [9] A. Stove and S. R. Sykes, "A Doppler-based automatic target classifier for a battlefield surveillance radar," in *Radar Conf.*, Edinburgh, UK, Oct. 2002.
- [10] I. Bilik, J. Tabrikian and A. Cohen, "GMM-based target classification for ground surveillance Doppler radar," *IEEE Trans. Aerospace Electron. Syst.*, vol. 42, no. 1, pp. 267-278, 2006.
- [11] G. E. Smith, K. Woodbridge and C. J. Baker, "Template based micro-Doppler signature classification," in *European Radar Conference*, Manchester, UK, Sept. 2006.
- [12] M. Otero, "Application of a continuous wave radar for human gait recognition," *Proc. SPIE, Signal Process., Sensor Fusion, Target Recog.*, vol. 5809, pp. 538-

548.

- [13] Y. Kim and H. Ling, "Human activity classification based on microDoppler signatures using a support vector machine," *IEEE Trans. Geosci. Remote Sensing, special issue on Indoor Imaging*, vol. 47, no. 5, pp. 1328-1337, 2009.
- [14] B. G. Mobasser and M. G. Amin, "A time-frequency classifier for human gait recognition," *Proc. SPIE, Optics and Photonics in Global Homeland Security V and Biometric Technology for Human Identification VI*, vol. 7306, p. 730628, 2009.
- [15] A. Lin and H. Ling, "A Doppler and direction-of-arrival (DDOA) radar for multiple-mover sensing based on a two-element array," *IEEE Trans. Aerosp. Electron. Syst.*, vol. 43, no. 4, pp. 1496-1509, Oct. 2007.
- [16] A. Lin and H. Ling, "Location tracking of indoor movers using a two-frequency Doppler and direction-of-arrival (DDOA) radar," in *IEEE Int. Antennas Propag. Symp.*, Albuquerque, NM, July 2006.
- [17] S. S. Ram and H. Ling, "Through-wall tracking of human movers using joint Doppler and array processing," *IEEE Geosci. Remote Sens. Letts.*, vol. 5, no. 3, pp. 537-541, July 2008.
- [18] A. Lin and H. Ling, "Frontal imaging of human using three-element Doppler and direction-of-arrival radar," *Electronics Letters*, vol. 42, no. 11, pp. 660-661, May 2006.
- [19] S. S. Ram, "Radar simulation of human activities in non line-of-sight environments," Ph.D. dissertaion, Univ. of Texas at Austin, 2009.
- [20] E. Staderini, "UWB radars in medicine," *IEEE Aerospace Electron. Syst.*, vol. 17, pp. 13-18, Jan 2002.
- [21] J. Lai, Y. Xu, E. Gunawan, E. Chua, A. Maskooki, Y. L. Guan, L. K.-S., C. B. Soh and C.-L. Poh, "Wireless sensing of human respiratory parameters by Low-power ultrawideband impulse radio radar," *IEEE Trans. Instrum. Meas.*, vol. 60, no. 3, pp. 928-938, 2011.
- [22] B. Shleicher, I. Nasr, A. Trasser and H. Schumacher, "IR-UWB radar demonstrator for ultra-fine movement detection and vital-sign monitoring," *IEEE Trans. Microw. Theory Tech.*, vol. 61, no. 5, pp. 2076-2085, 2013.
- [23] P. Bernardi, R. Cicchetti, S. Pisa, E. Pittella, E. PiuZZi and O. Testa, "Design, realization, and test of a UWB radar sensor for breath activity monitoring," *IEEE Sensors J.*, vol. 14, no. 2, pp. 584-596, 2014.
- [24] S. Nag, M. A. Barnes, T. Payment and G. Holladay, "An ultrawideband through-

- wall radar for detecting the motion of people in real time," *Proc. SPIE, Radar Sensor Technology and Data Visualization*, 48, vol. 4744, pp. 48-57, 30 July 2002.
- [25] A. R. Hunt, "A wideband imaging radar for through-the-wall surveillance," *Proc. SPIE, Sensors, and Command, Control, Communications, and Intelligence (C3I) Technologies for Homeland Security and Homeland Defense III*, vol. 5403, pp. 590-596, 2004.
- [26] A. R. Hunt, "Use of a frequency-hopping radar for imaging and motion detection through walls," *IEEE Trans. Geosci. Remote Sens.*, vol. 47, no. 5, pp. 1402-1408, 2009.
- [27] Y.-J. Ren, C.-P. Lai, P.-H. Chen and R. Narayanan, "Compact ultrawideband UHF array antenna for through-wall radar applications," *IEEE Antennas Wireless Propag. Letts.*, vol. 8, no. 12, pp. 1302-1305, 2009.
- [28] Q. Liu, Y. Wang and A. Fathy, "Towards low cost, high speed data sampling module for multifunctional real-time UWB radar," *IEEE Trans. Aerosp. Electron. Syst.*, vol. 49, no. 2, pp. 1301-1316, Apr. 2013.
- [29] R. O. Schmidt, "Multiple emitter location and signal parameter estimation," *IEEE Trans. Antennas Propag.*, vol. 134, no. 3, pp. 276-280, 1986.
- [30] J. A. Hogbom, "Aperture synthesis with a non-regular distribution of interferometer baselines," *Astron. Astrophys. Supplement*, vol. 15, pp. 417-426, June 1974.
- [31] Y.-S. Yoon and M. G. Amin, "High-resolution through-the-wall radar imaging using beamspace MUSIC," *IEEE Trans. Antennas Propag.*, vol. 56, no. 6, pp. 1763-1774, 2008.
- [32] P. C. Chang, R. J. Burkholder and J. L. Volakis, "Adaptive CLEAN With target refocusing fort through-wall image improvement," *IEEE Trans. Antennas Propag.*, vol. 58, no. 1, pp. 155-162, 2010.
- [33] F. Ahmad, Y. Zhang and M. Amin, "Three-dimensional wideband beamforming for imaging through a single wall," *IEEE Geosci. Remote Sens. Lett.*, vol. 5, no. 2, pp. 176-179, Apr. 2008.
- [34] S. Hantscher, A. Reizenzahn and C. G. Diskus, "Through-wall imaging with a 3-D UWB SAR algorithm," *IEEE Signal Proc. Letts.*, vol. 15, pp. 269-272, Feb. 2008.
- [35] R. Solimene, F. Soldovieri, G. Prisco and R. Pierri, "Three-dimensional through-wall imaging under ambiguous wall parameters," *IEEE Trans. Geosci. Remote*

- Sens.*, vol. 47, no. 5, pp. 1310-1317, 2009.
- [36] K. E. Browne, R. J. Burkholder and J. L. Volakis, "Through-wall opportunistic sensing system utilizing a low-cost flat-panel array," *IEEE Trans. Antennas Propag.*, vol. 59, no. 3, pp. 859-868, 2011.
- [37] Y. Wang and A. Fathy, "Advanced system level simulation platform for three-dimensional UWB through-wall imaging SAR using time-domain approach," *IEEE Trans. Geosci. Remote Sens.*, vol. 50, no. 5, pp. 1986-2000, 2012.
- [38] W. Zhang and A. Hoorfar, "Three-dimensional real-time through-the-wall radar imaging with diffraction tomographic algorithm," *IEEE Trans. Geosci. Remote Sens.*, vol. 51, no. 7, pp. 4155-4163, 2013.
- [39] A. Eryildirim and I. Onaran, "Pulse Doppler radar target recognition using a two-stage SVM procedure," *IEEE Aerospace Electron. Syst.*, vol. 42, no. 2, pp. 1450-457, Apr. 2011.
- [40] J. D. Bryan, J. Kwon, N. Lee and Y. Kim, "Application of ultra-wide band radar for classification of human activities," *IET Radar Sonar Navigation*, vol. 6, no. 3, pp. 172-127, 2011.
- [41] J. Li, Z. Zeng, J. Sun and F. Liu, "Through-wall detection of human being's movement by UWB radar," *IEEE Geosci. Remote. Sens. Lett.*, vol. 9, no. 6, pp. 1079-1083, Nov. 2012.
- [42] O. R. Fogle and B. D. Rigling, "Micro-range/micro-Doppler decomposition of human radar signatures," *IEEE Trans. Aerospace Electron. Syst.*, vol. 48, no. 4, pp. 3058-3072, Oct. 2012.
- [43] Y. Wang, Q. Liu and A. E. Fathy, "CW and pulse-Doppler radar processing based on FPGA for human sensing applications," *IEEE Trans. Geosci. Remote Sens.*, vol. 51, no. 5, pp. 3097-3107, 2013.
- [44] Y. Yang and A. E. Fathy, "See-through-wall imaging using ultra wideband short-pulse radar system," in *Proc. IEEE Int. Antennas Propag. Symp.*, Washington, DC, 2005.
- [45] M. I. Skolnik, *Radar Handbook*, 1st ed., NY: McGraw-Hill, 1970.
- [46] M. Wollitzer, J. Buechler, J.-F. Luy, U. Siart, E. Schmidhammer, J. Detlefsen and M. Esslinger, "Multifunctional radar sensor for automotive application," *IEEE Microw. Theory Tech.*, vol. 46, no. 5, pp. 701-708, 1998.
- [47] S. Matsuzawa, K. Sato, Y. Inoe and T. Nomura, "Steerable composite right/left-handed leaky wave antenna for automotive radar applications," in *Eur. Microw. Conf.*, Manchester, UK, Sept. 2006.

- [48] M. Ettorre, R. Sauleau, L. Le Coq and F. Bodereau, "Single-folded leaky-wave antennas for automotive radars at 77 GHz," *IEEE Antennas Wireless Propag. Lett.*, vol. 9, pp. 859-862, 2010.
- [49] W. Menzel and A. Moebius, "Antenna concepts for millimeter-wave automotive radar sensors," *Proc. IEEE*, vol. 100, no. 7, pp. 2372-2379, 2012.
- [50] A. A. Oliner and K. S. Lee, "The nature of the leakage from higher modes on microstrip Line," in *IEEE MTT-S Int. Microw. Symp. Dig.*, Baltimore, MA, 1986.
- [51] G. M. Zelinski, G. A. Thiele, M. L. Hastriter, M. J. Havrilla and A. J. Terzuoli, "Half width leaky wave antennas," *IET Microw. Antennas Propag.*, vol. 1, no. 2, pp. 341-348, 2007.
- [52] H. Ertmert, "Guided modes and radiation characteristics of covered microstrip lines," *Arch. Elektron. Ubertrag. technik.*, vol. 30, no. 2, pp. 65-70, 1976.
- [53] W. Menzel, "A new travelling wave antenna in microstrip," in *Proc. 8th Eur. Microw. Conf.*, Paris, 1978.
- [54] D. C. Chang and E. F. Kuester, "Total and partial reflection from the end of a parallel-plate waveguide with an extended dielectric slab," *Radio Sci.*, vol. 16, pp. 1-13, Feb. 1981.
- [55] E. F. Kuester, R. Johnk and D. Chang, "The thin-substrate approximation for reflection from the end of a slab-loaded parallel-plate waveguide with application to microstrip patch antennas," *IEEE Trans. Antennas Propag.*, vol. 30, no. 5, pp. 910-917, Sept. 1982.
- [56] A. Oliner and K. Lee, "Microstrip leaky wave strip antennas," in *IEEE Int. Antennas Propag. Symp.*, Philadelphia, PA, 1986.
- [57] C. Luxey and J. M. Latheurte, "Simple design of dual-beam leaky-wave antennas in microstrips," *IEE Proc. Microw. Antennas, Propag.*, vol. 144, no. 6, pp. 397-402, Dec. 1997.
- [58] J. Grimm and D. Nyquist, "Spectral analysis considerations relevant to radiation and leaky modes of open-boundary microstrip transmission line," *IEEE Trans. Microw. Theory Tech.*, vol. 41, no. 1, pp. 150-153, 1993.
- [59] Y.-D. Lin, J.-W. Sheen and C.-K. C. Tzuang, "Analysis and design of feeding structures for microstrip leaky-wave antenna," *IEEE Trans. Antennas Propag.*, vol. 44, no. 9, pp. 1540-1547, 1996.
- [60] S.-D. Chen and C. K. C. Tzuang, "Characteristic impedance and propagation of the first higher order microstrip mode in frequency and time domain," *IEEE Trans. Microw. Theory Tech.*, vol. 50, no. 5, pp. 1370-1379, May 2002.

- [61] W. Hong, T.-L. Chen, C.-Y. Chang, J.-W. Sheen and Y.-D. Lin, "Broadband tapered microstrip leaky-wave antenna," *IEEE Trans. Antennas Propag.*, vol. 51, no. 8, pp. 1922-11928, 2003.
- [62] H. Jiang, R. Penno, K. Pasala, L. Kempel and S. Schneider, "Broadband microstrip leaky wave antenna with inhomogeneous materials," *IEEE Trans. Antennas Propag.*, vol. 57, no. 5, pp. 1558-1562, 2009.
- [63] C.-N. Hu and C.-K. C. Tzuang, "Analysis and design of large leaky-mode array employing the coupled-mode approach," *IEEE Trans. Microw. Theory Tech.*, vol. 49, pp. 629-636, Apr. 2001.
- [64] P. Baccarelli, P. Burghignoli, F. Frezza, A. Galli and P. Lampariello, "Novel modal properties and relevant scanning behaviors of phased arrays of microstrip leaky-wave antennas," *IEEE Trans. Antennas Propag.*, vol. 51, pp. 3228-3238, Dec. 2003.
- [65] J. L. Gomez-Tornero, D. Caete-Rebenaque and A. Alvarez-Melcon, "Microstrip leaky wave antenna with control of leakage rate and only one main beam in the azimuth plane," *IEEE Trans. Antennas Propag.*, vol. 56, no. 2, pp. 335-344, 2008.
- [66] M. Archbold, E. J. Rothwell, L. C. Kempel and S. W. Schneider, "Beam steering of a half-width microstrip leaky-wave antenna using edge loading," *IEEE Antennas Wireless Propag. Lett.*, vol. 9, pp. 203-206, 2010.
- [67] S. Lim, C. Caloz and T. Itoh, "Electronically scanned composite right/left handed microstrip leaky-wave antenna," *IEEE Microw. Wireless Compon. Lett.*, no. 14, pp. 277-279, June 2004.
- [68] R. O. Ouedraogo, E. J. Rothwell and B. J. Greetis, "A reconfigurable microstrip leaky-wave antenna with a broadly steerable beam," *IEEE Trans. Antennas Propag.*, vol. 59, pp. 3080-3083, Aug 2011.
- [69] J. Long, M. Jacob and D. F. Sievenpiper, "Electronically steerable antenna using superluminal waveguide and tunable negative capacitors," in *Proc. IEEE Int. Symposium on Antennas Propag.*, Chicago, 2012.
- [70] J. Liu, D. R. Jackson and Y. Long, "Propagation wavenumbers for half- and full-width microstrip line in the EH₁ mode," *IEEE Trans. Antennas Propag.*, vol. 59, pp. 3005-3012, Dec. 2011.
- [71] T. Tomofuji, H. Terada, S. Kawabata, K. Wakino and T. Kitazawa, "Full-wave analysis and design of circular half-width microstrip leaky wave antenna," *IEEE Trans. Antennas Propag.*, vol. 61, no. 8, pp. 3967-3975, 2013.
- [72] FEKO version 6.2, Stellenbosch, South Africa: EM Software & Systems Inc.,

2012.

- [73] M. Winfried, M. Wetzel and M. Menzel, "A novel direct-imaging radar sensor with frequency scanned antenna," in *IEEE MTT-S Int. Microw. Symp. Dig.*, Philadelphia, PA, USA, 2003.
- [74] S.-T. Yang and H. Ling, "Design of a microstrip leaky-wave antenna for two-dimensional bearing tracking," *IEEE Antennas Wireless Propag. Lett.*, vol. 10, pp. 784-787, 2011.
- [75] Time Domain, "P410 Data Sheet," 2013. [Online]. Available: <http://www.timedomain.com/p400.php>.
- [76] Commission, Federal Communications, "Revision of Part 15 of the Commission's Rules Regarding Ultra-Wideband Transmission Systems," 2001. [Online]. Available: http://transition.fcc.gov/Bureaus/Engineering_Technology/Orders/2002/fcc02048.pdf.
- [77] C. Zhang, A. Fathy and M. Mahfouz, "Performance enhancement of a sub-sampling circuit for ultra-wideband signal processing," *IEEE Microw. Wireless Compon. Lett.*, vol. 17, no. 12, pp. 873-875, 2007.
- [78] D. Lee, J. Sung and J. Park, "A 16ps-resolution random equivalent sampling circuit for TDR utilizing a vernier time delay generation," in *Proc. IEEE Nuclear Sci. Symp.*, Portland, OR, 2003.
- [79] L. Nguyen, D. Wong, M. Ressler and F. Koeing, "Obstacle avoidance and concealed target detection using the Army Research Lab ultra-wideband synchronous impulse reconstruction (UWB SIRE) forward imaging radar," *Proc. of SPIE*, vol. 6553, p. 65530H, 2007.
- [80] Y. Yang and A. Fathy, "Development and implementation of a real-time see-through-wall radar system based on FPGA," *IEEE Trans. Geosci. Remote Sens.*, vol. 47, no. 5, pp. 1270-1280, 2009.
- [81] R. E. Collin, in *Field Theory of Guided Waves*, 2/e ed., New York, IEEE Press, 1991, p. 600.
- [82] L. O. Goldstone and A. A. Oliner, "Leaky-wave antenna I: rectangular waveguide," *IRE Trans. Antennas Propag.*, vol. 7, no. 4, pp. 307-319, Oct. 1959.
- [83] P. Lampariello, F. Frezza, H. Shigesawa, M. Tsuji and A. A. Oliner, "A versatile leaky-wave antenna based on stub-loaded rectangular waveguide .I. Theory," *IEEE Trans. Antennas Propag.*, vol. 46, no. 7, pp. 1032-1041, 1999.
- [84] D. L. Donoho, "Compressed sensing," *IEEE Trans. Inf. Theory*, vol. 52, no. 4, pp.

- 1289-1306, 2006.
- [85] E. J. Candes, J. Romberg and T. Tao, "Robust uncertainty principles: exact signal reconstruction from highly incomplete frequency information," *IEEE Trans. Inf. Theory*, vol. 52, no. 2, pp. 489-509, 2006.
 - [86] S. S. Chen, D. L. Donoho and M. A. Saunders, "Atomic decomposition by basis pursuit," *SIAM J. Sci. Comput.*, vol. 20, no. 1, pp. 33-61, 1998.
 - [87] D. L. Donoho and X. Huo, "Uncertainty principles and ideal atomic decomposition," *IEEE Trans. Inf. Theory*, vol. 47, no. 7, pp. 2845-2862, Nov. 2001.
 - [88] R. Gribonval and M. Nielsen, "Sparse representations in unions of basis," *IEEE Trans. Inf. Theory*, vol. 49, no. 12, pp. 3320-3325, 2003.
 - [89] D. L. Donoho and M. Elad, "Optimally sparse representation in general (nonorthogonal) dictionaries via ℓ_1 minimization," *Proc. Nat. Acad. Sci. USA*, vol. 100, pp. 2197-2202, Mar. 2003.
 - [90] M. Elad and A. M. Bruckstein, "A generalized uncertainty principle and sparse representation in pairs of bases," *IEEE Trans. Inf. Theory*, vol. 48, no. 9, p. 2558-2567, 2002.
 - [91] J. A. Tropp, "Greed is good: Algorithmic results for sparse approximation," *IEEE Trans. Inf. Theory*, vol. 50, no. 10, p. 2231-2242, 2004.
 - [92] M. Friedlander and E. Van den Berg, "Probing the pareto frontier for basis pursuit solutions," *SIAM J. Sci. Comput.*, vol. 31, no. 2, p. 890-912, 2008.
 - [93] J. Yang and Y. Zhang, "Alternating direction algorithms for ℓ_1 -problems in compressive sensing," *SIAM J. Sci. Comput.*, vol. 33, no. 1, pp. 250-278, 2011.
 - [94] L. C. Potter, E. Ertin, J. T. Parker and M. Cetin, "Sparsity and compressed sensing in radar imaging," *Proc. IEEE*, vol. 98, no. 6, pp. 1006-1020, 2010.
 - [95] R. Baraniuk and P. Steeghs, "Compressive radar imaging," in *2007 IEEE Radar Conference*, Boston, MA, 2007.
 - [96] A. Gurbuz, J. McClellan and W. Scott, "A compressive sensing data acquisition and imaging method for stepped frequency," *IEEE Trans. Signal Process.*, vol. 57, no. 7, p. 2640-2650, 2009.
 - [97] I. Stojanovic, W. C. Karl and W. C. M. Cetin, "Compressed sensing of mono-static and multi-static SAR," *Proc. SPIE, Algorithms Synthetic Aperture Radar Imagery XVI*, vol. 7337, pp. 1-12, Apr. 2009.

- [98] N. Whiteloni and H. Ling, "Radar signature analysis using a joint time-frequency distribution based on compressed sensing," *IEEE Trans. Antennas Propagat.*, vol. 62, no. 2, pp. 755-763, 2014.
- [99] M. Herman and T. Strohmer, "High-resolution radar via compressed sensing," *IEEE Trans. Signal Process.*, vol. 57, no. 6, p. 2275–2284, 2009.
- [100] Y. Chan, K. Ho and S. Wong, "Aircraft identification from RCS measurement using an orthogonal transform," *IEEE Proc. Radar Sonar Navig.*, vol. 147, no. 2, pp. 93-102, Apr. 2000.
- [101] E. H. Newman and D. Forrai, "Scattering from a microstrip patch," *IEEE Trans. Antennas Propag.*, vol. 35, no. 3, pp. 245-251, 1987.
- [102] H. T. Shamansky and A. K. Dominek, "The determination of the propagation constant for the traveling wave in an infinite ground plane," *IEEE Trans. Antenna Propag.*, vol. 36, no. 10, pp. 1455-1463, 1988.
- [103] W. L. Stutzman and G. A. Thiele, in *Antenna Theory and Design 2/e*, 2ed ed., Hoboken, Wiley & Sons, pp. 472-477.
- [104] F. Frezza, P. Lampariello, H. Shigesawa, M. Tsuji and A. Oliner, "A versatile leaky-wave antenna based on stub-loaded rectangular waveguide II: effects of flanges and finite stub length," *IEEE Trans. Antennas Propag.*, vol. 46, no. 7, pp. 1042-1046, 1998.
- [105] A. Lai, T. Itoh and C. Caloz, "Composite right/left-handed transmission line metamaterials," *IEEE Microwave Magazine*, vol. 5, no. 3, pp. 34-50, Sep. 2004.
- [106] Y.-J. Chi and F.-C. Chen, "CRLH leaky wave antenna based on ACPS technology with 180 horizontal plane scanning capability," *IEEE Trans. Antennas Propag.*, vol. 61, no. 2, pp. 571-577, 2013.